LEVEL

(12)

(18) (19)

DNA 4380F

(6)
LABORATORY STUDY OF DEEP-BASED STRUCTURES IN SUPPORT OF DIABLO HAWK

AD A091370

SRI International

333 Ravenswood Avenue

Menlo Park, California 94025

DTIC
ELECTE
NOV 5 1980
C

(11) 1 Feb 78 (12) 135

(9) Final Report 15 Sep —31 Dec 77.

CONTRACT No. DNA 001-76-C-0385

(15)

(17) 73

(16)
J34HAXS

(10)
P. E. /Senseny
H. E. /Lindberg

APPROVED FOR PUBLIC RELEASE;
DISTRIBUTION UNLIMITED.

DDC FILE COPY

Prepared for

Director

DEFENSE NUCLEAR AGENCY

Washington, D. C. 20305

80 10 30 007

410281

Destroy this report when it is no longer
needed. Do not return to sender.

REPORT DOCUMENTATION PAGE	READ INSTRUCTIONS BEFORE COMPLETING FORM

1. REPORT NUMBER	2. GOVT ACCESSION NO.	3. RECIPIENT'S CATALOG NUMBER
DNA 4380F ✓	AD-A091 370	

4. TITLE *(and Subtitle)*	5. TYPE OF REPORT & PERIOD COVERED
LABORATORY STUDY OF DEEP-BASED STRUCTURES IN SUPPORT OF DIABLO HAWK	Final Report for Period 15 Sept 77 to 31 Dec 77
	6. PERFORMING ORG. REPORT NUMBER PYU 5762 ✓

7. AUTHOR(s)	8. CONTRACT OR GRANT NUMBER(s)
P. E. Senseny H. E. Lindberg	DNA 001-76-C-0385 ✓

9. PERFORMING ORGANIZATION NAME AND ADDRESS	10. PROGRAM ELEMENT, PROJECT, TASK AREA & WORK UNIT NUMBERS
SRI International 333 Ravenswood Avenue ✓ Menlo Park, California 94025	Subtask J34HAXSX311-07

11. CONTROLLING OFFICE NAME AND ADDRESS	12. REPORT DATE
Director Defense Nuclear Agency Washington, D.C. 20305	1 February 1978
	13. NUMBER OF PAGES 138

14. MONITORING AGENCY NAME & ADDRESS(if different from Controlling Office)	15. SECURITY CLASS (of this report)
	UNCLASSIFIED
	15a. DECLASSIFICATION/DOWNGRADING SCHEDULE

16. DISTRIBUTION STATEMENT *(of this Report)*

Approved for public release; distribution unlimited.

6a 7 3 a

17. DISTRIBUTION STATEMENT *(of the abstract entered in Block 20, if different from Report)*

18. SUPPLEMENTARY NOTES

This work sponsored by the Defense Nuclear Agency under RDT&E RMSS Code B34407T462 J34HAXSX31107 H2590D.

19. KEY WORDS *(Continue on reverse side if necessary and identify by block number)*

Deep basing	Reinforcement	Joints	Plasticity
Scale models	Laboratory tests	Boreholes	Theory
Structures	Static	Cable	NONSAP
Rock	Dynamic	Elliptical	DIABLO HAWK
Tunnels	Porewater	Underground	

20. ABSTRACT *(Continue on reverse side if necessary and identify by block number)*

Laboratory studies were performed in support of DIABLO HAWK structures and cable-hardening experiments to investigate: (1) the influence of loading rate on tunnel closure in both water-saturated and dry specimens of SRI RMG 2C2, a tuff simulant; (2) borehole collapse mechanisms and borehole/cable interaction; and (3) the influence of joints and joint orientation on the closure of circular tunnels in specimens of jointed 16A rock simulant.

DD FORM 1473 EDITION OF 1 NOV 65 IS OBSOLETE

20. Results for SRI RMG 2C2 show that greater pressure must be applied in dynamic tests than in static tests to achieve a given tunnel closure. The percentage increase in pressure is twice as large for saturated specimens than for dry specimens. This larger loading rate effect in saturated specimens is due, in part, to no porewater migration and drainage in the dynamic tests.

Static and dynamic borehole collapse and borehole/cable interaction test results show that springline collapse is the dominant borehole closure mechanism and that the most severe loading on the cable is from the inward motion of springline rubble. Observed critical loads for cable damage suggest that the TRW fielding ranges in DIABLO HAWK should provide the desired range of damage from none to severe.

Static uniaxial strain loading tests were performed on specimens that contain a single set of parallel, equally spaced joints. The joint planes were parallel to the tunnel axis. Two orientations were investigated: 0° and 45° between the normal to the joint plane and the direction of major loading. Results show that there is no block motion and that tunnel deformation is due to plastic flow, fracture across the joints, and, probably, localized slipping along the joints. Joint orientation influences the pressure required to achieve a given vertical tunnel closure and also the direction of springline motion. To achieve a vertical tunnel closure of 5 percent requires a pressure of 14.0 ksi (96.5 MPa) for an intact specimen, 12.6 ksi (86.9 MPa) for the 0° orientation, and only 8.2 ksi (56.5 MPa) for the 45° orientation. Large outward springline motion occurred for the 45° joints.

A theoretical analysis was also performed to compare the efficiency of elliptical and circular structures at plastic response levels. Results for uniaxial strain loading show that if the surrounding rock remains elastic, an elliptical cross section is more efficient than a circular cross section. However, when yielding occurs in the rock, the circular cross section is more efficient because it can better resist closure at the springlines.

SUMMARY

Three series of laboratory experiments were performed to help plan
and interpret DIABLO HAWK structures and cable-hardening experiments.
The first series of experiments studied the influence of loading rate and
porewater pressure on tunnel closure in a tuff simulant. The purpose was
to evaluate the use of constitutive relations that neglect these parameters
in deep-based structure design formulae. The second and third series of
experiments studied two phenomena being addressed specifically in DIABLO
HAWK: borehole/cable interaction, and response of cylindrical structures
in jointed rock. Theoretical analyses were also performed to compare the
efficiency of elliptical and circular structures at plastic as well as
elastic levels.

S.1   TUNNEL RESPONSE UNDER DYNAMIC VERSUS STATIC LOADING

Static and dynamic tests were performed on 4-inch-diameter (0.1-m)
specimens of SRI RMG 2C2 (a tuff simulant) to study the effect of loading
rate on tunnel closure. Test specimens were both fully saturated and
dry to determine the roles of porewater pressure and rock skeleton be-
havior in dynamic versus static response. Tests were performed under
both isotropic and uniaxial strain loading. Figure S.1 plots results
of the isotropic loading tests (uniaxial strain loading test results
are similar). Greater pressure must be applied in dynamic tests to
achieve the same closures as in static tests. Also, results show that
saturated specimens are weaker than dry specimens under static loading,
but stronger under dynamic loading. This means that porewater weakens
specimens in static tests but stiffens them in dynamic tests. This
difference in porewater effect between static and dynamic loading is
due in part, to porewater migration and drainage from the specimen in
our static tests. These results indicate that dynamic and porewater
effects are important and should be included in deep-base structure
analysis.

1
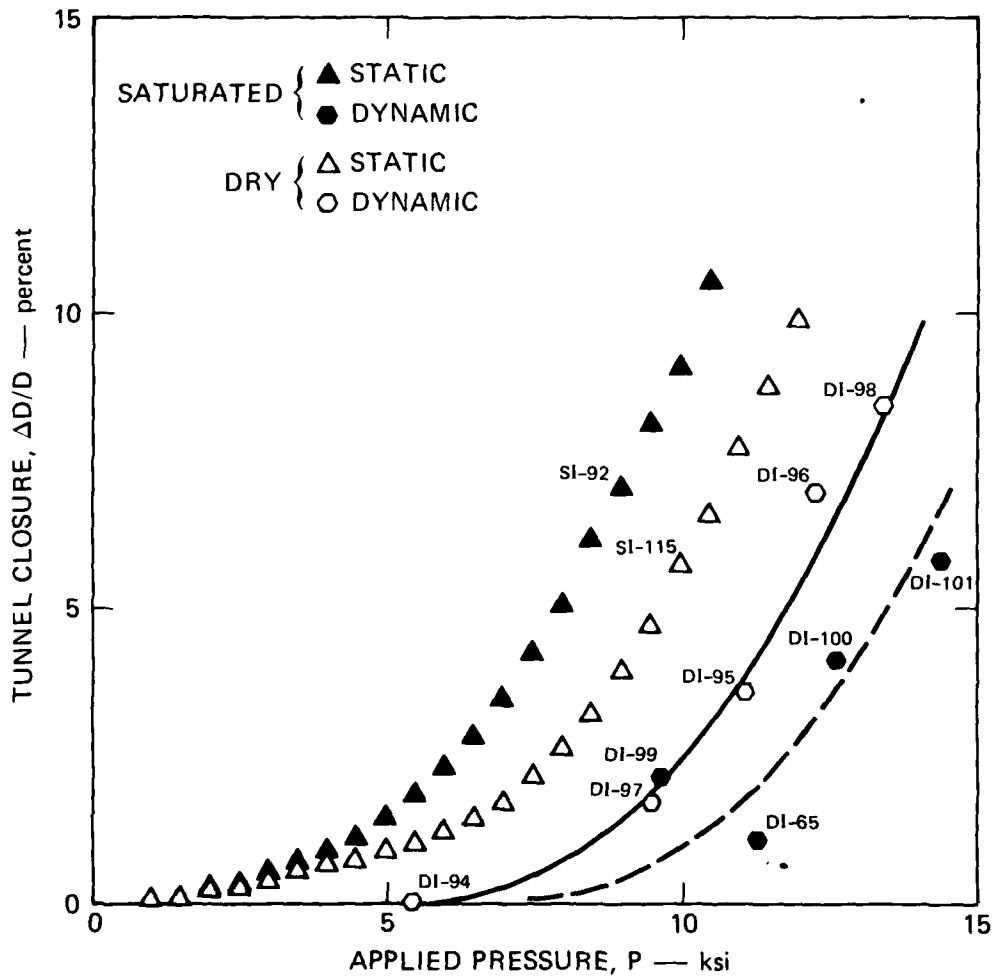
FIGURE S.1 TUNNEL CLOSURE VERSUS APPLIED PRESSURE FOR ISOTROPIC
LOADING OF SRI RMG 2C2. LINER: 6061-T0 ALUMINUM,
a/h = 11.5

2

S.2   BOREHOLE/CABLE INTERACTION

Tests were performed to provide better qualitative and quantitative understanding of borehole/cable interaction mechanisms to assist in the design and interpretation of the TRW cable-hardening experiments being fielded in DIABLO HAWK.

Static and dynamic uniaxial strain loading tests were performed on 4-inch-diameter (0.1-m) specimens of SRI RMG 2A (a weak tuff simulant) that contained 5/8-inch-diameter (16-mm) boreholes. TRW provided scale-model simulated cables in two sizes: 1/2-inch-diameter (13-mm) and 1/4-inch-diameter (6 mm), giving borehole-diameter-to-cable-diameter ratios of 1.25 and 2.5, respectively.

We first studied empty boreholes to determine collapse mechanisms. Then we included simulated cables to study borehole/cable interaction. Results showed that, for the violent closures required to produce cable damage, collapse was dominated by inward motion of springline rubble. Loading on the cables from springline rubble in dynamic tests was so concentrated that the cables were crimped severely. This crimping occurred at a loading pressure P_V equal to eight times the unconfined compressive strength of the tuff simulant, σ_u, but there were no electrical shorts in the cables. Figure S.2 shows dynamic cable deformation at $P_V = 8\sigma_u$ for both cable sizes.

S.3   CYLINDRICAL STRUCTURES IN JOINTED ROCK

Static uniaxial strain loading tests were performed on jointed rock models containing cylindrical structures to study the effects of joints and joint orientation on tunnel response. Specimens were 12 inches (0.3-m) in diameter and contained 2-inch-diameter (50-mm) circular tunnels.

Figure S.3 and S.4 show posttest sections of two jointed rock models. The specimens consist of a stack of 0.33-inch-thick (8.4-mm) elliptical plates. In one specimen (LSUX-13) the joints are horizontal, and in the other (LSUX-14) they are at a 45° angle ($\pi/4$ rad).

3

1/2-INCH-DIAMETER CABLE

1/4-INCH-DIAMETER CABLE

MP-5762-64

FIGURE S.2   SECTION VIEWS OF SEVERE BOREHOLE AND CABLE
DEFORMATION IN DYNAMIC UNIAXIAL STRAIN TESTS

4
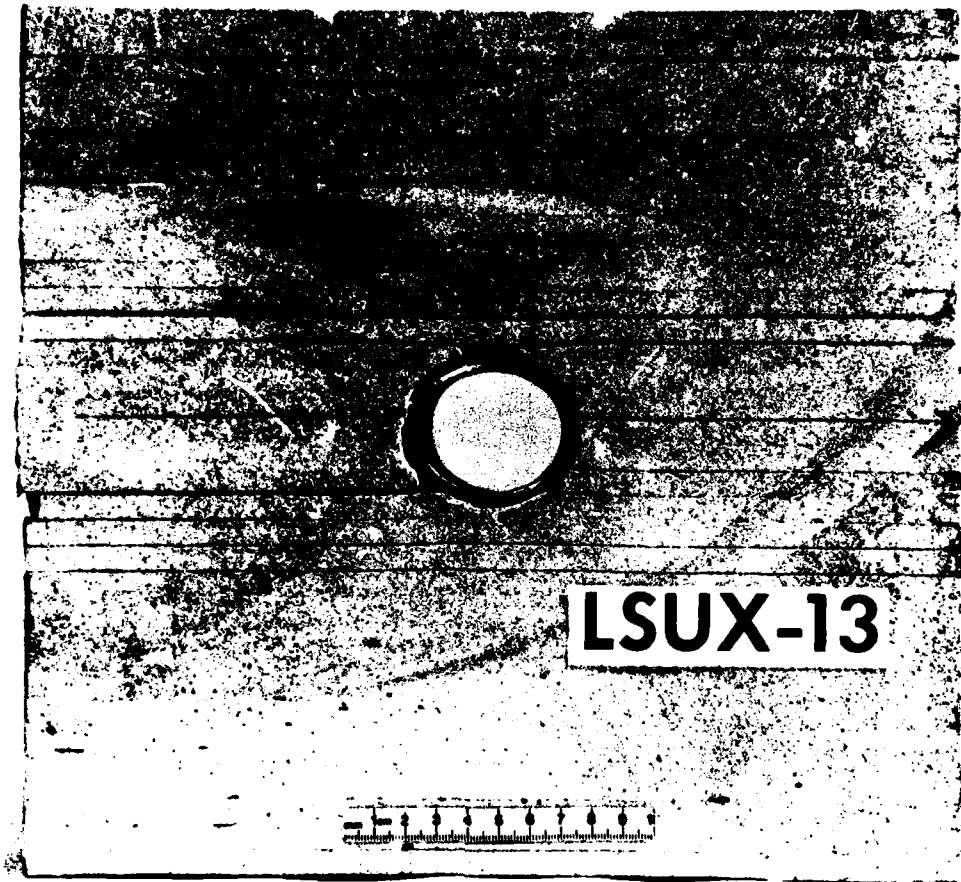
MP-5762-27

FIGURE S.3   SECTIONED SPECIMEN FROM STATIC UNIAXIAL STRAIN TEST LSUX-13
(P_V = 17 ksi, P_H = 7.4 ksi, $\Delta D_V/D_V$ = 10.2%, $\Delta D_H/D_H$ = 0.25%)

5

FIGURE S.4   SECTIONED SPECIMEN FROM STATIC UNIAXIAL STRAIN TEST LSUX-14
(P_V = 12 ksi, P_H = 4.6 ksi, $\Delta D_V/D_V$ = 8.90%, $\Delta D_H/D_H$ = -5.10%)

6

Figure S.5 plots vertical tunnel closure as a function of vertical pressure. The initial jump in tunnel closure is attributed to closing of gaps between the plates. After this initial jump, closure increases smoothly with pressure. Tunnel closure for the 45° joints is significantly larger than for the 0° joints, indicating that the rock-liner structure becomes weaker as the joint angle increases. For comparison, we also plotted vertical tunnel closure data for a test on a 4-inch-diameter (0.1-m) specimen of intact 16A rock simulant. Except for the initial jump, data from this test and the 0° joint test are similar. We therefore conclude that the effect on vertical tunnel closure of a horizontal set of joints is fairly small.

Figure S.6 plots springline tunnel closure as a function of vertical pressure. Springline response of the 0° and 45° joint models was very different. The springlines moved outward initially in both tests as the gaps between the plates closed. For the 0° joints, the springlines were then relatively stationary throughout the test. However, for the 45° joints, the springlines moved steadily outward to a value of 5% as the load increased to its maximum.

S.4   THEORETICAL ANALYSIS OF ELLIPTICAL STRUCTURES

Theoretical analyses were performed to compare the efficiency of elliptical and circular structures under uniaxial strain loading. Previous analysis showed that if the rock around the tunnel remains elastic, an elliptical cross section is more efficient than a circular cross section. For Poisson's ratio in the range of 0.2 to 0.3, the pressure to produce incipient yield around the elliptical cavity is about twice that for the circular cavity.

We performed elastic-plastic analyses to determine whether elliptical cross sections retain their advantage over circular cross sections when the surrounding rock yields. We studied three cases: unlined cavities with no internal pressure, cavities with internal pressure P_i, and cavities with liners that would produce a comparable interface pressure under symmetric loading.

7
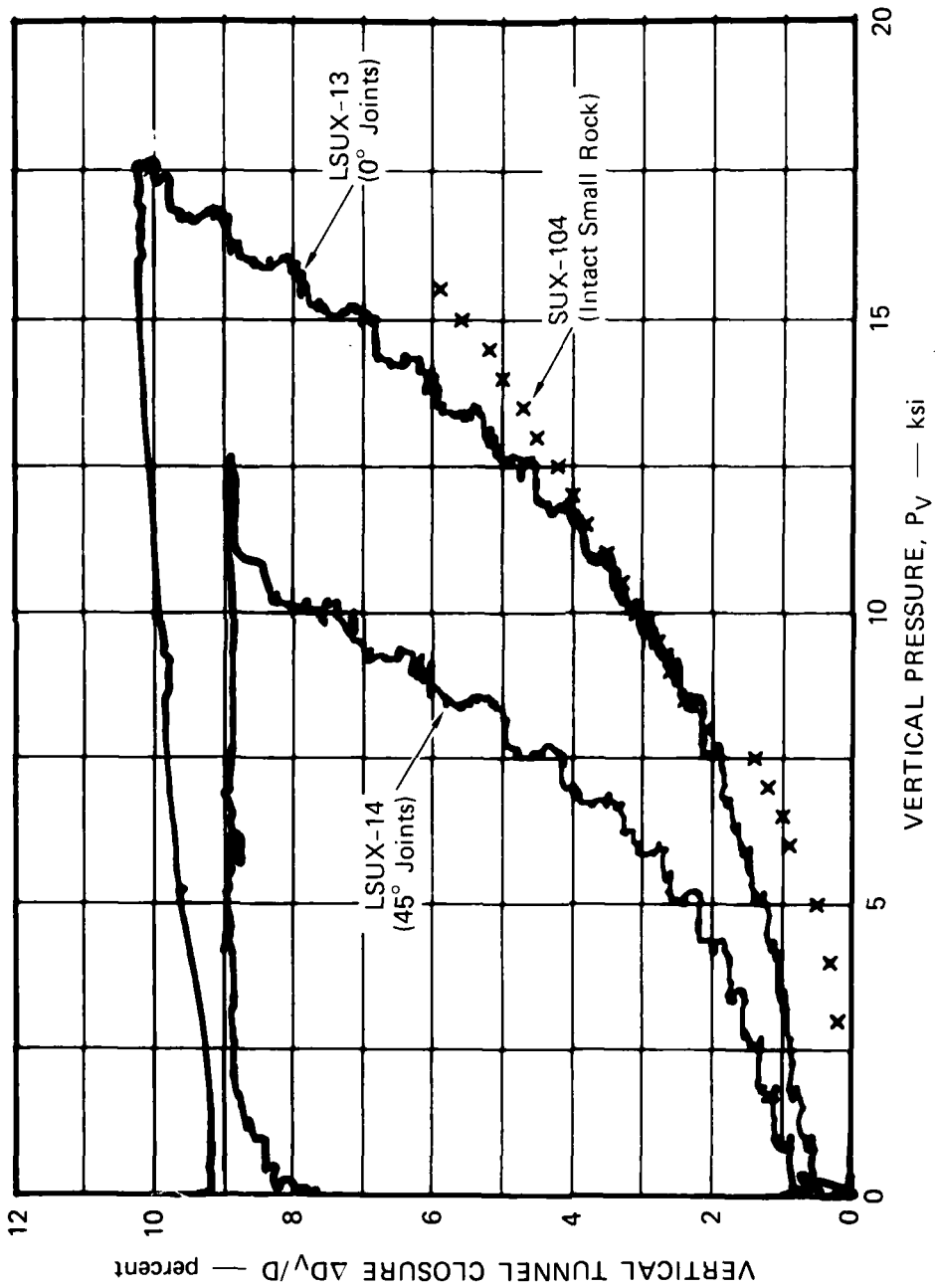
FIGURE S.5   VERTICAL TUNNEL CLOSURE VERSUS VERTICAL PRESSURE FOR UNIAXIAL
STRAIN LOADING OF JOINTED 16A ROCK SPECIMENS

Data from a test on an intact 4-inch-diameter specimen, SUX-104, is plotted for
comparison. 1015 steel liner a/h = 12.5.

8
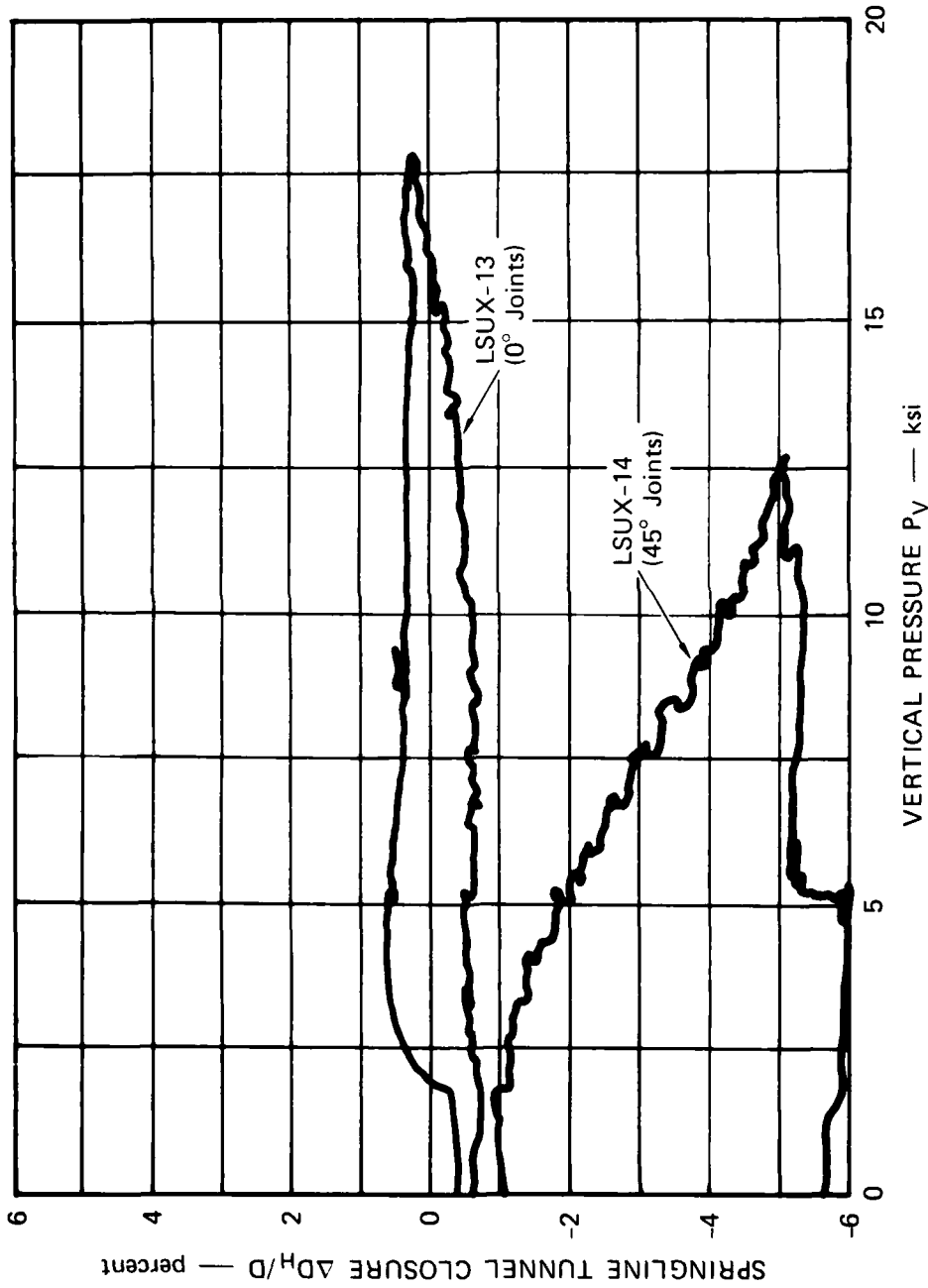
FIGURE S.6   SPRINGLINE TUNNEL CLOSURE VERSUS VERTICAL PRESSURE FOR UNIAXIAL
STRAIN LOADING OF JOINTED 16A ROCK SPECIMENS

1015 steel liner, a/h = 12.5

9

We used the finite element code NONSAP to calculate tunnel closure.
Results showed that when the surrounding medium yields, elliptical
structures are not more efficient than circular structures. As an example,
Figure S.7 plots percentage change in cross-sectional area as a function
of the vertical pressure for all three cases. The elliptical cross
section may suffer less closure at low pressure, but it always suffers
greater closure at high pressure. Calculations showed that elliptical
structures are particularly weak at the springlines. As a result of
this study, we did not field elliptical structures in DIABLO HAWK.

(a) UNLINED CAVITY, $P_i = 0$

(b) CAVITY WITH UNIFORM INTERNAL PRESSURE $P_i = 2000$ psi

(c) LINED CAVITY, MILD STEEL LINER, R/h = 20
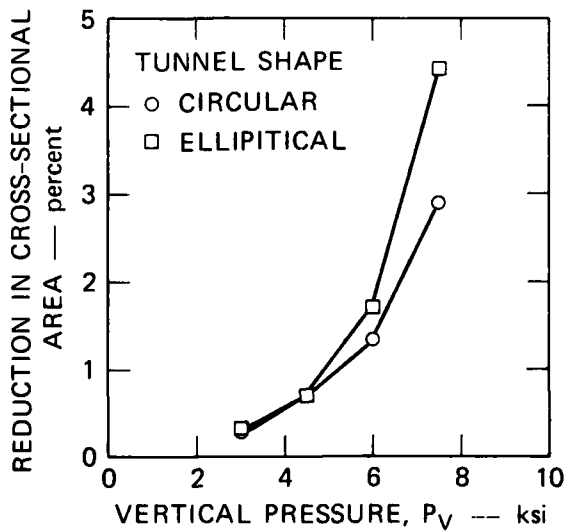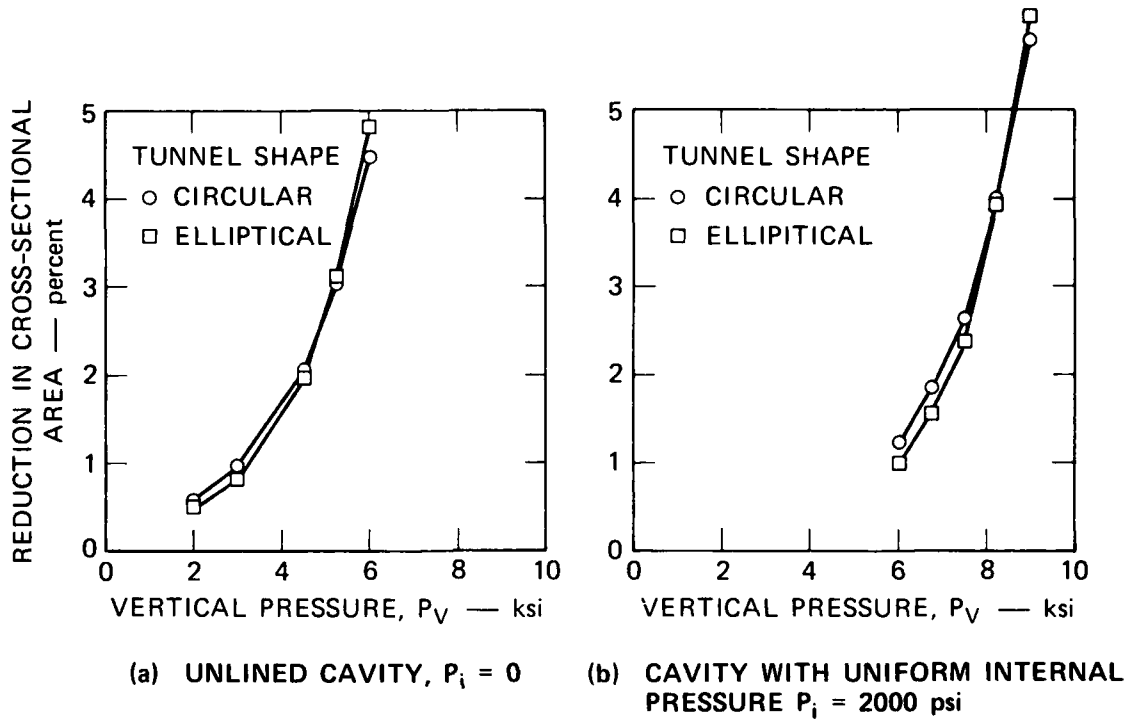
MA-5762-57

FIGURE S.7   REDUCTION IN CROSS-SECTIONAL AREA VERSUS VERTICAL PRESSURE FOR CIRCULAR AND ELLIPTICAL CAVITIES

11

PREFACE

This report describes the first part of a program performed for the Defense Nuclear Agency during the period September 1976 to December 1977 under Contract DNA001-76-C-0385. The technical monitors were LTC D. Burgess and LTC J. Galloway.

The authors gratefully acknowledge the technical support of Paul De Carli, John Busma, George Cartwright, Hugh Hanna, Ed Eckert, Bill Heckman, and Hank Rudnicki.

TABLE OF CONTENTS

LIST OF ILLUSTRATIONS

LIST OF TABLES

1. INTRODUCTION

1.1 BACKGROUND

This report is the fourth in a series [1-3]* of reports that
describe deep-basing laboratory programs at SRI International. It
describes experiments and analyses performed in support of the DIABLO
HAWK event. These laboratory programs investigate the influence of
geological environment and reinforcing structure on response mechanisms
and damage levels in cylindrical cavities at loading pressures typical of
a nuclear burst.

Laboratory testing of scale-model cavities provides an efficient
means of quickly evaluating and developing proposed deep-based structural
concepts so that it is necessary to field only models of the most promising
of these in the underground nuclear tests. Laboratory results also allow
extrapolation of field results to other geological environments. Further,
since in laboratory tests rock properties and specimen boundary conditions
are known, results provide a check on the adequacy of material models
and computer codes used to predict structural response in the field.

1.2 APPROACH AND SCOPE OF INVESTIGATION

We continued our study of deep-based structures by performing labo-
ratory tests to investigate: (1) the effect of loading rate and pore-
water pressure on tunnel closure in SRI RMG 2C2, a tuff simulant;
(2) borehole collapse mechanisms and borehole/cable interaction; and
(3) the influence of joints and joint orientation on tunnel closure in
models containing a single set of joints. We also performed theoretical
analyses to investigate possible advantages of elliptical structures
over circular structures.

---

*Numbers in brackets designate references at the end of the report.

We studied experimentally the influence of several parameters in the rock constitutive behavior on tunnel response. Typical deep-basing geologies are jointed, highly saturated rock. Also, since the weapon loading will be of short duration (although quasistatic), the material response under rapid loading is important. Current analyses used for deep-basing structure design assume that the rock around the structure is intact, isotropic, and homogeneous. Furthermore, parameters in the rock constitutive model are derived from static tests and are taken to be independent of the degree of saturation. It is necessary to study the effects of joints, porewater, and loading rate on tunnel response so that we can develop improved design criteria for deep-based structures. Results of our tests provide a measure of the importance of these parameters in determining tunnel response. Results of tests on jointed rock models also will be used to interpret data from larger scale jointed rock models fielded in DIABLO HAWK.

We studied borehole/cable interaction because hardened communication channels are an important characteristic of deep-based facilities. Cables must be hardened enough to prevent deformation that would distort transmission or even short the cable. Our borehole collapse and borehole/ cable interaction tests provide data on collapse and interaction mechanisms to aid in planning the TRW cable-hardening experiment in DIABLO HAWK and in interpreting the results.

The concept of using elliptical cross sections as super hard structures arises from an elastic analysis that shows that under uniaxial strain loading, elliptical cross sections can carry about twice as much load as circular cross sections. Since at the high loading of many deep-basing scenarios the rock around the cavity yields, it is necessary to study the response of elliptical cross sections in an elastic-plastic medium to determine if they retain their advantage over circular sections.

22

1.3 REPORT ORGANIZATION

The next two chapters give results of experiments in tuff simulants performed in the smaller testing machines. Chapter 2 describes the sensitivity to porewater pressure and loading rate of tunnel closure in SRI RMG 2C2, and Chapter 3 gives results of experiments that investigate borehole collapse and borehole/cable interaction in SRI RMG 2A. The empty borehole collapse experiments can also be interpreted as models of unlined tunnels at extreme damage levels. Then, Chapter 4 describes response of circular structures in models of jointed hard-rock simulant. These tests were performed in the larger machine with more extensive tunnel instrumentation. The comparison of the theoretical efficiency of elliptical and circular structures is described in Chapter 5.

2. TUNNEL RESPONSE UNDER DYNAMIC VERSUS STATIC LOADING

2.1 INTRODUCTION

In a previous program [3], it was observed that to achieve a given tunnel closure, it is necessary to apply a greater pressure to the specimen for dynamic loading than for static loading. In that program only a few isolated dynamic tests were performed because we were interested primarily in comparing the response of several different tunnel liners. In the current program, we performed tests to investigate our earlier observation; we selected a single liner from [3], and obtained more extensive data.

In the previous tests, specimens were fully saturated. In static tests, we allowed water to drain from the specimen at both ends of the tunnel to avoid porewater accumulation at the liner, which causes it to bulge unrealistically [2,3]. In dynamic tests, however, loading is so rapid that porewater migration can be neglected, and we therefore did not permit water to drain from the specimen. Greater porewater pressure in the dynamic tests is a possible explanation for the greater loading pressures required to achieve a given tunnel closure. Another possible explanation is the greater strain rate in the dynamic tests. (Loading rates in the dynamic tests are approximately five orders of magnitude greater than in the static tests.) If deformation of the rock skeleton is sensitive to strain rate in the usual sense, then greater strain rate in the dynamic tests would require higher loading pressures to achieve the same tunnel closure.

To study the influence of both strain rate and porewater pressure on tunnel closure, we tested both dry and saturated specimens. By comparing tunnel closures in static and dynamic tests on dry specimens, we can determine the effect of strain rate on rock skeleton behavior. By comparing tunnel closures in saturated specimens with those in dry

24

specimens for both static and dynamic tests, we can determine the effect of porewater pressure.

These tests were performed with both isotropic and uniaxial strain loading. Table 2.1 shows the test matrix. Procedures for preparing test specimens and using the testing machines have been described in detail previously [2,3]. The specimens used here were 4-inch-diameter (0.1-m), 4-inch-high (0.1-m) cylinders of SRI RMG 2C2, a tuff simulant. Table 2.2 lists the constitutive parameters for both saturated and dry material. Each specimen has a 5/8-inch-diameter (16-mm) tunnel drilled along a diameter at midheight. The tunnels were then lined with a 6061-TO aluminum monocoque cylinder having mean-radius-to-wall-thickness ratio $a/h = 11.5$. The specimens were loaded with hydraulic pumps in static tests and with explosive gas sources in dynamic tests. For isotropic loading, we use only one hydraulic pump or explosive gas source. For uniaxial strain loading, however, two are required: one to apply the vertical loading pressure and the other to apply the lateral confining pressure needed to maintain uniaxial strain.

In the next two sections we present results of the isotropic and uniaxial strain loading tests. The results of both loading types are in discussed in the final section.

2.2 ISOTROPIC LOADING TESTS

Figure 2.1 shows tunnel closure versus applied pressure results from the isotropic loading tests. Data from saturated specimens are plotted as solid symbols and from dry specimens as open symbols. From static tests we obtain the entire tunnel closure versus applied pressure curve (triangles in Figure 2.1) whereas we obtain only the posttest tunnel closure from dynamic tests[*] (hexagons in Figure 2.1). The posttest

---

[*] Springback from the peak closure in static tests was less than 0.2%, and hence is neglected in the dynamic data. In larger rock specimens (0.3-m diameter), the tunnel is 50 mm in diameter, large enough to install an LVDT (linear variable differential transformer) that can measure instantaneous closure throughout the test under both dynamic and static loading. (See Appendix A). A few dynamic tests with more complete instrumentation are planned for future experiments.

Table 2.1

SRI RMG 2C2 TEST MATRIX

		Load Type		
	Static		Dynamic	
Specimen	Isotropic	Uniaxial Strain	Isotropic	Uniaxial Strain
Dry	SI-115	SUX-103 SUX-114	DI-94, DI-95 DI-96, DI-97 DI-98	DUX-77, DUX-78 DUX-81, DUX-83
Saturated	SI-92	SUX-94	DI-65, DI-99 DI-100, DI-101	DUX-73, DUX-79 DUX-80, DUX-82

Table 2.2

CONSTITUTIVE PARAMETERS FOR SRI RMG 2C2

	Saturated	Dry
Young's Modulus, E^a	1.15×10^6 psi (7.9 GPa)	1.15×10^6 psi (7.9 GPa)
Poisson's Ratio, ν^b	0.23	0.20
Compressive Strength, σ_u^a	3675 psi (25.35 MPa)	3675 psi (25.35 MPa)
Friction Angle, ϕ^b	2.5^o (0.044 rad)	15° (0.262 rad)

[a] Determined from unconfined compression tests.

[b] Determined from uniaxial strain tests.

26
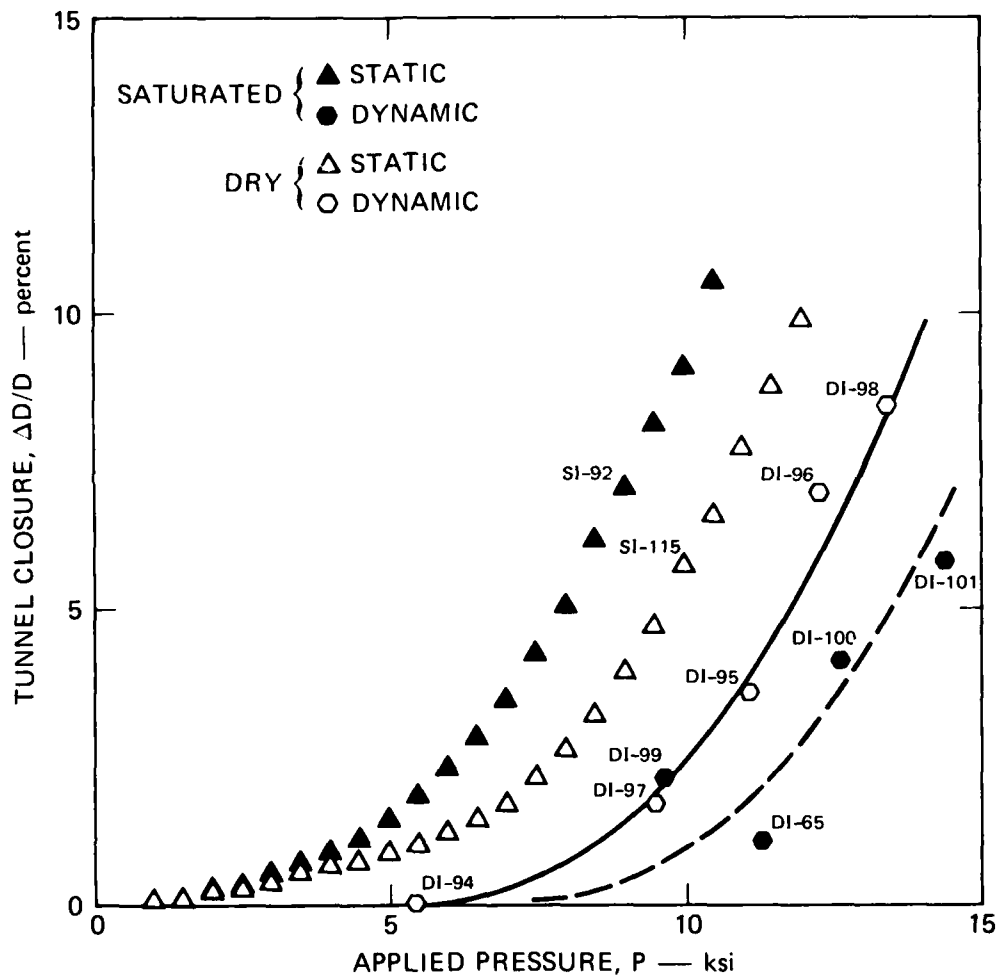
FIGURE 2.1   TUNNEL CLOSURE VERSUS APPLIED PRESSURE FOR ISOTROPIC
LOADING OF SRI RMG 2C2. LINER: 6061-T0 ALUMINUM,
a/h = 11.5

tunnel closure is plotted as a function of the peak loading pressure
for each of the nine dynamic tests. A solid line drawn through the five
dynamic data points for dry specimens gives a good fit, demonstrating
repeatability of the tests. The curve has the same shape as the locus
of static data points. There are fewer data and some scatter in the
points from the dynamic tests on saturated specimens, so the dashed
curve through the solid hexagons is obtained by shifting the solid curve
by 1.5 ksi (10.3 MPa) to obtain a reasonable fit.

Tunnel closure data from the dry specimens, both static and dynamic,
lie between the static and dynamic data for saturated specimens. This
indicates that saturated specimens are weaker than dry specimens under
static loading but stronger under dynamic loading. Thus, the role of
porewater in determining tunnel closure differs significantly between
static and dynamic tests. For example, to achieve 5 percent closure
requires a loading pressure on the saturated specimen about 20 percent
less than on the dry specimen for static loading, but about 15 percent
greater for dynamic loading.

The role of strain rate in determining tunnel closure is found by
comparing the static and dynamic data for dry specimens. To achieve 5
percent closure in a dynamic test requires about 20 percent more pressure
than in a static test, and this is due solely to the difference in strain
rate. If the effect of porewater pressure is included in addition to
strain rate (compare saturated static and dynamic tests), the difference
in loading pressures increases to about 70 percent.

These results are discussed in more detail in Section 2.4. The
important point to note for the following discussion is that tunnel
closure is influenced by differences in both strain rate and porewater
pressure.

28

2.3 UNIAXIAL STRAIN LOADING TESTS

The uniaxial strain loading results are similar to the isotropic loading results just presented. However, to help in interpreting tunnel closure versus applied pressure results, we need to review briefly our uniaxial strain loading test procedures. In the isotropic loading tests, only one loading source is used (hydraulic pump or explosive gas source), and the pressures on the ends and lateral surface of the specimen are equal. In the uniaxial strain loading tests, two loading sources are needed: one to apply the loading pressure on the ends of the specimen (vertical pressure, P_V), and one to apply the confining pressure to the lateral surface of the specimen (lateral confining pressure, P_H). In a uniaxial strain loading test the lateral confining pressure must be adjusted to maintain zero radial displacement (equivalent to zero circumferential strain) at the specimen lateral surface.

In our tests, we monitor the circumferential strain at two stations, diametrically opposed, and adjust the lateral confining pressure to give a zero sum of the output of the two gages. In static tests, this is easily accomplished; after each small increment in vertical pressure, the lateral confining pressure is increased until the sum of the strain gage outputs is zero. Figure 2.2 shows a plot of lateral confining pressure P_H versus vertical pressure P_V for static uniaxial strain loading. The uniaxial strain load paths for saturated and dry specimens are not the same. Both load paths can be approximated as piece-wise linear. The first linear segment corresponds to elastic behavior and its slope is $\nu/(1 - \nu)$, where ν is Poisson's ratio. The second linear segment corresponds to plastic behavior and its slope is $(1 - \sin\phi)/(1 + \sin\phi)$, where ϕ is the angle of internal friction. The values for Poisson's ratio and the friction angle obtained from Figure 2.2 are those reported in Table 2.2.

In dynamic tests, however, load control is open loop. We choose the explosive charge size to produce peak pressures on the static uniaxial strain load path, but the path followed is adjusted by adjusting the testing machine characteristics, not by feeding back lateral strain

29
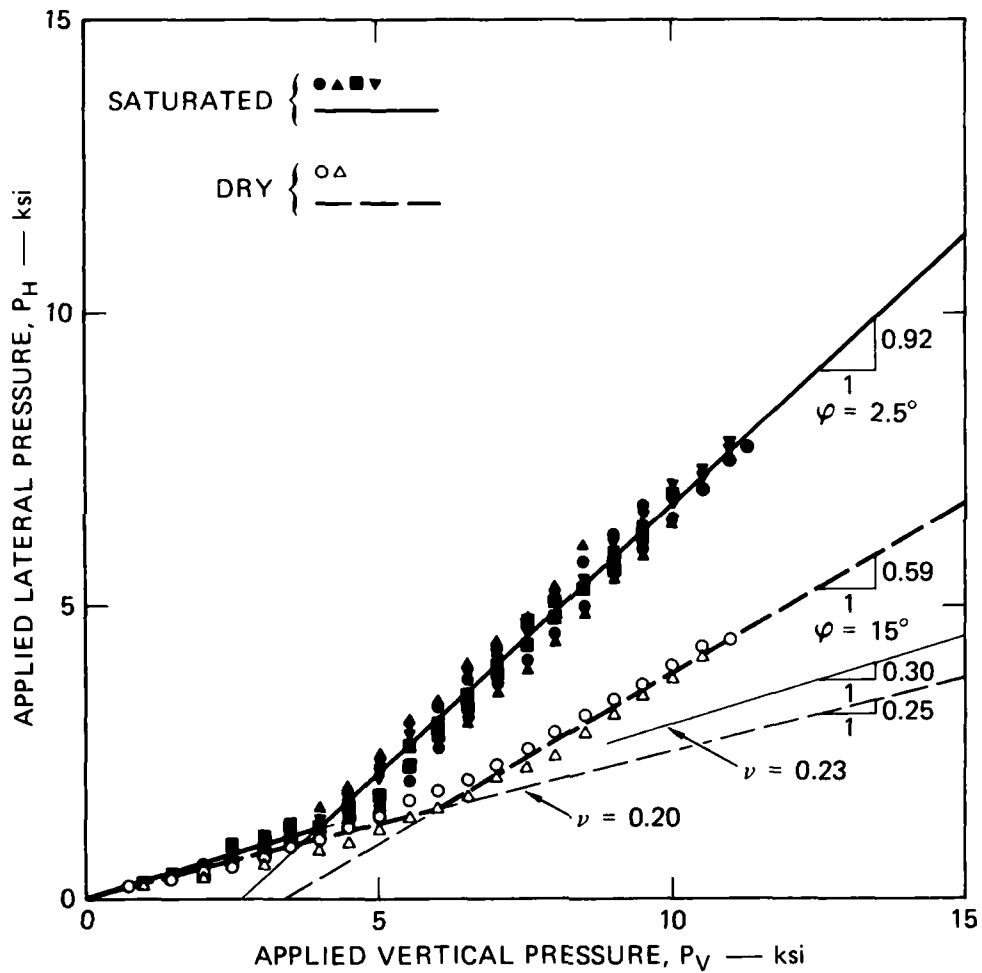
FIGURE 2.2 LATERAL CONFINING PRESSURE VERSUS VERTICAL PRESSURE
NEEDED TO MAINTAIN UNIAXIAL STRAIN CONDITIONS IN
SRI RMG 2C2

30

as in the static tests. We can tune the testing machine to bring the dynamic load path into fairly close agreement with the static uniaxial strain load path, but the latter path may not produce uniaxial strain in dynamic tests because of differences in material response. To determine how much the dynamic deformation field deviates from uniaxial strain, we record the output of the two strain gages mounted on the specimen. We found in some tests that the lateral surface of the specimen moved inward, indicating that the lateral confining pressure was too large and the specimen was overconfined. In other tests, the lateral surface of the specimen moved outward, indicating that the lateral confining pressure was too small and the specimen was underconfined. Thus, because we have found that tunnel closures are larger for underconfined specimens [3], we take vertical tunnel closures measured in underconfined tests as upper bounds to uniaxial strain loading tunnel closures, and tunnel closures measured in overconfined tests as lower bounds. We will see that upper and lower bound vertical loading pressures at 5 percent closure differ by about 20 percent. Details and examples of pressure and strain-time histories are given in [3].

Figure 2.3 plots vertical tunnel closure as a function of applied vertical pressure for the uniaxial strain loading tests. As in the plot of isotropic results, data from saturated specimens are plotted as solid symbols and data from dry specimens as open symbols. The dashed lines in this figure are upper and lower bounds on the dynamic uniaxial strain loading closure in dry specimens. For saturated specimens, only a lower bound was obtained. An exception is the complete closure in DUX-82, but this is not a useful upper bound.

Qualitatively, the results are identical with those from the isotropic loading tests; that is, the tunnel closure data from the dry specimens, both static and dynamic, lie between the static and dynamic closure data for the saturated specimens. At 5 percent closure, the pressure on the saturated specimen is 20 percent less than on the dry specimen for static loading, about the same as for the isotropic loading. A rough extrapolation of the dynamic lower bound data for saturated specimens to 5 percent closure indicates that about 15 percent more pressure is required than for the dynamic lower bound data for dry specimens. Again, this is about the

31
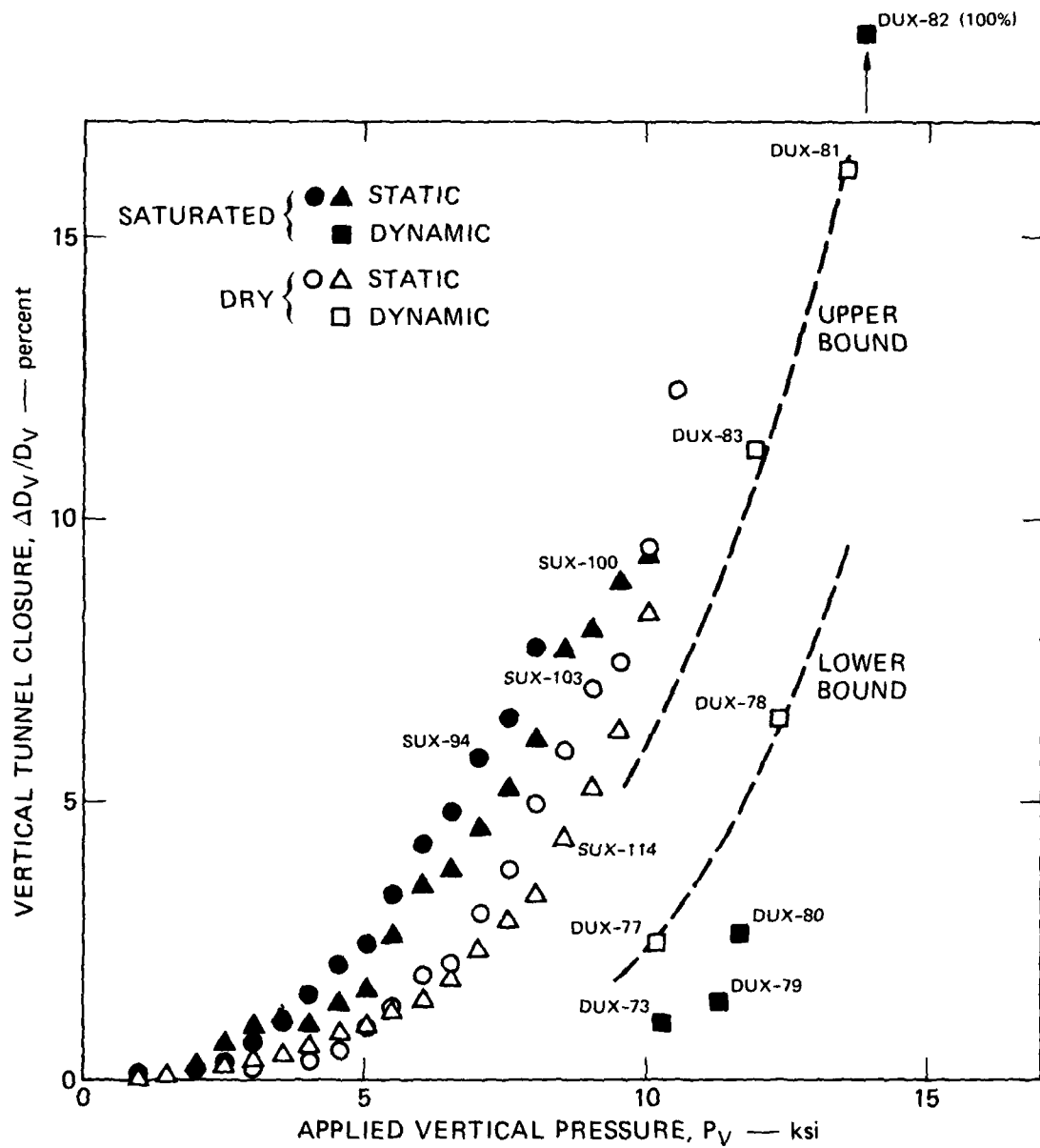
FIGURE 2.3   VERTICAL TUNNEL CLOSURE VERSUS APPLIED VERTICAL PRESSURE FOR
UNIAXIAL STRAIN LOADING OF SRI RMG 2C2.   LINER: 6061-T0
ALUMINUM, a/h = 11.5

Dashed lines represent upper and lower bounds to tunnel closure under dynamic
uniaxial strain loading for dry SRI RMG 2C2.

32

same as for isotropic loading. It is more difficult to quantify the effect of strain rate in the uniaxial strain tests because we do not know just where the dynamic uniaxial strain data lie. However, using the upper and lower bounds at 5 percent closure, we find the difference in strain rate can require a 10 to 40 percent increase in pressure. For isotropic loading the increase in pressure due to strain rate was about 20 percent.

2.4 DISCUSSION OF RESULTS

We performed the tests described above to study the large difference between tunnel closures measured in static and dynamic tests on saturated specimens [3]. Tests on dry as well as saturated specimens were conducted to separate the effects of strain rate from porewater pressure. We can determine the influence of strain rate by comparing static and dynamic test results for dry specimens, and the influence of porewater pressure by comparing results from tests on saturated specimens with those from tests on dry specimens. The influence of strain rate is discussed first.

From our isotropic and uniaxial strain loading tests on dry specimens of SRI RMG 2C2, we found that the greater strain rates in dynamic tests required that the loading pressure be increased by between 10 and 40 percent to produce a 5 percent closure. This range of increased pressure can be reduced to between 20 and 30 percent by assuming that the actual dynamic uniaxial strain loading data do not lie close to either of our bounds. This magnitude increase of strength with strain rate has been observed in concrete [5] and a number of clays and sands [6-8], and is probably typical of most soft rocks.

Porewater pressure weakens the specimen in static tests, but strengthens it in dynamic tests. It is generally accepted that porewater pressure reduces the shear strength and stiffens the hydrostat of rocks under static loading [9]. The effect of porewater pressure on shear strength is shown schematically in Figure 2.4. Porewater pressure reduces the friction angle from that of the effective stress (total stress less porewater pressure) Mohr envelope to that of the total stress Mohr

33

EFFECTIVE STRESS
MOHR ENVELOPE

TOTAL STRESS
MOHR ENVELOPE

$\sigma_1' = \sigma_1 - p$

σ_1

$\sigma_2' = \sigma_2 - p$

σ_2
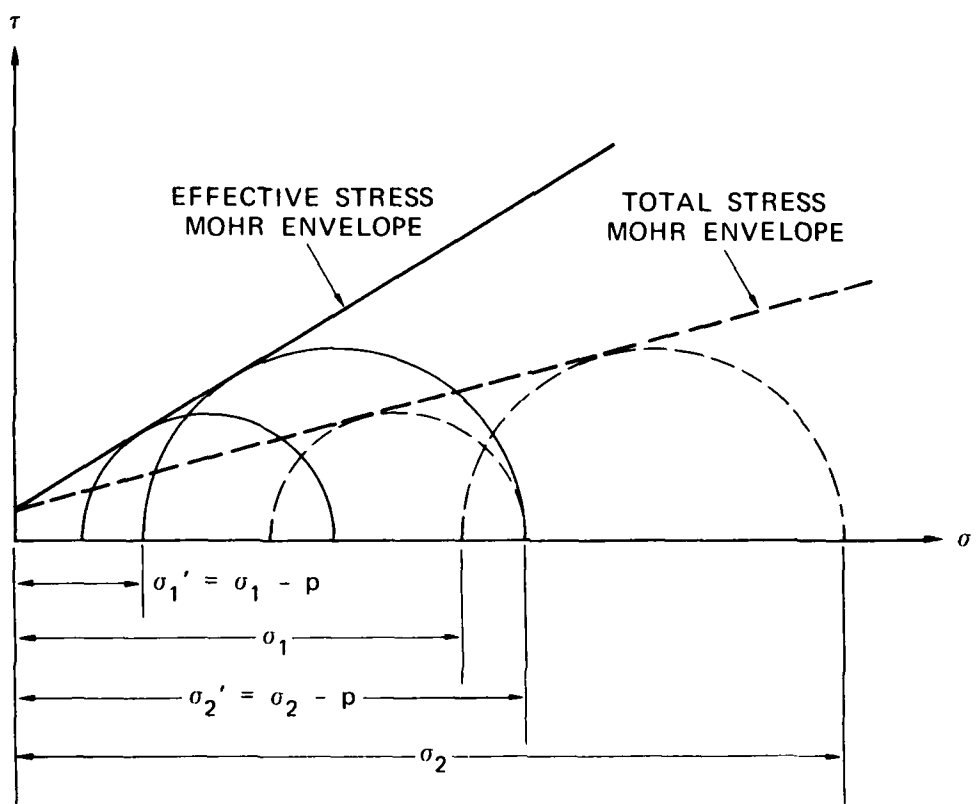
MA-3743-30

FIGURE 2.4   EFFECT OF PORE PRESSURE ON MOHR FAILURE ENVELOPE

34

envelope. For SRI RMG 2C2, the reduction in friction angle is from 15° (0.262 rad) to 2.5° (0.044 rad). Stiffening of the hydrostat in static tests is probably reduced because porewater is permitted to drain. In dynamic tests there is no time for porewater migration, and even though porewater pressure may still reduce the shear strength, the stiffening due to porewater pressure is not lost. For a simple example of porewater stiffening, we consider the elastic response of a body containing a cylindrical cavity subjected to a free field pressure P_o, an internal cavity pressure P_i, and a porewater pressure p. Straightforward elastic analysis [10] shows that the radial displacement u is

$$u = \frac{(1 + \nu)}{E} (P_o - P_i) \frac{a^2}{r} + \frac{(1 + \nu)(1 - 2\nu)}{E} (P_o - p) r$$

where E is Young's modulus, and ν is Poisson's ratio. We see that as p increases, u decreases. Thus, porewater pressure makes the material appear stiffer, since the deformation for a given free-field pressure is smaller with porewater pressure than without.

Our experiments show that effects of porewater pressure are more important than the effect of strain rate. However, both porewater pressure and strain rate should be accounted for in deep-base structure design and when comparing field, laboratory, and theoretical results.

3. BOREHOLE/CABLE INTERACTION

3.1 BACKGROUND

3.1.1 Relationship with DIABLO HAWK

On October 6, 1976, Milton Schrader, Peter Dai, and Edward Lobherr of the TRW Systems' Vulnerability and Hardening Laboratory met at the DNA Nevada Operations Office with Herbert Lindberg of SRI International to discuss the possibility of a laboratory program to study cable-borehole interaction. The objective of the program was to assist in the design and interpretation of the TRW cable hardening experiments being fielded in the DIABLO HAWK event. A first-draft test program was mutually agreed upon then submitted to LTC Danny N. Burgess for consideration. This chapter describes the results of the program as finally agreed upon with LTC Burgess and carried out in cooperation with Milton Schrader of TRW.

A description of the technical background for the program was prepared by TRW as part of the program plan and is given below. This background shows their approach to the analysis and interpretation of the DIABLO HAWK borehole/cable interaction experiment and to the laboratory program. With this background, we can make several useful comparisons as the overall program **progresses in the following steps:** TRW pretest analysis, SRI laboratory experiments, TRW reevaluation of the pretest analysis, the DIABLO HAWK experiment itself, and TRW interpretation of the DIABLO HAWK results. The TRW background description has been edited for consistency of style, but the technical content remains the same.

3.1.2 Technical Background

A report on command center facilities for the post-1985 Worldwide Military Command and Control Systems (WWMCCS) prepared for DCA concluded that a deeply buried command center for the National Military Command System (NMCS) is an attractive option, based on an evaluation of performance, survivability, and cost. Subsequent actions by the Joint Chiefs of Staff, the Office of the Secretary of Defense -DTACCS, and the WWMCCS Council have set in motion a Deep-Basing R&D program. The major thrust of the R&D program will be to identify and reduce technical, schedule, and cost risks in deep-based systems implementation. Hardened communications cables are important for linking the deeply buried center with the surface facilities. A key area of concern, therefore, is the uncertainty in the hardness of the cable system, which may lead to a substantial overdesign of the system to achieve the required survivability with sufficient confidence.

As part of the surface link from the deep underground command center (DUCC), the cable system may be critical to the operation of a deep-based command center during an attack. NMCS general war communications requirements include missile warning/attach assessment, Commander in Chief (CINC) conferencing, Emergency Action Message (EAM) dissemination, Residual Capability Assessment (RECA), and negotiation. The transattack data rate requirement in support of general war functions may exceed one megabit per second. If the cable circuits are destroyed, the alternative communications modes, a very low frequency (VLF) or extremely low frequency (ELF) mode, can support only very low data rates.

The baseline configuration of the cable system for the command center/surface accesses consists of cable runs in:

- Deeply buried tunnels (fixed to walls or emplaced in a bed of sand), at the level of the deep-based facilities.

- Vertical boreholes (5000 feet) to the surface (suspended from the top only, at discrete points along their length, or uniformly by backfill).

- Trenches near the surface between surface facilities
  (placed in crushed backfill in rock or plowed in
  soil for surface trench emplacements).

The communication link envisioned for the system is an armored
communication cable with multiple solid dielectric coaxial conductors
for wideband communication capability. Armored cable will provide the
strength required to support the suspended cable during ground shock
acceleration loading, and to resist borehole crushing and shearing.

A report prepared by TRW for the Defense Communication Agency
(DCA) on the DUCC cable survivability focused on the fragility of a
cable in a long vertical borehole. The two primary cable loading sources
and corresponding damage mechanisms associated with the nuclear ground
shock environment are:

- Free-field stress, which contracts and collapses the
  borehole, resulting in crushing deformation of the
  cable and its coaxial conductors.
- Relative motion, which shears the borehole and cable,
  resulting in shearing and large local stretching of
  the coaxial conductors.

Under extreme environments, both of these mechanisms can produce an
electrical short (or near short) condition in one or more of the coaxial
conductors, resulting in loss of communication. This laboratory program
concentrates entirely on the first mechanism--cable crushing caused by
borehole collapse.

The TRW report separated the problem of hardened cable crushing
into:

- Borehole fragility (unlined and cased)
- Cable fragility
- Borehole/cable interaction

Since cable crushing can occur only as a result of large borehole deformation, TRW first determined borehole response and collapse loads for large deformations by making large deformation finite element calculations with simple elastic-plastic material models. Loading was taken as a pseudo-static, uniaxial-strain load with the free field stress of σ_{ff} lateral to the borehole. Existing laboratory and field data were used to interpret the results for more realistic materials. TRW concluded that collapse loads are about three times the unconfined strength of the rock material ($\sigma_{ff} = 3\sigma_u$).

Interaction between the collapsing borehole and the cable is quite complex; however, the cable failure stress σ_{PL} under rigid platen loading can be considered to be a lower bound free field stress to produce shorting. Another lower bound is the free field stress required to collapse the borehole in the absence of a cable, shown by the line $\sigma_{ff} = 3\sigma_u$ in Figure 3.1. The PILEDRIVER fragility data shown fall below the $3\sigma_u$ line because of borehole shearing. The mechanical properties and platen fragility shown are for a typical complex hardened cable tested in the laboratory.

For hard rock media, the borehole/cable fragility would be essentially equal to the borehole collapse load, as shown in Figure 3.1. As the unconfined strength of the medium decreases, borehole/cable interaction effects become more significant. As the collapsing borehole closes around the cable, the interaction loads resist closure and cable flattening. Since no test data exist for evaluating the borehole/cable interaction effects, engineering judgment is used to extrapolate the cable shorting fragility from the lower bound curves:

$$(\sigma_{ff})_{\text{cable shorting}} = 3\sigma_u + \sigma_{PL}, \quad \sigma_{PL} > 1500 \text{ psi}$$

where σ_{PL} is the cable shorting stress under a platen load. This approximation is crude because we lack the experimental data required to understand the interaction of the cable with the plasticized rock,

SOIL   SOFT ROCK   HARD ROCK

BEST ESTIMATE BOREHOLE
COLLAPSE CURVE

$\sigma_{ff} = 3\sigma_u$

PILEDRIVER
DATA

NTS
AREA U12
WET TUFF

BEST ESTIMATE CABLE
FAILURE CURVES

$\sigma_{ff} = 3\sigma_u + 3.5$ ksi

$\sigma_u > 1.5$ ksi

?

PLATEN LOADING TEST

3.5 ksi

100   10   1

σ_{ff} (ksi)

FREE FIELD ROCK STRESS

0.01   0.1   1   10   100

UNCONFINED COMPRESSIVE STRENGTH σ_u (ksi)
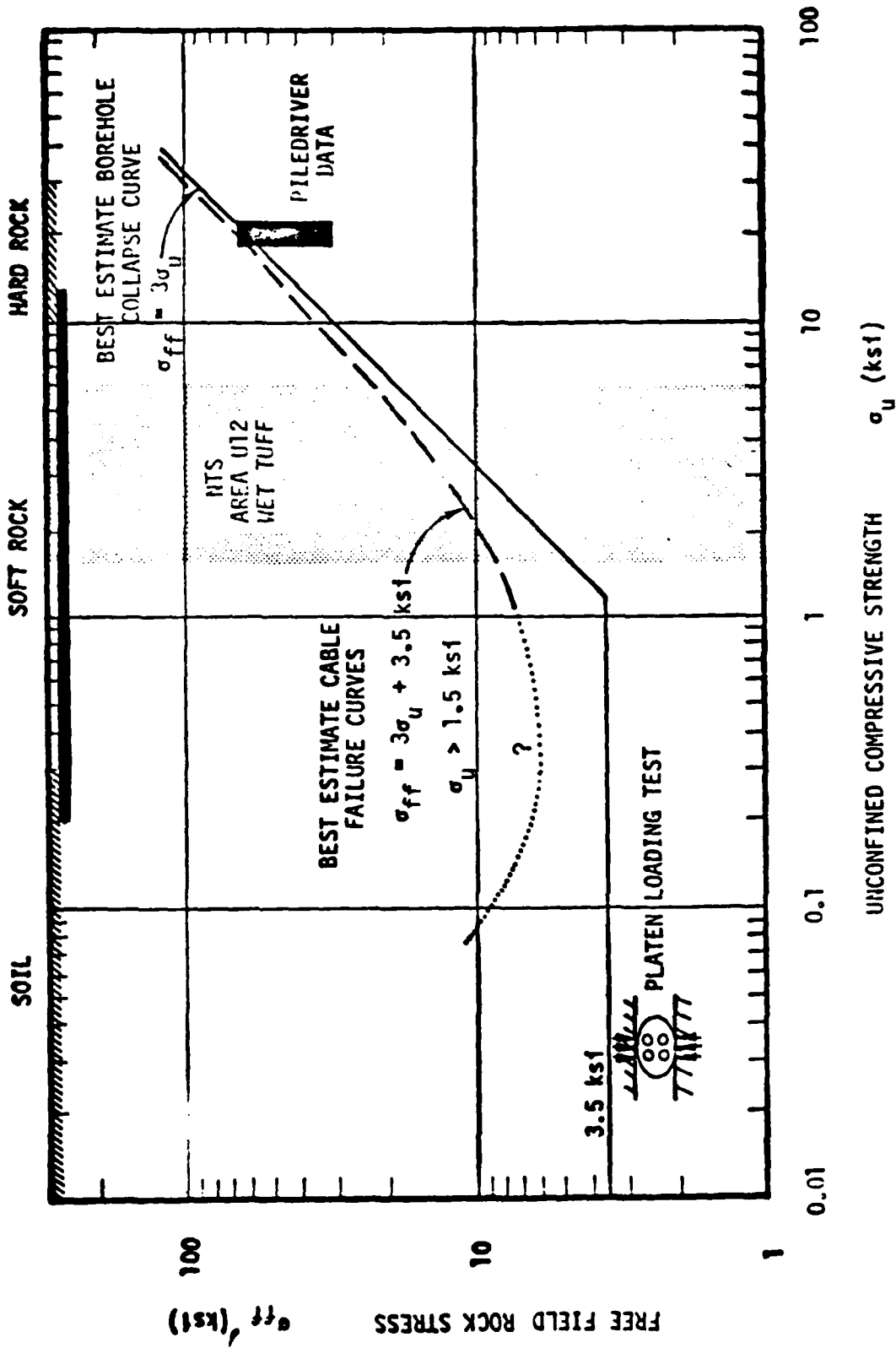
MA-317583-76

FIGURE 3.1   TRW BOREHOLE/CABLE INTERACTION MODEL

40

effects of debris within the borehole, and sensitivity of response to borehole-to-cable diameter ratio.[*]

As a result of the uncertainties associated with borehole/cable interaction and cable damage, a cable survivability experiment was recommended for inclusion in the DIABLO HAWK event. DIABLO HAWK offers an opportunity to investigate cable damage from borehole collapse in a relatively weak test bed rock where a hardened cable would have its largest influence on the rock response. Uncertainties in material parameters and how they affect response dictate the number of test cables and the range of test stations required for the DIABLO HAWK cable experiment, and therefore, the cost of the experiment.

As outlined above, uncertainties in how to use the material parameters in calculating response are just as important as uncertainties in the parameters themselves. These uncertainties will influence our interpretation of results from the DIABLO HAWK test as well as limit our ability to make an effective test plan before the event. The purpose of the laboratory program is to reduce these uncertainties by testing in the laboratory, where we can work with known material and load parameters and where we will be able to observe the complex response in detail as it happens.

3.2   OBJECTIVES

The general objectives of the laboratory program were to provide:

(1)   Better qualitative understanding of the borehole/cable interaction mechanisms.

(2)   Improved quantitative definition of the borehole/cable interaction.

(3)   Reduced systematic uncertainty assocated with borehole/cable interaction.

---

[*] All of these questions were addressed in the laboratory program. The results will provide a basis for an improved analysis in which these effects will be taken into account.

The first two objectives can provide data for development of rational analyses that can be used to improve fragility estimates (e.g., improve the curves of Figure 3.1). All the objectives are directed toward the immediate application of improving the DIABLO HAWK experiment. Even though the DIABLO HAWK planning was nearly complete before the laboratory program was begun, the improved understanding of borehole/cable interaction permitted reevaluation of the cable experiment plan and will assist in interpreting the results.

In addition to assisting in DIABLO HAWK planning and interpretation, the laboratory experiments will allow us to compare scaled experiments in a relatively homogeneous laboratory medium with those in a more realistic nonuniform medium in the field. The laboratory data can aid in the post-DIABLO HAWK anaylsis by providing a basis for resolving potential anomalies in the DIABLO HAWK experiments. Comparisons of laboratory and underground nuclear test data may establish the validity of such laboratory testing as a option for future testing. Although laboratory testing would not eliminate the need for field testing to validate the final cable design to be used in a DUCC system, it may provide a valuable design tool for evaluating the borehole/cable interaction of intermediate designs of the hardened DUCC cable.

3.3   APPROACH

The approach in the laboratory program followed the three parts of the cable crushing problem as identified by TRW:

- Borehole fragility
- Cable fragility
- Borehole/cable interaction

SRI investigated borehole fragility and borehole/cable interaction while TRW investigated cable fragility and prepared scale-model cables to be tested at SRI.

42

3.3.1 Test Plan

The program consisted of 15 borehole tests with and without
simulated cables in simulated tuff. In all but three dynamic tests to
examine the effect of lateral confining pressure, loading was applied
to simulate as closely as possible a uniaxial strain field (simulating
side-on loading in the field). Ten tests were performed with dynamic
loading, to more closely simulate the loading in DIABLO HAWK and five
with static loading, to allow active load control and to investigate
effects of springline rubble. In the dynamic tests, pressures were
selected to produce slight, moderate, and severe damage for both empty
boreholes and boreholes with large and small cables. In the static tests,
complete load versus closure curves were measured for empty boreholes,
with springline rubble removed as it appeared; then tests were run with
large and small cables up to the maximum pressure applied in the dynamic
tests. A static test was also run until complete closure of an empty
borehole occurred; springline rubble was not removed in this test.

3.3.2 Rock Modeling

Figure 3.2 illustrates the relationship between strength pro-
perties of grout simulants and the strength measured for tuff samples
taken from corings near the MIGHTY EPIC/DIABLO HAWK structure drifts.
The shaded area encloses all the data points from 31 triaxial strength
tests performed by Terra Tek and by Waterways Experiment Station (WES).
These data encompass all the 15 core samples tested except for one sample
from I5S #7 at 21 feet, which appears to be from a narrow slab with a
strength about twice that of the upper bound curve in Figure 3.2. The
straight line labeled Tuff 2 is a good constant-friction-angle fit to
the average data for confining stresses less than about 0.5 kbar, the
region of interest for the structure experiments in MIGHTY EPIC/DIABLO
HAWK. This line is described by an unconfined strength σ_u = 0.2 kbar
(20 MPa) and a friction angle ϕ = 18°. Together with Young's modulus
E = 0.6 x 10^6 psi (4.1 GPa) and Poisson's ratio ν = 0.28, it describes
the ideal material being used for analysis by the DNA structures community.
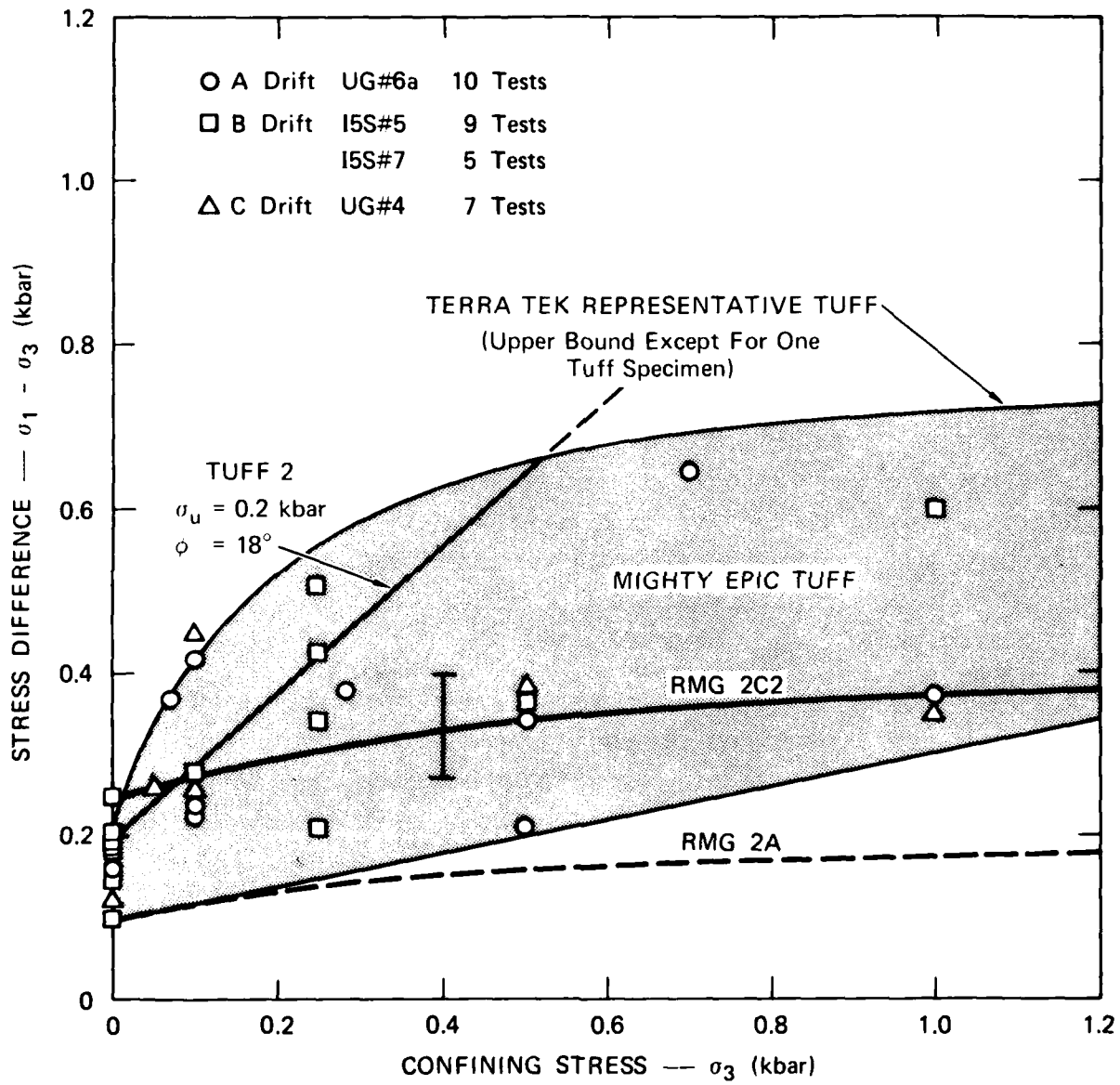
FIGURE 3.2   FAILURE ENVELOPES FOR MIGHTY EPIC TUFF AND GROUT SIMULANTS
(Source for Tuff data: Terra Tek Report TR 76-21, April 1976, pp. 9, 44, 45).

MA-317583-77

44

The line is drawn dashed for confining stresses above $\sigma_3 = 0.5$ kbar (50 MPa) because its use is not appropriate in this range.

For the large borehole closures anticipated for cable crushing, the stress state in the tuff will extend over a broad area of the yield surface; that is, there will be a large yield region around the borehole so that σ_3 will extend from zero at the borehole to large values away from the borehole. The tuff simulant labeled RMG-2C2 is a reasonable approximation over this range, although its friction is lower than ideal. Because of its low friction, it is near the upper bound tuff curve at $\sigma_3 = 0$ and near the lower bound curve for $\sigma_3 = 1$ kbar (100 MPa).

Model borehole response in this material would be representative of response in medium strength tuff in the MIGHTY EPIC area. However, based on our experience with this simulant in our laboratory investigation of deep-based structures, we are not sure if we can produce dynamic borehole collapse within the 1-kbar dynamic pressure capability of our dynamic test machine. We can collapse a borehole in this material statically because the static machine has a 2-kbar capability. However, to ensure that we could carry through both the dynamic and static collapse and borehole/cable interaction experiments, we used the weaker simulant labeled RMG-2A in Figure 3.2. Components and mechanical properties of this simulant are given in Table 3.1.

3.3.3 Cable Modeling

There are two approaches to cable modeling with the weaker tuff. The most straightforward approach is to model the cable with the same strength (platen stress σ_{PL}) as measured on the full-scale cable. Then borehole/cable interaction will be near a maximum and, also, the results will provide a conservative bound on cable survivability in tuff at the NTS test bed. That is, because RMG-2A has a yield envelope slightly lower than the weakest measured tuff properties, the laboratory pressure needed to cause cable crushing will be smaller than those expected in the field.

45

Table 3.1

COMPONENTS AND MECHANICAL PROPERTIES OF SRI RMG-2A GROUT

Component or property	Percent of weight or property value
Cement (Portland, Type 1 or Class G)	23.93
Sand (Monterey, 20-40 mesh)	19.76
Barite (Ba SO_4)	26.24
Bentonite	2.58
CFR2 (Friction-reducing compound, detergent powder)	0.072
Water	27.45
Total	100.03
Cure time (dry heat, days)	7
Density (kg/m^3)	203
Young's modulus (uniaxial compression, psi[*])	1×10^6
Poisson's ratio (from uniaxial-strain P_H vs P_V)	0.20
Friction angle (degrees, from uniaxial-strain P_H vs P_V)	4.3
Unconfined compressive strength (psi[*])	1500

---

[*] 1 psi = 6.9 kPa.

The second approach is to model the cable with half the strength of the full-scale cable. Then the yield envelope of the RMG-2A simulant would appear to this cable approximately as the RMG-2C2 simulant appears to the full-scale cable. The laboratory experiments would be performed with all stress quantities reduced by a factor of two compared with the full-scale prototype cable in NTS tuff. This second approach has the advantage that we would be modeling more nearly average strength behavior of tuff rather than lower bound strength behavior. Thus, the borehole/ cable interaction would more closely represent that expected in the field. The laboratory pressure required to cause cable collapse, multiplied by two, the stress scale factor, would give an estimate of the pressure required to cause collapse in average tuff. This assumes that the TRW platen test is a valid measure of cable strength for the more complex deformations in actual borehole/cable interaction.

TRW used the second approach in making cable models. For exact scaling all stress quantities should be reduced by a factor of two, including σ_1 and σ_3 from a rock failure envelope, σ_1 and σ_3 in a uniaxial strain test, Young's modulus E, applied vertical and lateral pressures P_V and P_H in the test machine, and borehole/cable interaction pressure σ_{BC}. With the exception of modulus E, all these quantities are scaled reasonably by using the RMG-2A simulant and a cable model with a curve of σ_{PL} versus dimensionless platen displacement x/d reduced in stress by a factor of two. For small closures, as in the hardened structure response, E is an important parameter. However, the code calculations by TRW show that for the large borehole closures for cable crushing, the load versus closure curves become so steep that the critical load to produce a critical crushing closure will not depend strongly on E.

TWR made two sizes of model cable to be tested, one only slightly smaller than the 5/8-inch (159-mm) diameter borehole and the other half this size. The cable outside diameters were 0.50 inch (12.7 mm) and 0.25 inch (6.3 mm), respectively. Cross section photographs of the cables in model boreholes are given in Figure 3.3.

mm 1cm 2 3 4 5 6 7 8 9 10

MP-5762-38

FIGURE 3.3a   LARGE CABLE IN BOREHOLE
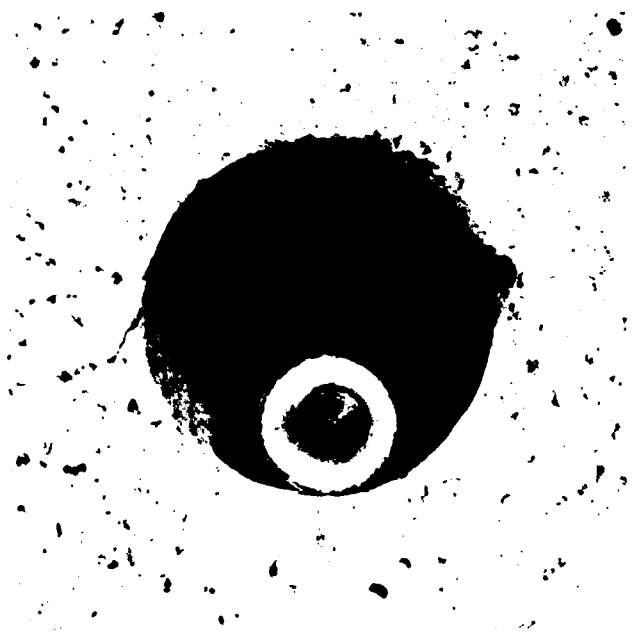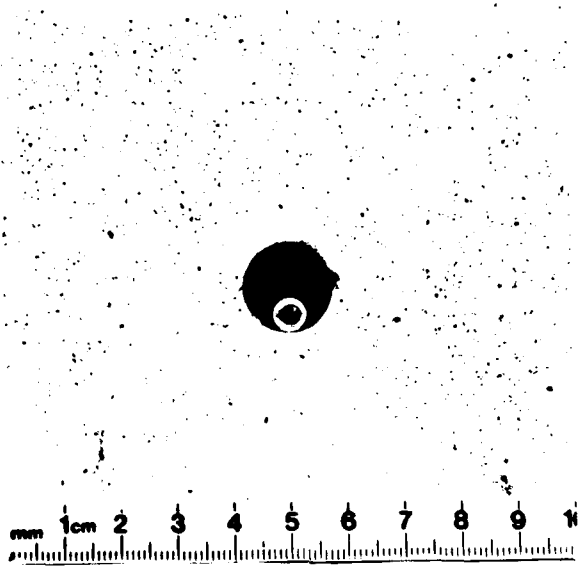
MP-5762-39

FIGURE 3.3b   SMALL CABLE IN BOREHOLE

3.3.4 Instrumentation

Four quantities were measured during both static and dynamic experiments: vertical loading pressure P_V, lateral confining pressure P_H, rock specimen lateral strain ϵ_θ (two redundant gages), and borehole closure u_B. In the static tests, P_V was taken as the independent variable and the other quantities were measured at each small increment in P_V. At each increment, the confining pressure P_H was increased just enough to maintain the uniaxial strain condition, $\epsilon_\theta = 0$, as observed by two strain gages mounted on the copper jacket on the rock. Borehole closure was recorded by photographing the borehole through the access ports in the test machine. Where possible (where there was no cable or springline rubble), we also measured deformation directly with a hole micrometer.

In the dynamic tests, time is the independent parameter. Two separate measurements of both P_V and P_H were recorded continuously on oscilloscopes and magnetic tape: P_V in the gas above the rock and in the oil below the rock, and P_H at two heights in the lateral chamber around the rock. The rock lateral strain was also recorded continuously. We maintained a nearly uniaxial strain condition by adjusting the vertical and lateral explosive charges so that P_V/P_H was equal to values taken from the static uniaxial strain tests. In three tests, P_V/P_H was adjusted to intentionally produce underconfined and overconfined conditions for comparison. The most difficult measurement was dynamic borehole deformation. This was done by high-speed photography of a back-lighted thin plastic tube inside the borehole.

In all tests, both static and dynamic, detailed pre- and posttest measurements were made of the rock specimen and the rock was sectioned after the test to measure and photograph final borehole and cable deformed shapes.

3.4   RESULTS--EMPTY BOREHOLE RESPONSE

A summary of the objectives, measurements and key results of all
the tests, both with and without cables, is given in Table 3.2.   The
table should be scanned to get an overview of the scope and approach of
individual tests before proceeding with the discussion of detailed
results.

3.4.1   Static Tests

The first tests performed were static tests, to observe in detail
the mechanisms of borehole collapse and to obtain the static confining
pressures needed to maintain a uniaxial strain condition.   Figures 3.4
and 3.5 give cross sections of the grout specimens and boreholes in tests
on unlined boreholes in which springline rubble was removed periodically
throughout the tests.   The first test (SUX-105, Figure 3.4) was carried
to complete borehole closure to demonstrate that this could be done in
the machine while maintaining a reasonable uniaxial strain condition and
without losing pressure seals.   The model rock was dry in this test.   In
all other tests the rock was saturated as closely as possible to 100%.
In Figure 3.4, the location of the borehole is shown by a thin horizontal
region of broken rock with fractures from the ends of the region extending
toward the top and bottom of the specimen.   The top and bottom of the rock
are caved in about 0.15 inch (4 mm) as a result of the large deformation
and crushing of the unsaturated rock.

Test SUX-106 (Figure 3.5) was performed in the same way but on
a saturated rock and was stopped short of complete collapse so that the
sectioned rock would show the closing-eye shape of the borehole.   Note
that in the saturated condition the ends of the rock are caved in only
a slightly.   In both tests SUX-105 and SUX-106, the springlines began
flaking off as the crown-invert closure increased.   This rubble was
removed in these tests so that the crown-invert diameter could be measured
and plotted against vertical pressure (Figure 3.6).   The result was the
eye-shaped closure seen in Figure 3.5, in which the crown and invert
became flattened in shape but remained intact.   The top and bottom arcs

51

Table 3.2   EMPTY BOREHOLE AND BOREHO

Test	Date	Objective	Cable	Camera Speed (fps)	Camera Results	Explosive Vert./Hor. (gm)/(gm)	$P_{\perp}$ (ksi)	Ver
							Static Tests	
SUX-105	4-11-77	Static closure of empty borehole, dry rock, springline rubble continuously removed.	None	35 mm	Sequence	Static	--	
SUX-106	4-18-77	Static closure of empty borehole, wet rock, springline rubble continuously removed.	None	None		Static		
SUX-111	11-18-77	Static closure of empty borehole, springline rubble left in hole.	None	Polaroid	Tygon tube buckled	Static		
SUX-112	11-21-77	Static closure around small cable to severe crushing.	Small	None	Static			
SUX-113	12- 1-77	Static closure around large cable to severe crushing.	Large	None	Static			
							Dynamic Tests	
DUX-86	4-20-77	Dynamic closure of empty borehole.	None	10,000	smoke	120/80	--	
DUX-87	4-21-77	Dynamic loading without closure of empty borehole.	None	10,000	good PICS	45/28	4.42	
DUX-88	4-22-77	Dynamic closure of empty borehole, at lower pressure than in 86.	None	10,000	good PICS	70/40	7.36	
DUX-89	4-25-77	Dynamic closure around large cable at threshold pressure that closed empty borehole (that in 88).	Large	None		70/40	7.60	
DUX-90	4-27-77	More severe closure around large cable at higher pressure than in 89.	Large	None		120/80	11.24	
DUX-91	6-17-77	Observe form of empty borehole closure with overconfining lateral pressure.	None	10,000	shot misfire	80/80	shot misf	
DUX-92	6-21-77	Observe form of empty borehole closure with underconfining lateral pressure.	None	10,000	good PICS (some smoke)	80/34	6.92	
DUX-93	6-22-77	Repeat of shot 91 (overconfining lateral pressure).	None	10,000	smoke	80/80	8.00	
DUX-103	11-22-77	Dynamic closure around small cable at threshold pressure that closed empty borehole.	Small	None		70/40	7.18	
DUX-104	11-23-77	Dynamic closure around small cable at higher pressure (same as for large cable in 90).	Small	None		120/80	10.70	

---

*Averages and standard deviations from the 5 measurements with 120/80 gm charges were: $P_V = 11.69 \pm 0.74$ ksi (6.3%), $P_H =$ 8

Averages and standard deviations from the 6 measurements with 70/40 gm charges were: $P_V = 7.64 \pm 0.40$ ksi (5.2%), $P_H =$ 5.5

53   /

| Vertical *P | | | Horizontal *P | | | Rock Strain | | Results |
P_1 (ksi)	P_4 (ksi)	Ave. (ksi)	P_2 (ksi)	P_3 (ksi)	Ave. (ksi)	SG1 (%)	SG2 (%)	
Tests								
--	--	13.6	--	--	6.42	+0.12	-0.12	Borehole crown-invert closure vs. pressure until completely closed.
					6.18	-0.21	+0.21	Poorly controlled lateral pressure. Test stopped short of complete closure.
		9.50			6.14	+0.072	-0.070	Tygon tube buckled, stopping photography. Good record of P_H vs P_V. Hole shaped in figure eight.
		11.50			8.30	-0.14	+0.140	More cable deformation in crown-invert direction then across springlines (opposite from dynamic test)
		11.50			7.88	+0.039	-0.039	Cable deformed only slightly; beginning to push in at one springline.
Tests								
--	11.70	11.70	8.90	8.00	8.45	Off +	·1.0	Rock extruded through tunnel access port
4.42	4.60	4.51	3.47	--	3.47	-0.15	-0.13	No closure, springlines very slightly flaked.
7.36	8.32	7.84	5.60	5.80	5.70	+0.48	+0.35	Borehole completely collapsed; high speed photos show springlines move in first.
7.60	7.80	7.70	5.52	5.72	5.62	+0.13	+0.18	Borehole collapsed onto cable, but cable only slightly deformed into a rounded rectangle.
11.24	12.40	11.82	8.00	8.80	8.40	gages failed		Cable creased at springlines, severely crushed but not shorted.
shot misfire								One machine ring assembled improperly, explosive chambers vented.
6.92	7.99	7.36	5.03	4.90	4.97	+0.35	Off +	Borehole completely collapsed with S-shaped boundary as in 88.
8.00	8.83	8.42	7.87	8.10	7.98	+0.14	-0.18	Same as 92 even though rock was overconfined rather than underconfined.
7.18	7.60	7.39	5.40	4.95	5.18	-0.21	-0.17	No borehole damage whatsoever.
10.70	12.40	11.55	--	8.15	8.15	-0.16	-0.22	Cable severely crushed in from springline sides.

Z), P_H = 8.37 ± 0.44 ksi (5.3%).

P_H = 5.50 ± 0.30 ksi (5.5%).
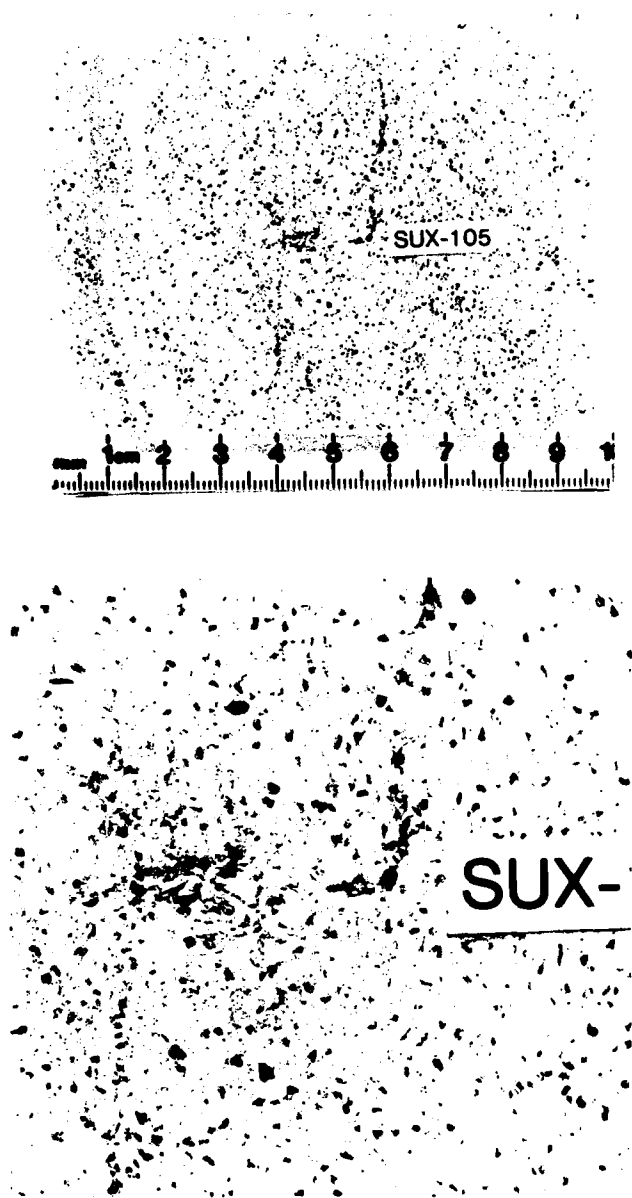
FIGURE 3.4 SECTION VIEWS OF COLLAPSED EMPTY BOREHOLE
IN DRY SRI RMG 2A TUFF SIMULANT

Internal rubble was removed throughout static, uniaxial
strain test; final pressure P_V = 13.6 ksi = 93.8 MPa
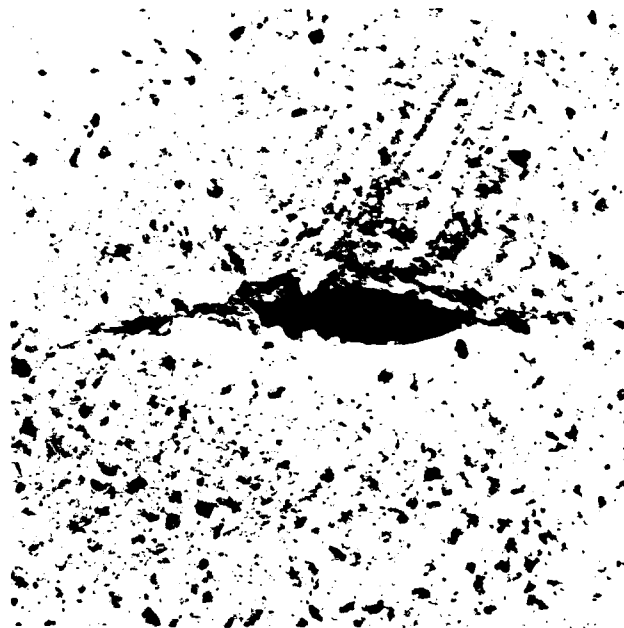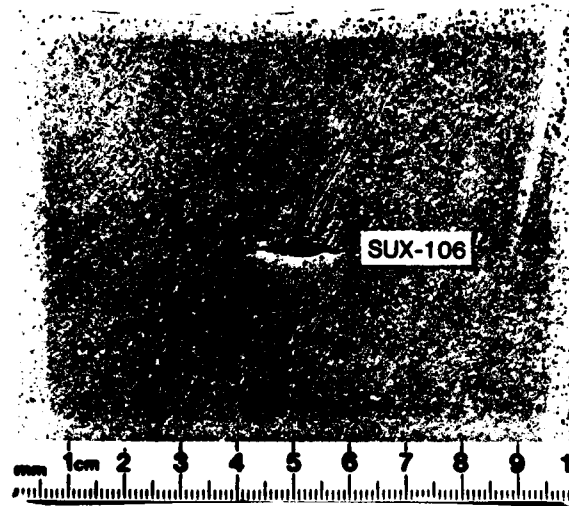
FIGURE 3.5   SECTION VIEWS OF COLLAPSED EMPTY BOREHOLE
IN SATURATED SRI RMG 2A TUFF SIMULANT

Internal rubble was removed throughout static, uniaxial
strain test; final pressure P_V = 11.0 ksi = 75.9 MPa

56
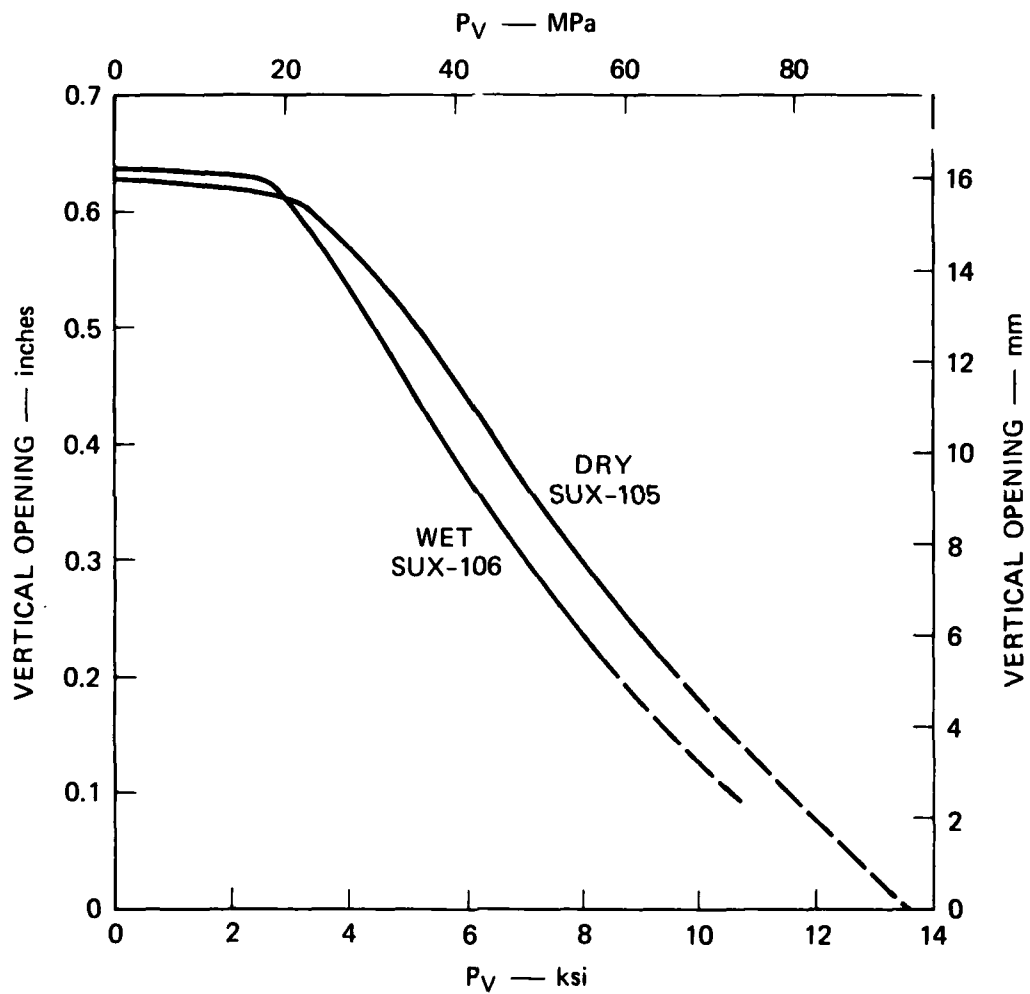
FIGURE 3.6   VERTICAL OPENING VERSUS VERTICAL PRESSURE FOR EMPTY BOREHOLES
IN WET AND DRY SRI RMG 2A SIMULANT UNDER STATIC, UNIAXIAL
STRAIN LOADING

of the crown and invert in Figure 3.5 have a length corresponding to 90 degree ($\pi/2$ rad.) arcs in the undisturbed borehole.

It is interesting to observe in Figure 3.6 that a large increase in vertical pressure is needed from the pressure of about P_V = 3 ksi (21 MPa), at which permanent closure begins, until about P_V = 12 ksi (83 MPa), where closure is complete. During most of this increase the free field stresses are in the yield region of an ideally elastic-plastic analytical model. For this model, NONSAP calculations give unbounded deformation (no equilibrium solution can be obtained) as soon as the free field yield condition is reached. The large increases in applied stresses needed to actually cause closure (Figure 3.6) suggest that new strength mechanisms of rock plastic flow are probably active in this range.

However, for the borehole/cable interaction experiments, which are described in the next subsection, two features of response tend to reduce this gap between simple small-deformation theory and experiment. First, the volume of rubble material removed during tests SUX-105 and SUX-106 was significant and increased the deformation required for closure. Second, for efficient use of the borehole, the volume of the cable is a large fraction of the volume of the borehole. The net result is a much reduced deformation of the type shown in Figures 3.5 and 3.6. For the larger cable, interaction with the borehole begins before the vertical opening has reduced to the 0.5-inch (12.7-mm) diameter of the cable, at a pressure of P_V = 4.4 ksi (30 MPa). Because of the springline rubble, interaction begins sooner. Experiments described in the next subsection show that even for the smaller cable, significant interaction and cable deformation occur at P_V = 8 ksi (28 MPa).

To see the effect of springline rubble on borehole closure, we performed experiment SUX-111 in which the rubble was held within the borehole by a tube of polyethelene rubber with a solid but weak rigid styrofoam cylinder inside it. The polyethylene conducts light and was backlighted and used in an attempt to obtain static closure photographs comparable to those described in the next subsection for the dynamic tests.

58

Unfortunately, the illuminated end of the tube buckled as the borehole closed so that no useful photgraphs were obtained. This difficulty can probably be overcome, but we were unable to perform repeat tests because of limited time and funds. Also, because excellent photography was obtained in the dynamic tests, the added expense did not seem warranted.

The important result of SUX-111 is shown in the section photographs in Figure 3.7. Note that the crown and invert have moved together as in SUX-105, but that the dominant inward motion is at the springlines, where the rubble has squirted in and deformed the polyethylene tube into a figure-8 shape. The solid material inside the tube is the styrofoam.

Figure 3.8 gives the horizontal confining pressure P_H required to maintain a nearly uniaxial strain condition plotted against vertical loading pressure P_V. Plots are given for tests SUX-112 and SUX-113, with model cables present, in addition to test SUX-111. Data from all three tests fall close to a single curve. One might expect that the curve from SUX-113 would differ from the others because this test was performed with a large cable, whereas SUX-112 was performed with a small cable and SUX-111 was performed with the polyethylene tube, both of which had considerably smaller volumes than the large cable. However, the data points from SUX-111 and SUX-113 fall very close together; the largest difference is between these points and those for SUX-112, and even this difference is quite small.

The straight lines drawn through the elastic and plastic portions of the data points have slopes that give Poisson's ratio $\nu = 0.20$ in the elastic region and friction angle $\phi = 4.3$ degrees in the plastic region. The intercept of the plastic line with the P_V axis is at 2 ksi (14 MPa) which is slightly larger than the unconfined strength $\sigma_u = 1.5$ ksi (10 MPa) found from uniaxial compression tests.

An example plot of rock lateral strain versus applied vertical pressure in these tests is given in Figure 3.9. Throughout the tests, strain is measured by two gages on the copper can containing the rock specimen. The gages are located on opposite sides of the rock at the ends of a diametral line perpendicular to the borehole and at an axial

59

SUX-111

mm 1cm 2 3 4 5 6 7 8 9 1(
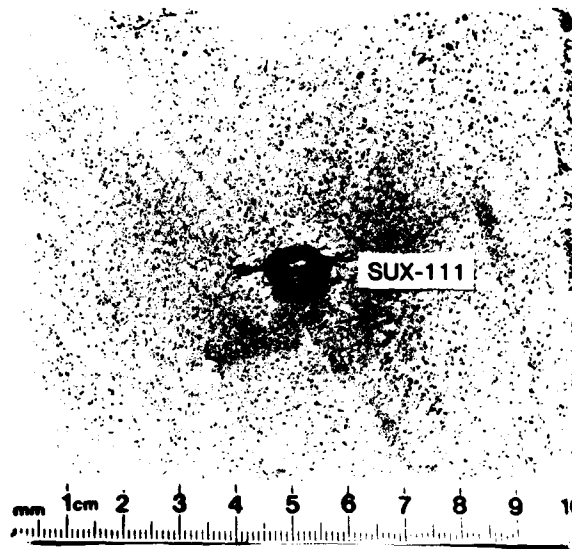
MP-5762-43

FIGURE 3.7 SECTION VIEWS OF BOREHOLE COLLAPSED AROUND
SOFT POLYETHYLENE PHOTOGRAPHIC TUBE

Note that springline rubble, not removed during test, has
pushed in from sides and deformed tube into figure-8
shape; final pressure P_V = 9.50 ksi = 65.5 MPa

60
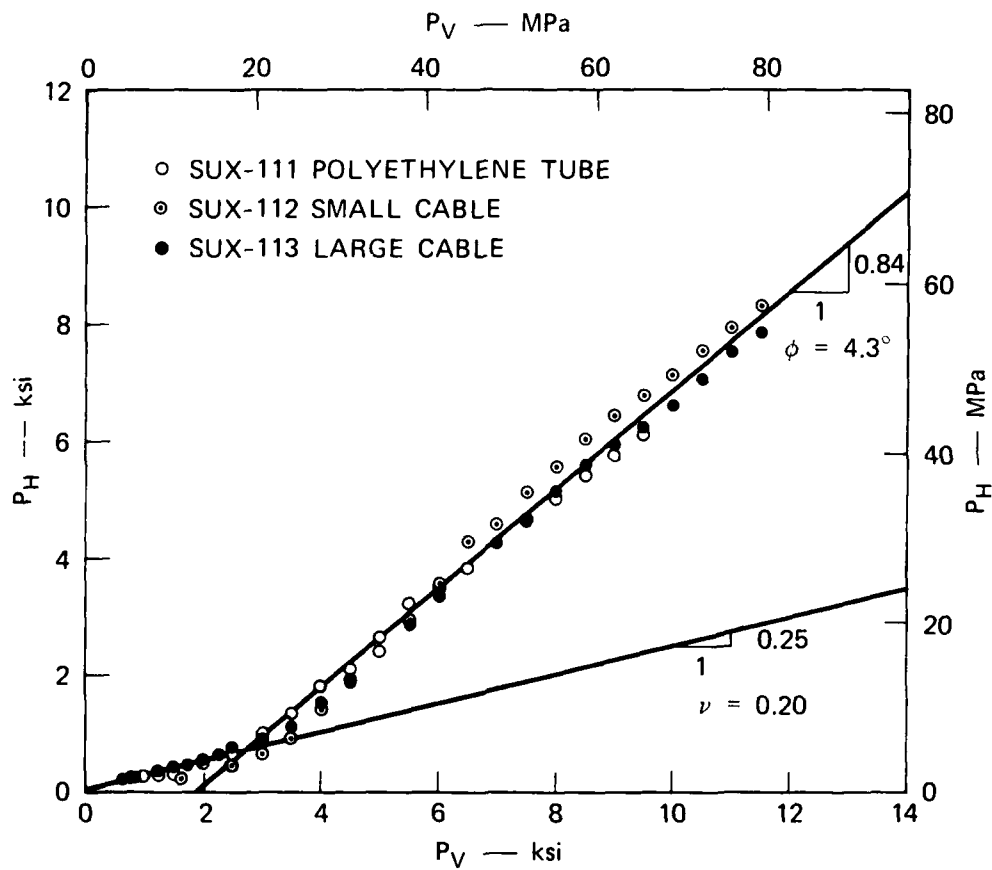
FIGURE 3.8   CONFINING PRESSURE P_H VERSUS LOADING PRESSURE P_V DURING STATIC
UNIAXIAL STRAIN TESTS ON SRI RMG 2A TUFF SIMULANT
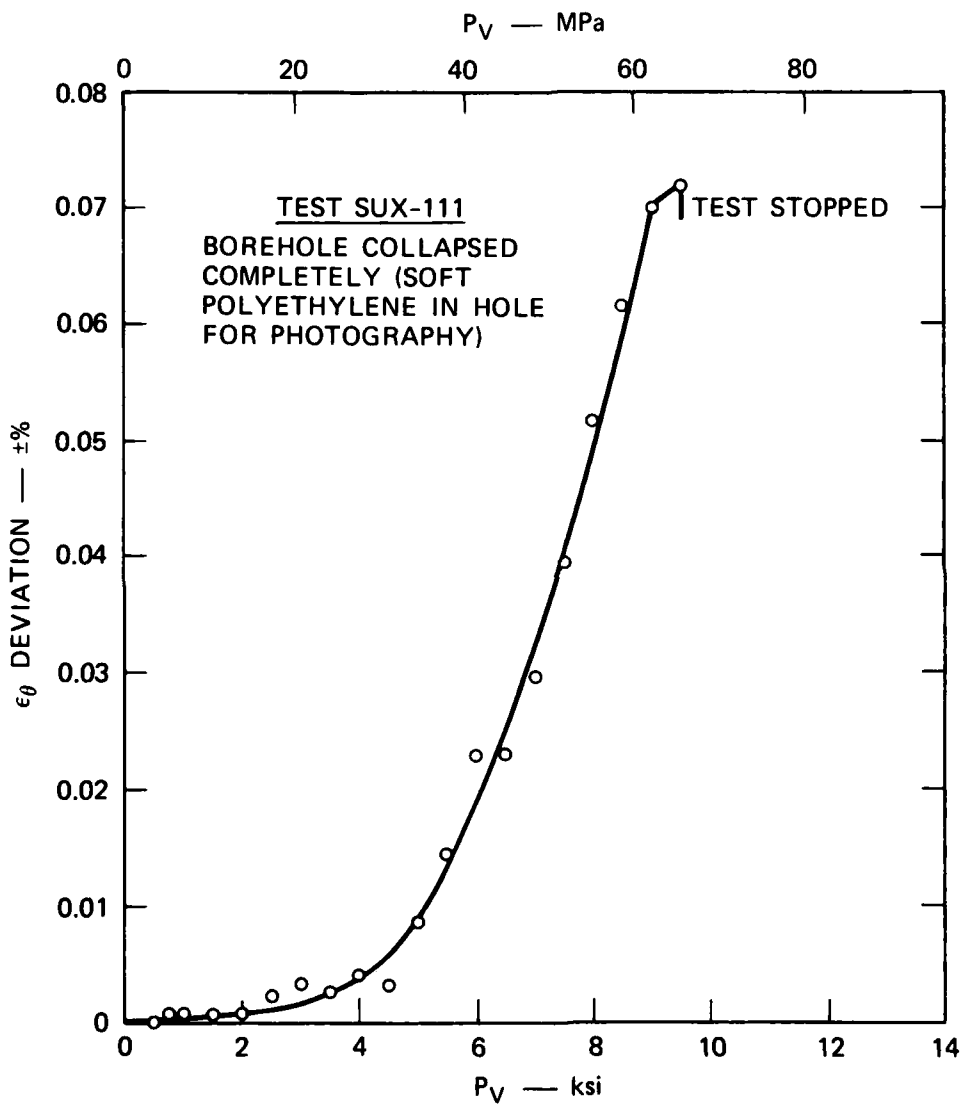
MA-5762-45

FIGURE 3.9   ROCK SPECIMEN LATERAL STRAIN DURING COMPLETE
COLLAPSE OF UNCONFINED BOREHOLE

Values are maximum of two gages slaved by P_H to be nominally
equal and opposite in sign.

position one borehole diameter above the borehole axis. At each small increment in P_V, P_H is adjusted so that these strain gages read nearly equal and opposite values; that is, so that the average strain is close to zero. The points in Figure 3.9 are at the absolute values of the larger of the two strains, whichever it happened to be, at each P_V. They give a measure of the nonuniformity in the lateral rock boundary strain. The strains are very small when the rock response is mainly elastic and the borehole closure is small. For $P_V = 4$ ksi (28 MPa), $\varepsilon_\theta = 0.005\%$. Then the strain rises rapidly during rock plastic flow and borehole closure until, at the end of the test, $P_V = 9.5$ ksi (65.5 MPa) and $\varepsilon_\theta = 0.072\%$. This is still a very small strain compared with the large vertical deformation of the rock and the gross borehole closure.[*] Peak strains at the maximum loads in all of the tests, both static and dynamic, are listed in Table 3.2.

3.4.2 Dynamic Tests

Five dynamic tests were performed on nominally empty boreholes. The boreholes were not completely empty because, as in static test SUX-111, light-transmitting polyethylene tubes were inserted in order to photograph the boreholes as they closed. In the first test, DUX-86, the peak vertical pressure, $P_V = 11.7$ ksi (80.7 MPa), was selected to be near the maximum stresses in the static tests just discussed. Borehole closure was so severe that the collapsed rock around the borehole squirted out of the tunnel acces ports of the machine. In the next test, DUX-87, the peak pressure was reduced to $P_V = 4.5$ ksi (31 MPa). At this pressure there was no borehole closure. The only damage appeared to be some very minor roughness along the springlines.

DUX-88 was performed at an intermediate pressure of $P_V = 7.5$ ksi (52 MPa) with $P_H = 5.70$ ksi (39.3 MPa). This loading produced closure similar to that in static test SUX-111 (which in sequence was performed

---

[*] In tests of reinforced tunnels for deep-based structures, as reported in Chapter 2, the maximum rock lateral strain is only about 0.005 to 0.020%.

after DUX-88). As in test DUX-87, the high-speed photographs turned
out well but now showed substantial deformation. Selected frames are
given in Figure 3.10. The closure is seen to be dominated by the inward
movement of the springline rubble (at the sides of the hole in the photo-
graphs). Also, by comparing the pressures given in the caption with the
closure sequence in the photographs, we see that the closure follows the
pressure in a pseudo-static manner, as expected for loading times that
are long compared with the wave transit time through the rock specimen.
The complete pressure-time histories and a cross plot of horizontal versus
vertical pressure are given in Figure 3.11. At t = 3.2 msec, P_V = 4.8
ksi (33 MPa) and noticeable closure is just starting, consistent with
the static curve in Figure 3.6. At t = 4.0 msec, P_V = 6.4 ksi (44 MPa)
and closure is well under way, again consistent with Figure 3.6. At t =
4.5 msec, smoke has obscured the picture, but it is evident by comparing
the photographs for t = 4.0 msec and 4.2 msec that by 4.5 msec the bore-
hole is well-closed around the polyethylene tube. The peak pressure,
P_V = 7.5 ksi (52 MPa), occurred at 6 msec. The section photographs in
Figure 3.12 show that the polyethylene tube deformed into a distorted
S shape, with the crown and invert each intact over a short segment and
the springlines pushed in until the tube was completely closed.

In this test, the rock lateral strain records indicated that
near the peak stress the rock was underconfined; by the time of complete
closure the lateral strain gages read 0.48 and 0.34% outward as listed
in Table 3.2. To see whether confinedment has a serious effect on bore-
hole closure mechanisms, we performed further experiments with the
lateral pressure increased above that required for uniaxial strain. The
first test, DUX-91, failed because one of the test machine rings was
accidentally assembled upside down. The repeat test, DUX-93, went well,
giving peak pressures P_V = 8.4 ksi and P_H = 8.0 ksi (59 and 55 MPa),
compared with P_V = 7.5 ksi and P_H = 5.7 ksi (52 and 39 MPa) in test
DUX-88.

t_0	+ 0.8 msec	+ 1.2 msec
+ 1.6 msec	+ 2.0 msec	+ 2.4 msec
+ 2.8 msec	+ 3.2 msec	+ 3.6 msec
+ 4.0 msec	+ 4.2 msec	+ 4.5 msec

MP-5762-8R
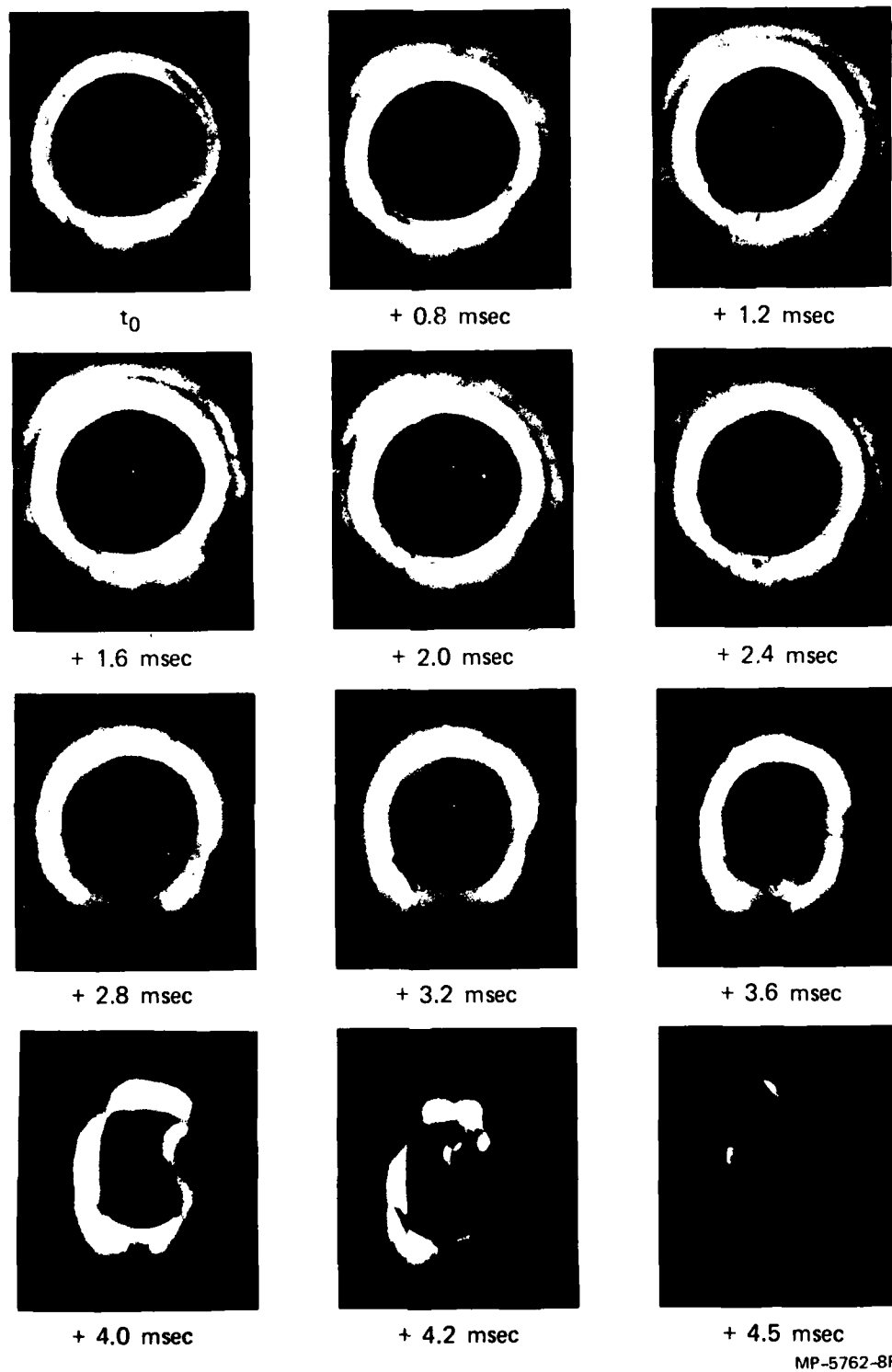
FIGURE 3.10   DYNAMIC CLOSURE OF EMPTY BOREHOLE IN SRI RMG 2A

Test DUX-88, peak pressures P_V = 7.5 ksi, P_H = 5.7 ksi (52 and 39 MPa) occurred at 5 msec; at 3.2 msec, P_V = 4.8 ksi = 33 MPa; at 4.0 msec, P_V = 6.4 ksi = 44 MPa.
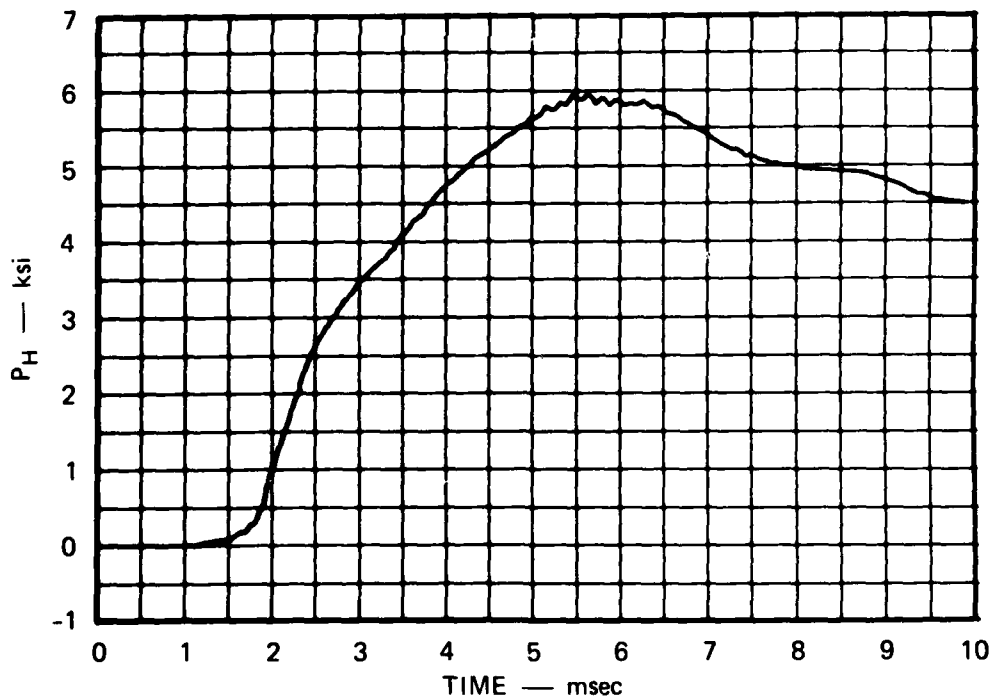
FIGURE 3.11   PRESSURE-TIME HISTORIES AND CROSS PLOT FOR VERTICAL AND
HORIZONTAL PRESSURES IN TEST DUX-88

66
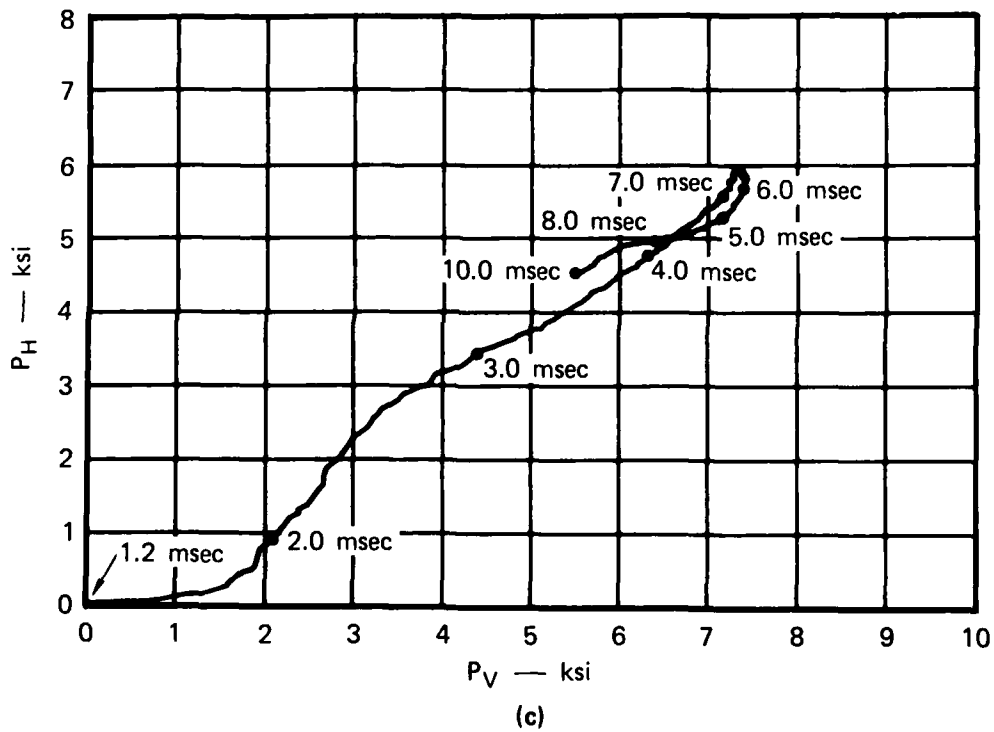
FIGURE 3.11   PRESSURE-TIME HISTORIES AND CROSS PLOT FOR VERTICAL AND
HORIZONTAL PRESSURES IN TEST DUX-88 (CONCLUDED)
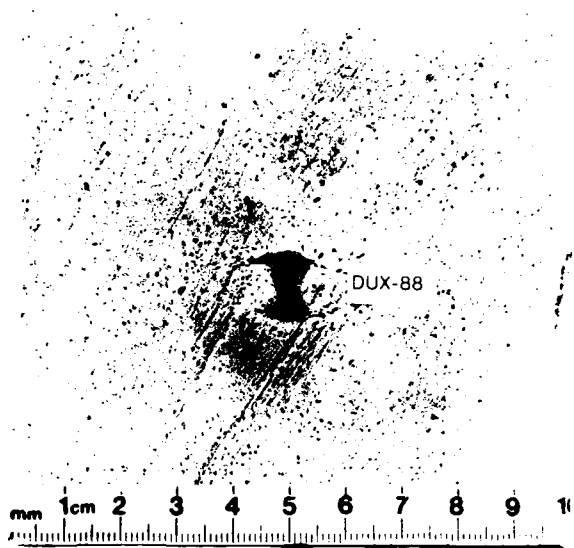
FIGURE 3.12   POSTTEST SECTION PHOTOGRAPHS OF
COLLAPSED BOREHOLE, TEST DUX-88

Pressure and strain records from DUX-93 are given in Figure 3.13. The record from strain gage 1 is similar in form to those in DUX-88, starting off initially with a negative swing of strain and then becoming positive later. However, the strain is much smaller than in DUX-88. The positive strain near t = 5 ms, where the pressures are maximum and tunnel closure occurs, is 0.14% in DUX-93 compared with 0.48% in DUX-88. The record from strain gage 2 starts off similarly to that from gage 1 but remains negative. Near t = 5 msec, the strain is -0.18%. These strains are small and nearly equal and opposite in sign, just as in the static tests. In total, the test appears to have been slightly over-confined, as desired.

Rock and borehole cross sections for this test and also for test DUX-92 are given in Fiure 3.14. Test DUX-92 was performed in an inten-tionally underconfined condition, with peak pressures P_V = 7.36 ksi and P_H = 4.97 ksi (5. and 34 MPa). In this test, the peak strain from gage 1 was +0.35% and the record from gage 2 went off scale beyond +0.5%. It is apparent from the shape of the rock in Figure 3.14 that it was under-confined. Yet, the deformed shape of the polyethylene liners in the underconfined and overconfined tests is essentially identical. In both tests, the crown and invert arcs have moved in a moderate amount and the springline rubble has moved in forcefully to produce an overall S shape in the squeezed-off tube. Close-up views of the deformed boreholes are given in Figure 3.15.

Figure 3.16 gives a sequence of high-speed photographs, from test DUX-92. The dominance of springline rubble in producing closure is apparent.

3.5   RESULTS--BOREHOLE/CABLE INTERACTION

All the tests described in this section were begun with the cable resting on the bottom side of the borehole in the testing machine. For static tests this was on a springline, because the machine and rock axis was horizontal, and for dynamic tests this was on the invert, be-cause the machine and rock axis was vertical (as it is in all the
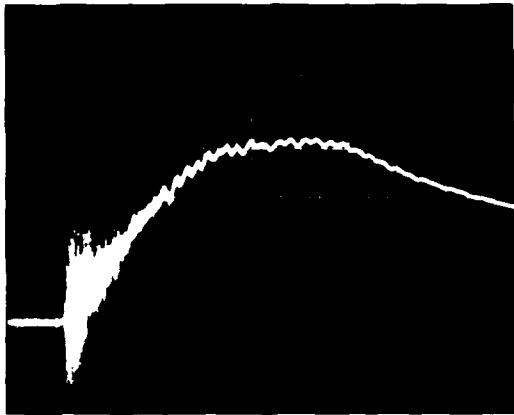
(a) $P_1 = P_V$ (2 ksi/cm)
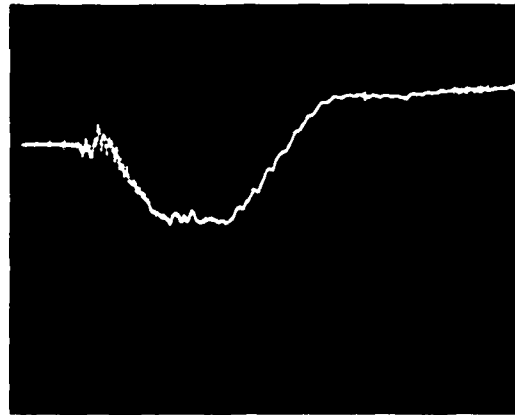
(c) S.G. 1 (0.125%/cm)
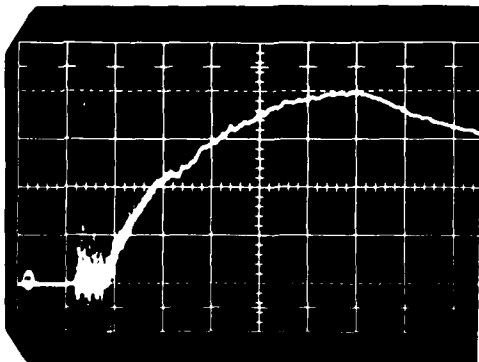
(b) $P_3 = P_H$ (2 ksi/cm)
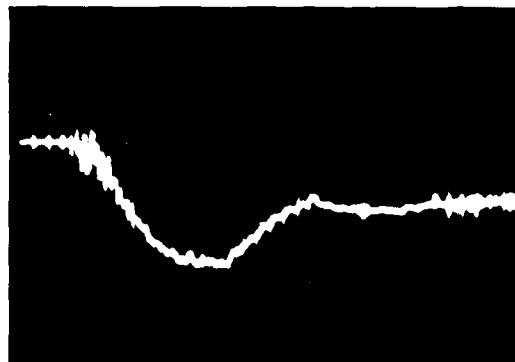
(d) S.G. 2 (0.125%/cm)

MP-5762-47

FIGURE 3.13   PRESSURE AND ROCK LATERAL STRAIN HISTORIES FOR TEST DUX-93
Time scale is 1 msec/cm for all records
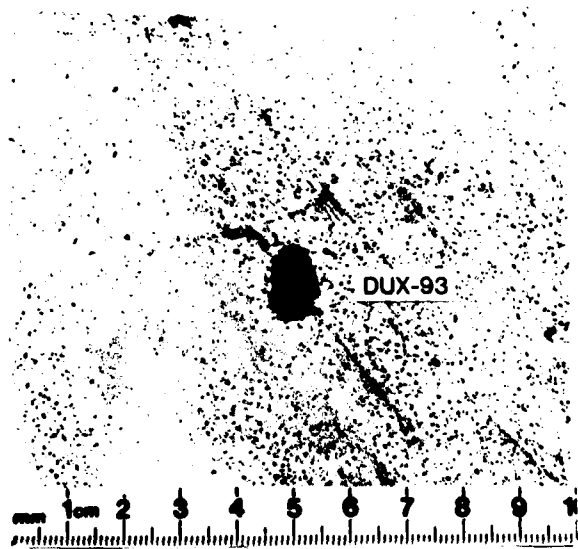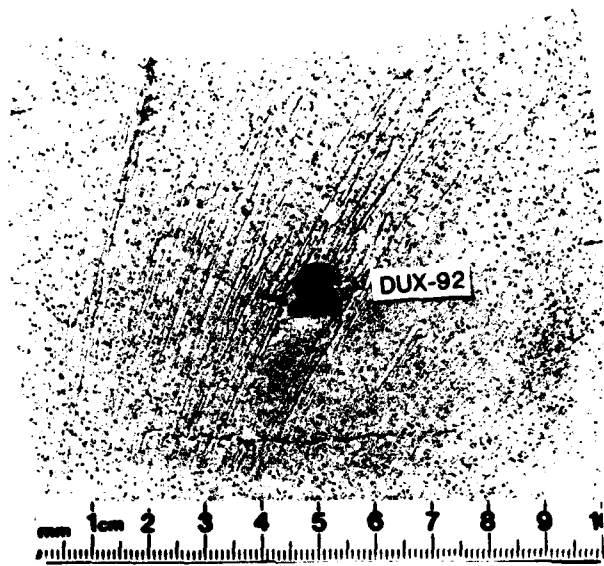
MP-5762-48

FIGURE 3.14   COMPARISON OF ROCK SPECIMEN EXTERNAL
PROFILES FOR UNDERCONFINED (DUX-92)
AND OVERCONFINED (DUX-93) DYNAMIC
LOADING

71
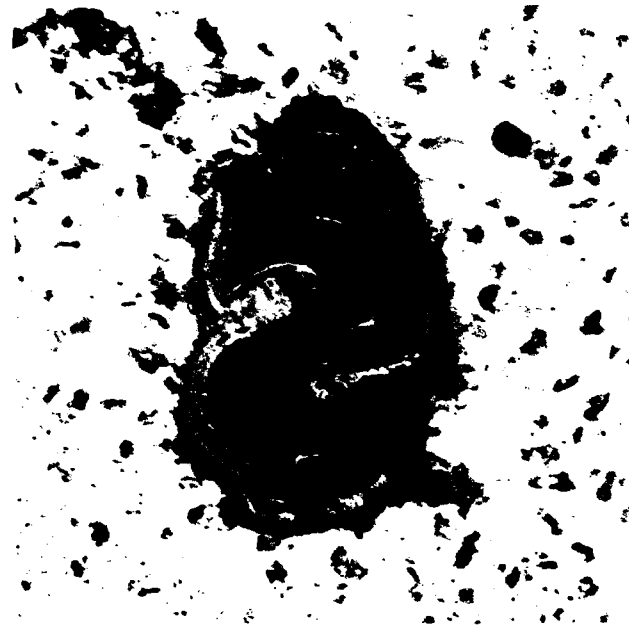
MP-5762-49

FIGURE 3.15   SIMILARITY OF BOREHOLE COLLAPSE SHAPE
FOR UNDERCONFINED (DUX-92) AND OVER-
CONFINED (DUX-93) DYNAMIC LOADING
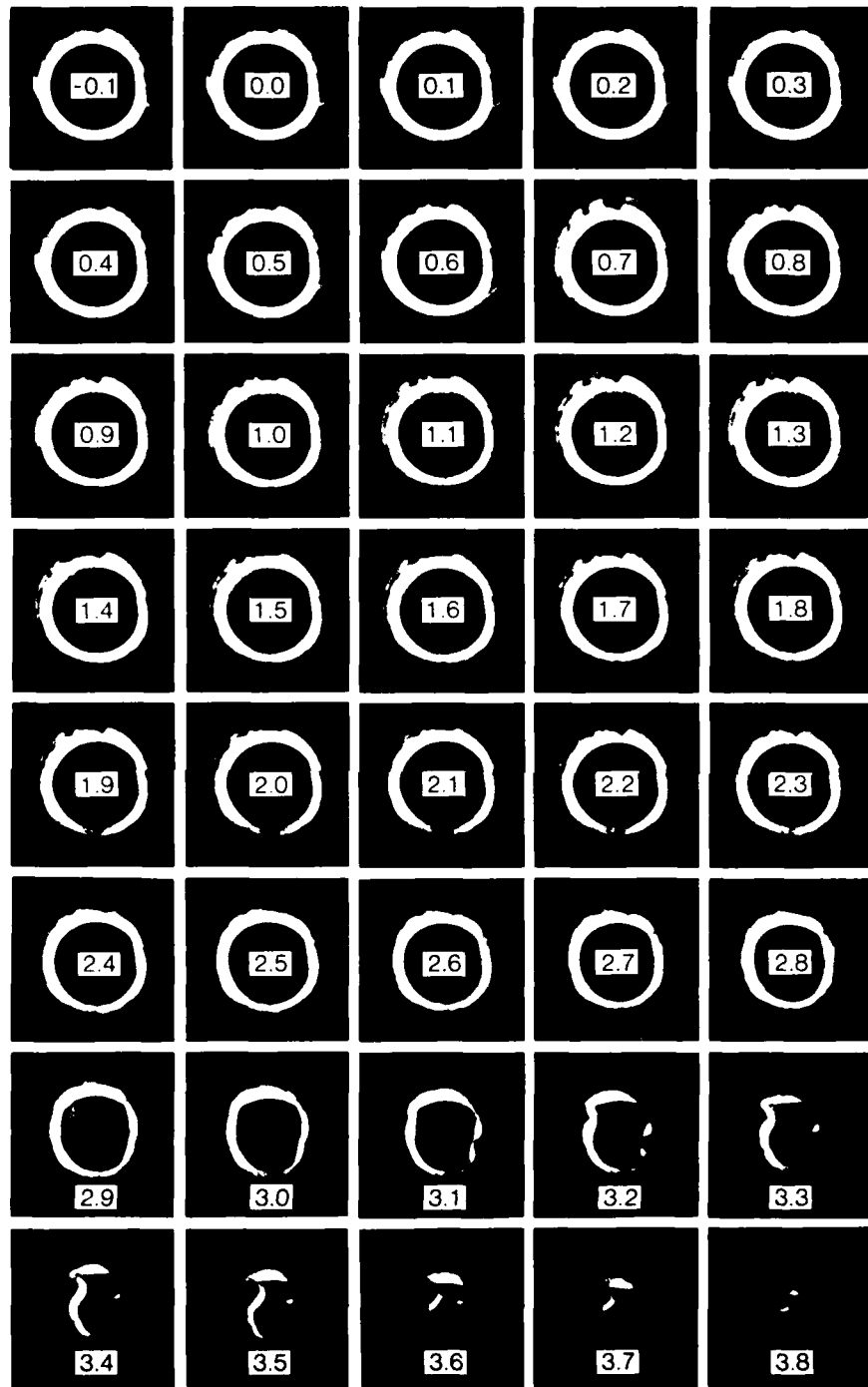
MA-5762-58

FIGURE 3.16 DYNAMIC CLOSURE OF EMPTY BOREHOLE IN SRI RMG 2A

Test DUX-92 peak pressures P_V = 7.4 ksi = 51 MPa and P_H = 5.0 ksi = 34 MPa; numbers in photographs are time from detonation, msec.

photographs of sectioned rock in this report, from both static and dynamic tests). With no special centering devices for an actual cable, resting on one side of the borehole is a probable position. It is difficult to estimate the location of the contact point with respect to the loading direction, so we merely chose the most convenient orientation in our initial tests. Since we saw no noticeable effect of the cable position on borehole/cable interaction, these orientations were maintained throughout the tests.

In all tests, both static and dynamic, continuity of the cable as a D. C. conductor was monitored throughout the test. In no test was the continuity interrupted. As described below, cable deformations were sometimes quite severe but electrical shorting never occurred.

3.5.1 Static Tests

Static tests were performed on both a large and a small cable to a final pressure of P_V = 11.5 ksi (79 MPa). Sectioned rocks and cables from these tests are shown in Figures 3.17 and 3.18. The large cable is only slightly deformed and would have almost its full communication capacity. The small cable, however, is bent from the sides so that its performance would be degraded. The greater damage in the smaller cable is attributed to the borehole closure being larger so that the inherent asymmetries of the closure processes, as described in the preceding paragraphs, have an opportunity to develop and produce asymmetric response in the cable. The large cable has a high enough hydrostatic strength that, after the small borehole closure to close the gap between borehole and cable occurs, the cable maintains the borehole open in nearly a circular shape.

74
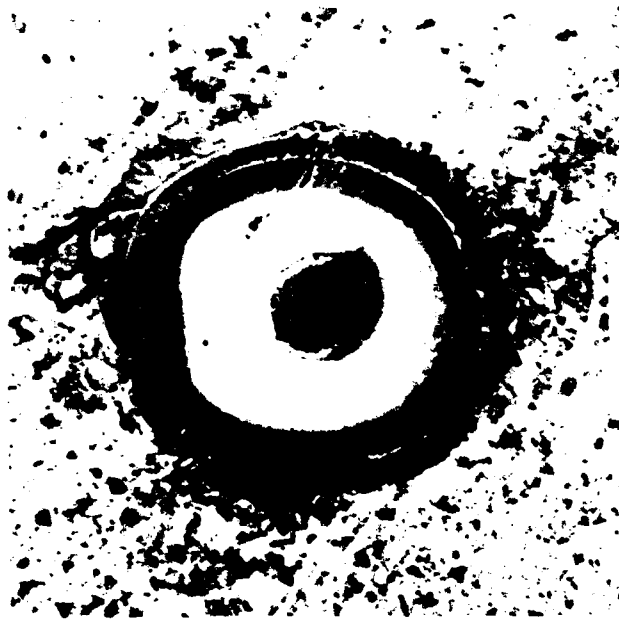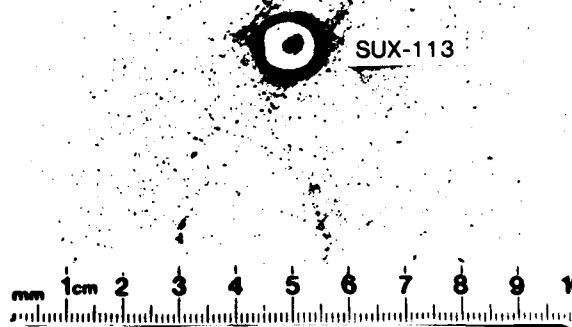
FIGURE 3.17   SECTION VIEWS OF BOREHOLE COLLAPSED
AROUND LARGE CABLE DURING STATIC
UNIAXIAL STRAIN TEST TO P_V = 11.5 ksi
(79.4 MPa) AND P_H = 7.88 ksi (54.4 MPa)

75
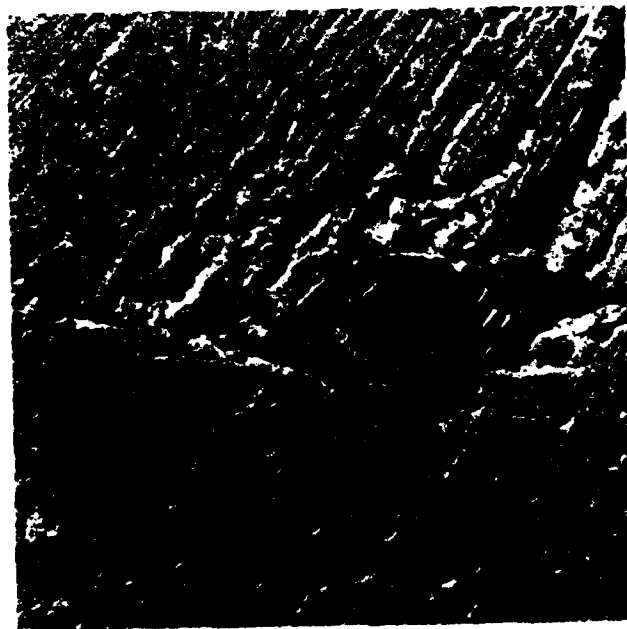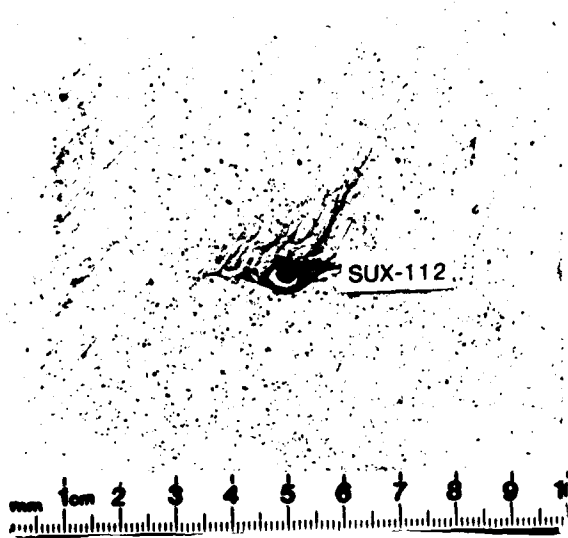
MP-5762-51

FIGURE 3.18   SECTION VIEWS OF BOREHOLE COLLAPSED
AROUND SMALL CABLE DURING STATIC
UNIAXIAL STRAIN TEST TO P_V = 11.5 ksi
(79.4 MPa) AND P_H = 8.30 ksi (57.3 MPa)

However, the dynamic tests described in the next subsection show
that neither of the modes of deformation in these static tests is likely
to occur under dynamic loading in the field. Under dynamic loading,
there is no time for the springline rubble to rearrange and thereby
minimize borehole/cable interaction as it did in these static tests.
The result is more severe deformation into more complex shapes.

3.5.2 Dynamic Tests

Four dynamic tests were performed to bracket threshold and
serious damage for each of the two cable sizes. Figure 3.19 shows
threshold damage in the large cable from loading pressures P_V = 7.8 ksi
and P_H = 5.7 ksi (54 and 39 MPa). The damage is similar to that in the
static result shown in Fgiure 3.17. The outer case of the cable is
deformed into a rounded rectangular shape, with the springline rubble
having moved in a slightly greater distance than the crown-invert dis-
placement.

Figure 3.20 gives section photographs of a large cable and rock
tested at higher pressures P_V = 11.8 ksi and P_H = 8.4 ksi (81 and 58
MPa). This is the pressure level that squirted the unlined borehole
rock out through the testing machine tunnel access ports. With the
cable in place, the rock stayed together but was severely weakened so
that it split in two, either during the test or on removal from the
machine. The cable is seriously deformed both in size and shape. The
crown-invert diameter has been reduced from 12.7 mm to 10.5 mm (a 17%
change), and the springline diameter has been pushed in to 9.0 mm (a
29% change). More important, the squirting action of the springline
rubble has deformed the cable case into an hourglass shape with sharp
inward and outward bends. Figure 3.21 gives a photograph of the entire
model cable before it was sectioned. The deformed shape is uniform
along the length of the tested section, demonstrating the uniformity of
the rock flow in the test. The ends are undeformed because they pro-
trude out through the end fittings to the tunnel access ports.
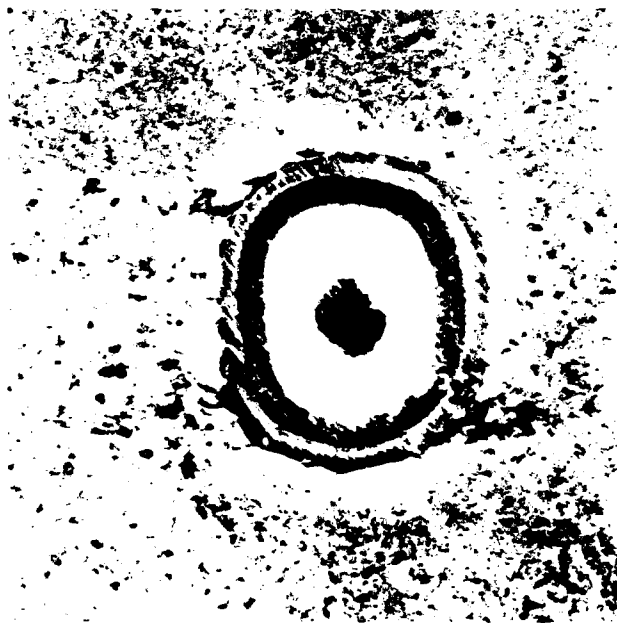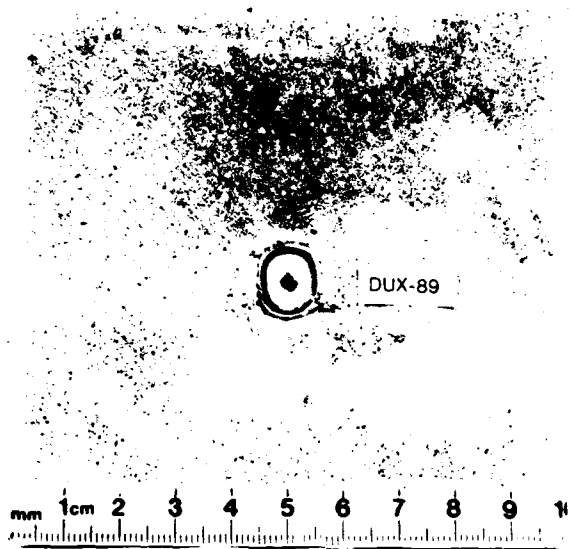
MA-5762-52

FIGURE 3.19   SECTION VIEWS OF BOREHOLE AND LARGE CABLE
DEFORMATION IN DYNAMIC UNIAXIAL STRAIN TEST

Note that springline rubble, on each side, has caused more
cable deformation than crown-invert displacement from top
to bottom; peak pressures were P_V = 7.8 ksi = 54 MPa and
P_H = 5.7 ksi = 39 MPa

78
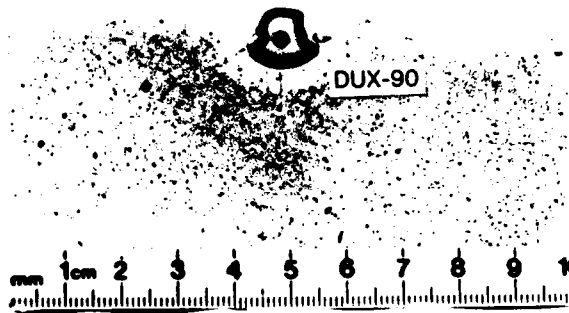
MA-5762-53

FIGURE 3.20   SECTION VIEWS OF SEVERE BOREHOLE AND LARGE
CABLE DEFORMATION IN DYNAMIC UNIAXIAL STRAIN
TEST

Springline rubble has now caused pronounced creases in
cable casing. Rock specimen broke in two while removing
it from testing machine. Peak pressures were P_V = 11.8
ksi = 81 MPa and P_H = 8.4 ksi = 58 MPa.

79
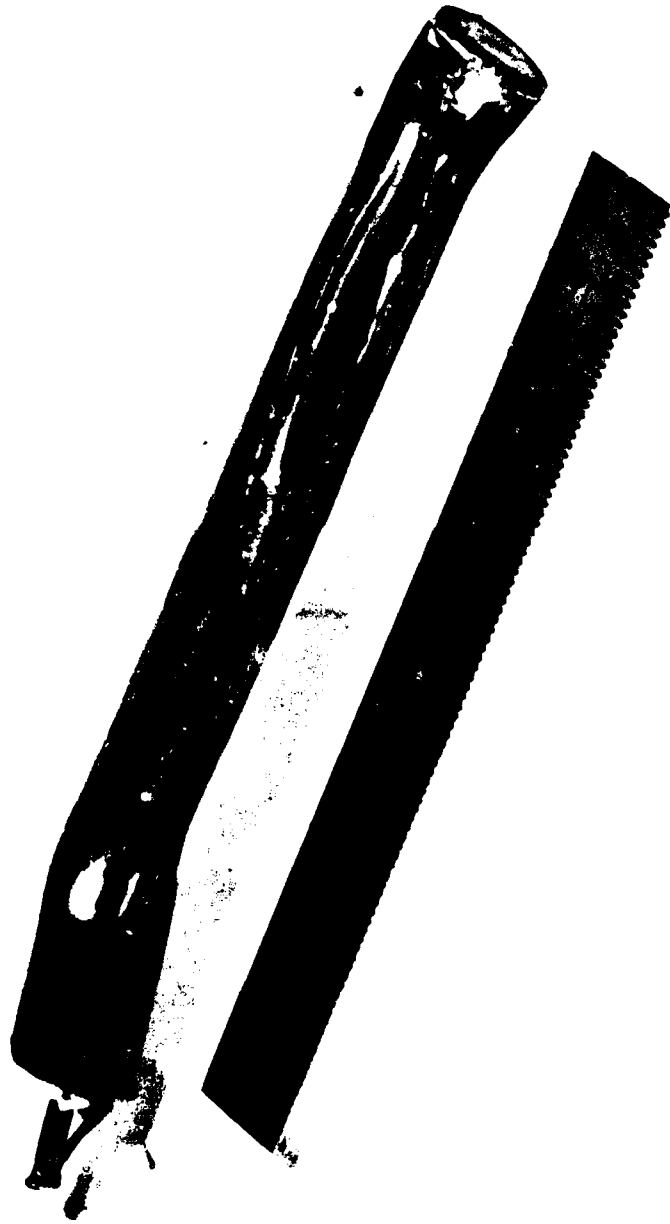
MP-5762-12

FIGURE 3.21   EXTERIOR VIEW OF DEFORMED LARGE CABLE FROM DYNAMIC TEST DUX-90 PRIOR TO SECTIONING

Test DUX-103 was performed with a small cable at pressures P_V = 7.4 ksi and P_H = 5.2 ksi (51 and 36 MPa). The borehole was un-damaged. No explanation has been found for this surprising result, which differs from those of other tests at this level in which severe borehole collapse occurred (see tests DUX-88, 89, and 93 in Table 3.2).

Test DUX-104 was performed with a small cable at pressures P_V = 11.5 ksi and P_H = 8.2 ksi (79 and 56 MPa), essentially the same pressures* used in the corresponding large cable test reported in Figure 3.20. The sectioned rock and deformed cable are shown in Figure 3.22. As in the static test at this level, the cable is considerably flattened. However, unlike the static test, the flattening has taken place across the springline diameter, not the crown-invert diameter. This is attri-buted to the springline rubble in the static test accumulating in a heap around the cable as it falls by gravity from the upper springline and is pushed up underneath the cable from the lower springline. (Recall that the springlines are at the top and bottom of the machine as des-cribed at the beginning of Section 3.5. The important point, however, is that in the static tests the rubble has ample time to be transported around the cable and fill the borehole-cable void uniformly). In the dynamic tests, the rubble has little time to fall or to be transported around the cable. The free-fall distance during the 1-millisecond borehole closure time (Figure 3.16) is only 0.0002 inch (0.005 mm). Thus, the dynamic test gives a much more accurate picture of borehole-cable interaction to be expected in the field. Also, note that although the cable deformation is quite complex, it is symmetric about the horizontal, so we conclude that the initial position of the cable at the bottom of the borehole had a negligible affect on borehole/cable interaction.

---

*The small variations in pressure measurements with gage pairs on in-dividual tests is the same as those from shot-to-shot at the same explosive weights. The standard deviation of all measurements at the charge weight is 6% (see Table 3.2).

DUX-104
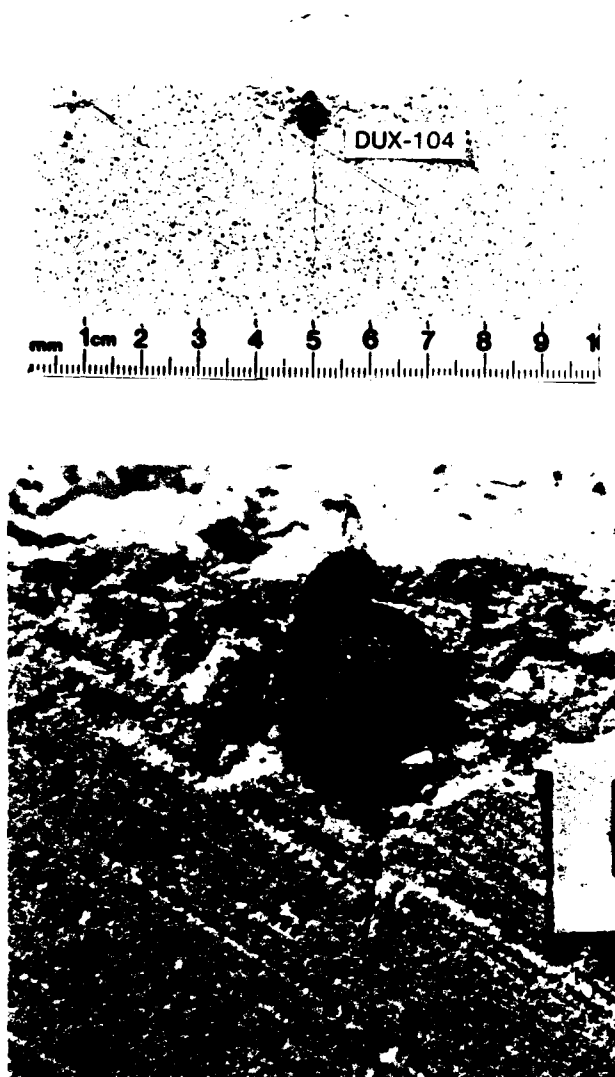
MA-5762-54

FIGURE 3.22   SECTION VIEWS OF SEVERE BOREHOLE AND SMALL
CABLE DEFORMATION IN DYNAMIC UNIAXIAL STRAIN
TEST

Note that as in tests DUX-89 and DUX-90 on large cable,
the more severe inward deformation is from the springline
rubble. Peak pressures were P_V = 11.5 ksi = 79 MPa,
P_H = 8.2 ksi = 56 MPa

82

In addition to being flattened in the springline direction, the outer case of the cable is crimped both top and bottom into tight folds. These large deformations into a complex shape would probably have a serious effect on information transmission through the cable. Nevertheless, no shorting occurred. It appears that, with uniform uniaxial loading along the length of the cable, extremely high pressures would be required to cause a short. With variations along the length because of inevitable variations in rock properties and rock jointing, shorting will be more likely to occur.

3.6   CONCLUSIONS AND RECOMMENDATIONS

From these results, we conclude and recommend the following:

- When the springline rubble is removed as the loading is increased and the borehole closes (an artifice, which was done only in the static tests to observe behavior in the remaining intact rock), closure is dominated by the crown and invert moving toward one another, forming a closing-eye shape.

- However, when the springline rubble is allowed to remain in the borehole, as it will in the field, borehole closure is dominated by springline rubble moving inward.

- In static tests, the springline rubble migrated around the cable, tending to fill the borehole/cable gap uniformly and unrealistically and biasing the borehole/cable interaction toward a uniform pressure around the cable.

- Dynamic testing was therefore crucial in studying borehole/cable interaction.

- In the dynamic tests, loading on the cable from the springline rubble was concentrated to such an extent that in both the small and large cables the sides of the cables were pushed inward and severe crimping occurred in the outer case of the cable.

- Dynamic tests with exaggerated overconfined and underconfined loading conditions (as compared with the basic side-on uniaxial strain loading used throughout the program) showed that this mode of damage from springline rubble is insensitive to lateral confinement. It appears that any slight asymmetry in loading is enough to trigger asymmetric closure and therefore concentrated fracture and rubble at the springlines (i.e., at locations on a diameter perpendicular to the direction of maximum loading).

- High-speed photographs of borehole closure around a backlighted polyethylene tube showed the closure process in detail. Comparison of the closure sequence with simultaneous recordings of loading pressure-time histories showed a frame-by-frame correlation of closure with pressure that was similar to that found in the static tests. Thus, although it was crucial that the tests be performed dynamically in order to have proper rubble motion, the response sequence was dominated by the remaining intact rock, which responded pseudo-statically because the millisecond loading times were long compared with the wave transit time across the rock specimen. This same situation is expected in the DIABLO HAWK field test. In the laboratory, rise times from zero pressure to the peak were about 4 to 5 msec. Borehole closure from negligible deformation to collapse around a polyethylene tube occurred in about 1 msec, in a small pressure increment near the peak of the pressure pulse.

- Borehole/cable interaction was found to be dominated by localized loading on the cable from springline rubble. Thus, the TRW platen test, which simulates the closing-eye mode of closure with springline rubble removed, needs to be reevaluated.

- Similarly, the TRW borehole/cable interaction analysis based on the closing-eye borehole collapse mode should be revised to place emphasis on loading from the springline rubble.

- Critical loads for borehole and cable damage in the SRI RMG 2A tuff simulant were found as follows:

Static Tests (with empty borehole and springline rubble removed)

$P_V \approx$ 3 ksi (21 MPa) - first permanent deformation

$P_V \approx$ 12 ksi (83 MPa) - complete closure

Dynamic Tests

P_V = 4.5 ksi (31 MPa) - no borehole damage

P_V = 7.6 ksi (52 MPa) - borehole completely closed around soft poly-ethylene tube

P_V = 7.6 ksi (52 MPa) - little or no deformation in large and small cables

P_V = 11.7 ksi (81 MPa) - serious deformation in both large and small cables, with severe inward bending and creasing of outer case caused by springline rubble moving inward.

- In spite of the severe bending and creasing in the outer case of the cable, electrical shorting never occurred in any of the tests.

- Shorting is more likely to occur (and has been repeatedly observed in underground tests) from shear motion across the axis of the borehole, a mechanism specifically excluded from study in this program. Laboratory tests to gain an understanding of cable shearing mechanisms and methods to harden against them may be even more important than the side loading test program presented here.

4. CYLINDRICAL STRUCTURES IN JOINTED ROCK

4.1 INTRODUCTION

In this chapter we describe results of two static uniaxial strain loading tests on 12-inch-diameter (0.3-m), 12-inch-high (0.3-m) jointed rock specimens containing 2-inch-diameter (50-mm) circular cylindrical tunnels. We performed these tests to study the influence on tunnel closure of a single set of joints. Tests were performed at two joint orientations: 0° and 45° between the normal to the joint plane and the direction of major loading.

In these tests we made active measurements of tunnel closure and tunnel liner strain. Tunnel closure was measured at two orientations: at the crown-invert and at the springlines. Tunnel liner strain was measured at four locations around the outside diameter of the liner: at the crown, at the invert, and at both springlines. Details of the instrumentation for these measurements are presented in Appendix A.

Complete specification of joint orientation is given by the angles between the normal to the joint-plane and three mutually orthogonal axes as shown in Figure 4.1. For the two models we tested, $\gamma = 90^{\circ}$ ($\pi/2$ rad); that is, the tunnel axis lies in the plane of the joints. Joint spacing was 0.33 inches (8.4 mm); hence, the tunnel-diamater-to-joint-spacing ratio was 6. The rock material was 16A rock simulant whose constituents[1] are:

Type I Cement; Source: Marquette Co., Brandon, MS	18.61%
Limestone sand (passing #12 sieve and retained on #16 sieve, saturated surface dry state); Source: Vulcan Materials Co., Calera, AL	61.37%

---

[1] S. A. Ragan, Waterways Experiment Station.
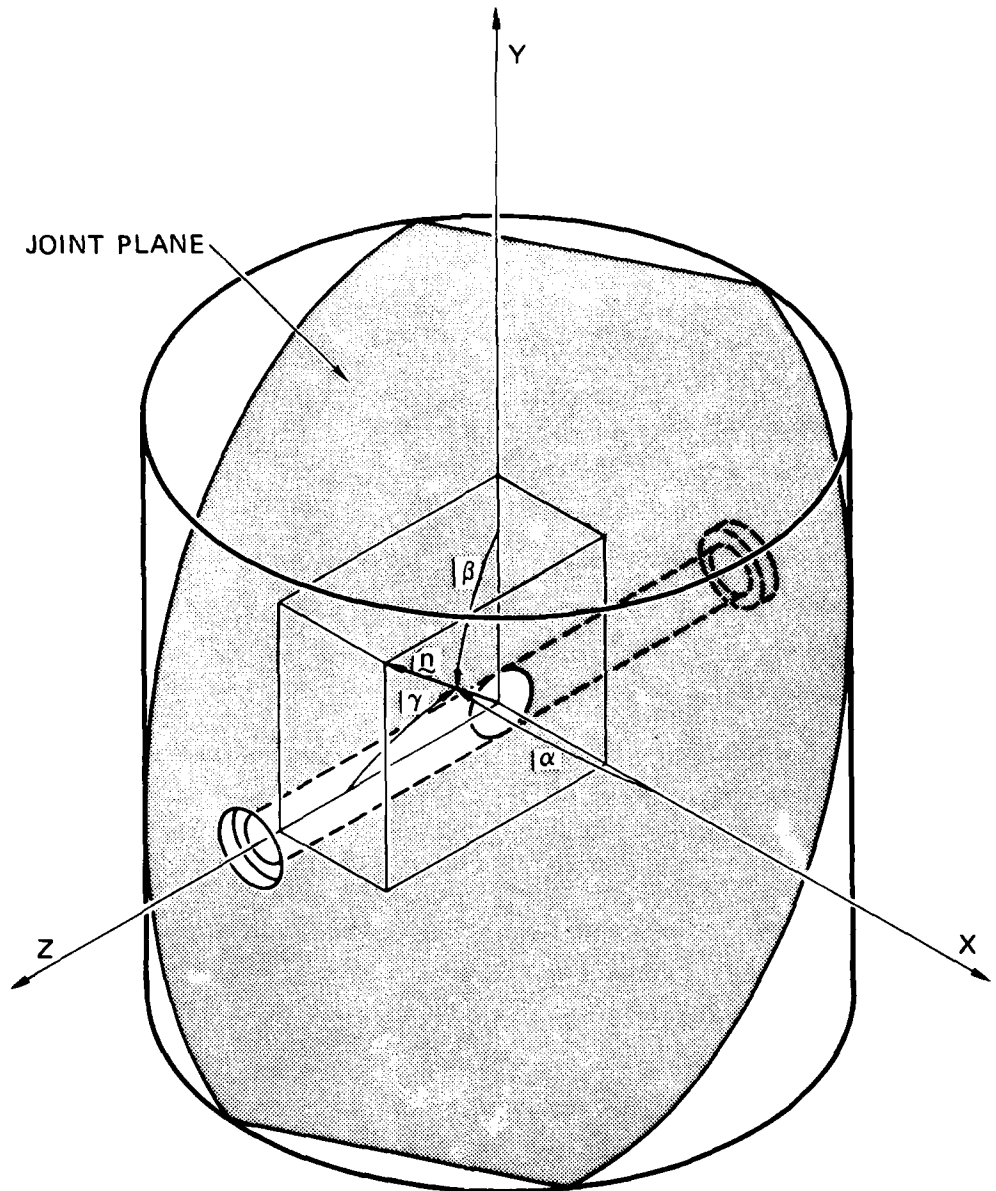
JOINT PLANE

MA-5762-22A

FIGURE 4.1   SCHEMATIC SHOWING JOINT ORIENTATION

$\underline{n}$ is normal to the joint plane.

87

Granite sand (passing #50 sieve and   6.62%
retained on #100 sieve, saturated
surface dry state); Source: Teton Construction Co.,
                                Cheyenne, WY

Water   13.40%
                                                      100.00%

Intact 16A simulant is characterized by the following constitutive
parameters:[2]

Young's Modulus $E = 3.08 \times 10^6$ psi   (21.2 GPa)

Poission's Ratio $\nu = 0.23$

Compressive Strength $\sigma_u = 3740$ psi   (25.8 MPa)

Friction Angle $\phi = 29^o$ (0.506 rad)

   The rock models were supplied by Waterways Experiment Station.
They were shipped to SRI where the tunnel was drilled and the reinforcing
structure was inserted.   Drilling tunnels in rock models is discussed
in the next subsection.

   The 12-inch-diameter (0.3-m) specimens were tested in the large-
scale triaxial testing machine [4].   Loading was controlled by a micro-
processor that monitors the outputs of strain gages mounted on the speci-
men to measure lateral (circumferential) strain.   Since we had not per-
formed a test using active tunnel instrumentation and automatic load
control, we performed a shake-down test on a specimen of intact SRI RMG
2C2.   The specimen was completely saturated and contained a 6061-T0
aluminum liner having $a/h = 11.5$.   The results of this test were com-
pared with those reported in Chapter 2 to insure proper functioning of
the load-controlling microprocessor and the tunnel instrumentation.
Results of this test are reported in Section 4.2.   Results of the two
tests on jointed models are reported in Section 4.3.

---

[2]R. L. Stowe, Waterways Experiment Station.

88

4.1.1   Drilling Tunnels in Rock Specimens

In the first 12-inch-diameter (0.3-m) specimens, tunnels were cast into the specimen [4]. We found this unsatisfactory because of thermal cracking while the specimen cured. Therefore, tunnels in all 12-inch-diameter (0.3-m) specimens are now drilled, just as for the 4-inch-diameter (0.1-m) specimens. Furthermore, it is not possible to cast tunnels into jointed specimens.

Tunnels are drilled with a 2-inch-diameter (50-mm) thin-wall core barrel and counterbored with a 4-inch-diameter (100-mm) flat-face barrel. The core barrel and flat-face barrel are shown in Figure 4.2.

To facilitate handling and aligning the specimen on the drill press, we enclosed and clamped the specimen in a drum as shown in Figure 4.3. The drum is placed in a box in which it is free to rotate. The front of the box is then sealed to collect the cooling water. Figure 4.4 shows the tunnel being drilled. Core barrel alignment is maintained by a bushing at the top of the box as shown. A pin through the box and drum above the axis of the drum prevents rock rotation. The core barrel is too short to drill the entire tunnel from one end. Therefore, the tunnel is drilled approximately halfway, the rock is rotated 180 degrees (π rad.) and then the tunnel is completed by drilling from the opposite side. The drum pin holes are indexed at 0 degrees and 180 degrees (0 and π rad.) to achieve accurate alignment.

The core obtained from the tunnel of an intact specimen, shown in Figure 4.5, may be used for performing unconfined compression tests. This permits Young's modulus and the unconfined compressive strength to be determined for each rock. The rough area near the center of the core is where the 0- and 180-degree (0- and π-rad.) drillings overlap. The roughness is removed by sliding the core barrel over the core and rotating it by hand.

MP-5762-15

FIGURE 4.2   THIN-WALL CORE BARREL (2-IN.-DIAMETER) AND FLAT-FACE BARREL
(4-IN.-DIAMETER) USED TO DRILL AND COUNTERBORE TUNNELS IN
ROCK SPECIMENS

(a) TRANSFERRING SPECIMEN FROM LIFT TO FIXTURE

(b) ENCLOSING SPECIMEN IN DRUM

(c) LOCKING SPECIMEN IN PLACE

(d) SEALING FRONT OF FIXTURE TO COLLECT COOLING WATER

MP-5762-16

FIGURE 4.3   PROCEDURE FOR MOUNTING ROCK SPECIMEN INTO DRILL FIXTURE

91

CORE BARREL ALIGNMENT BUSHING

DRUM LOCKING PIN

MP-5762-17

FIGURE 4.4   FIXTURE ON DRILL PRESS SHOWING CORE BARREL ALIGNMENT
BUSHING AND DRUM LOCKING PIN
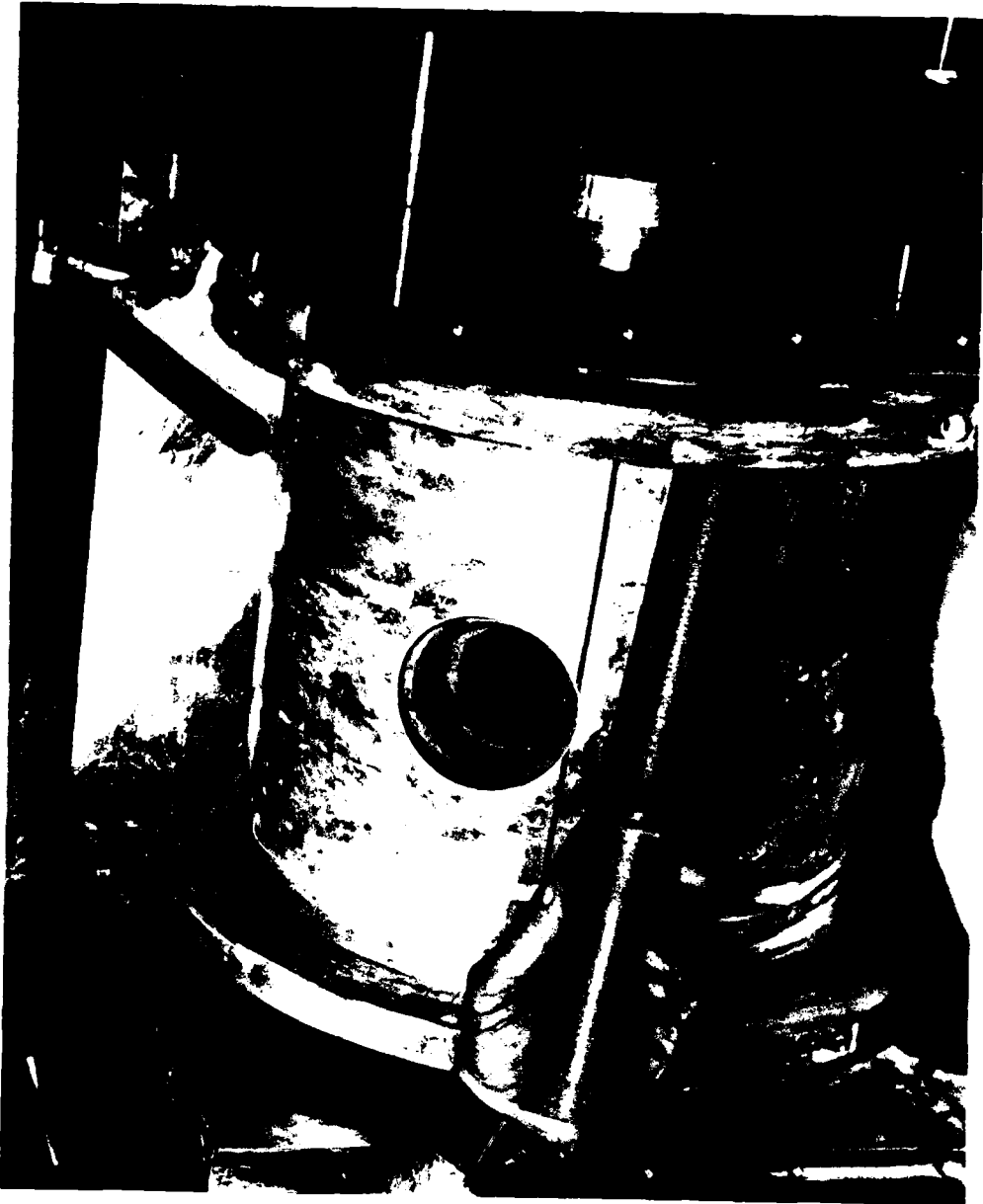
FIGURE 4.5 CORE REMOVED FROM TUNNEL OF INTACT ROCK

MP-5762-18

4.2   TESTS ON INTACT SRI RMC 2C2 SPECIMENS

We performed test LSUX-12 on a 12-inch-diameter (0.3-m) saturated specimen of SRI RMC 2C2. This rock material was chosen because we have a large amount of data from 4-inch-diameter (0.1-m) specimens for comparison [3] (see also Chapter 2). The reinforcing structure in this test was a 6061-T0 aluminum monocoque cylinder having a/h = 11.5, a larger scale model of the tunnel liner described in Chapter 2.

The specimen was loaded in uniaxial strain until the vertical tunnel closure was about 10 percent. We recorded with X-Y plotters lateral confining pressure and vertical tunnel closure as functions of the vertical pressure. Testing was stopped after each 500-psi (3.45-MPa) increment in vertical pressure to record data from digital display panels. This proved to be unsatisfactory, as we will discuss, so that in subsequent tests data were collected photographically from the digital display panels.

Figure 4.6 shows the load path for LSUX-12. To insure proper setting of the seals between vertical and lateral pressures, we began the test by increasing the vertical and lateral pressures manually to 600 and 200 psi (4.1 and 1.4 MPa), respectively. From this point onward, the pressures were automatically controlled by the microprocessor to maintain uniaxial strain. As we stated, the test was stopped at P_V = 1000 psi (6.9 MPa) and then after each additional 500 psi (3.45 MPa). While the test was stopped, the pressure decreased because the specimen was slowly compacting. These unloadings can be seen as nearly horizontal spikes in Figure 4.6. For comparison, the uniaxial strain load path determined from tests on 4-inch-diameter (0.1-m) specimens is drawn as a dashed line. The LSUX-12 load path followed this dashed line quite well until the vertical pressure reached 5.5 ksi (38 MPa). The pressure then dropped while data were collected from the digital display panel, as at lower pressures. However, when the test was resumed, the load path did not return to the dashed line as expected. We adjusted the pressures manually to move the loading pressure point to the dashed line, but when we returned control to the microprocessor, the loading

94
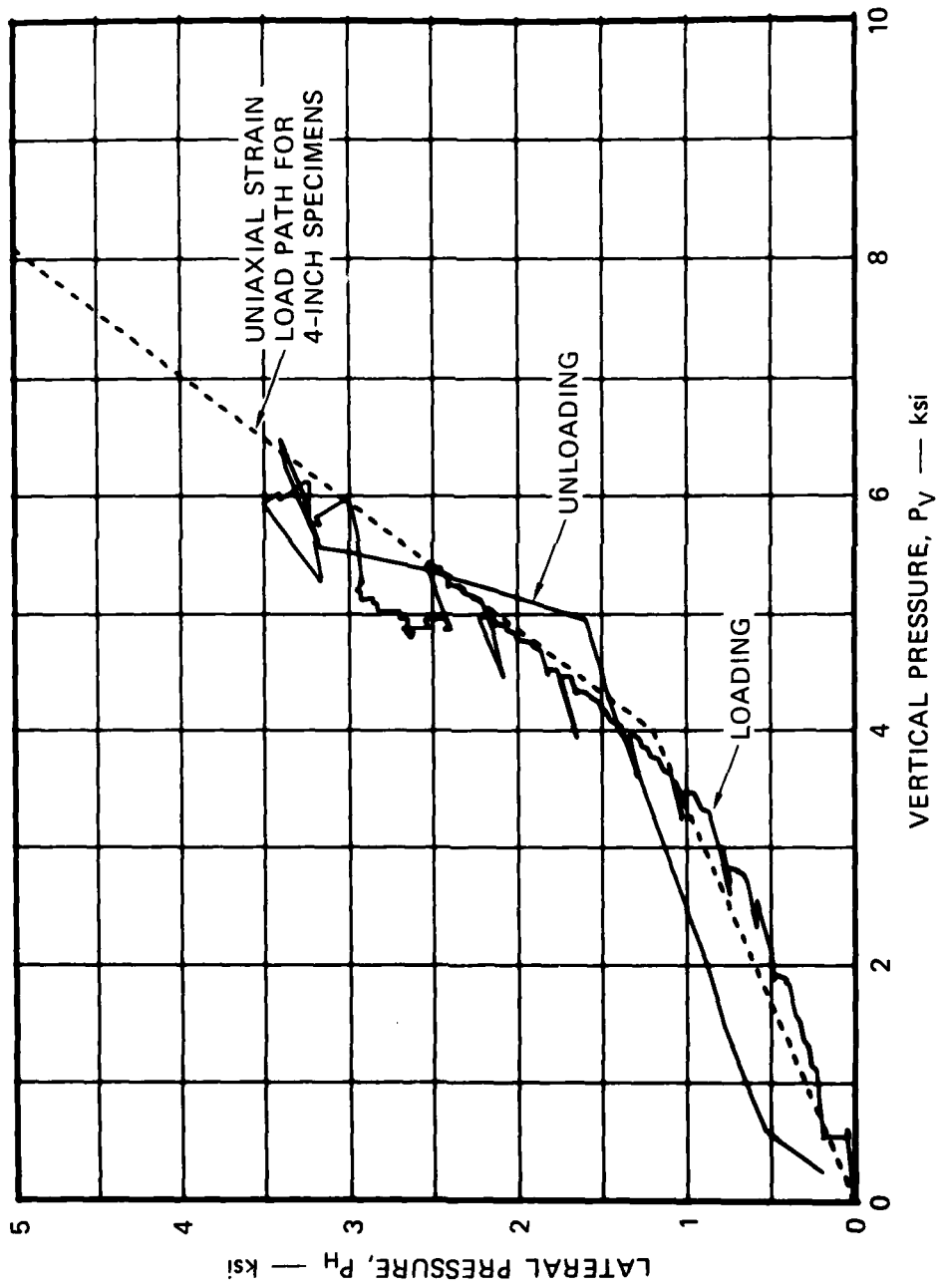
FIGURE 4.6   LATERAL CONFINING PRESSURE VERSUS VERTICAL PRESSURE FOR UNIAXIAL
STRAIN LOADING OF SATURATED SRI RMG 2C2 IN LSUX-12

point moved sharply away from the dashed line. The contribution to the specimen's strain history due to the plastic deformation that occurred while the test was stopped apparently changed the uniaxial strain load path significantly.[*] The specimen was then unloaded. The unloading path is also shown in Figure 4.6. Unloading is accomplished by opening solenoid valves. The action of the valves is too slow to maintain uniaxial strain, but it is always arranged to initially follow an over-confined path so that no additional tunnel deformation occurs.

Figure 4.7 shows vertical tunnel closure plotted as a function of vertical pressure. Tunnel closure is plotted from two tests on 4-inch-diameter (0.1-m) specimens for comparison. Initially, the data from the large and small specimens agree, but for vertical pressures greater than about 3.5 ksi (24 MPa) closure in the large specimen is greater than in the small specimens. The difference in tunnel closure may be due to differences in porewater pressure, but a theoretical analysis that includes transient porewater effects needs to be performed to test this explanation.

Figure 4.8 shows springline tunnel closure as a function of vertical pressure. The data are those taken periodically from the digital display panel. The tunnel moves outward slightly at the spring-lines, achieving a maximum negative closure of -0.4 percent. Late in the test the springlines move inward, but by then the load path had deviated from the desired path as discussed earlier.

After the test, we sectioned the specimen to obtain the photo-graph in Figure 4.9. Test LSUX-12 is compared with two previous large (dynamic) tests, LDUX-9 and LDUX-10 shown in Figures 4.10 and 4.11. The tunnel liner in all three tests was the same. Tunnels were cast in the specimens for LDUX-9 LDUX-10, whereas the tunnel was drilled in LSUX-12. The larger cracks near the tunnel in LDUX-9 and LDUX-10 are probably casting flaws and their contribution to tunnel closure in LDUX-9 is

---

[*]The lateral confining pressure required for uniaxial strain is path-dependent; see Chapter 6.3 of reference [3].
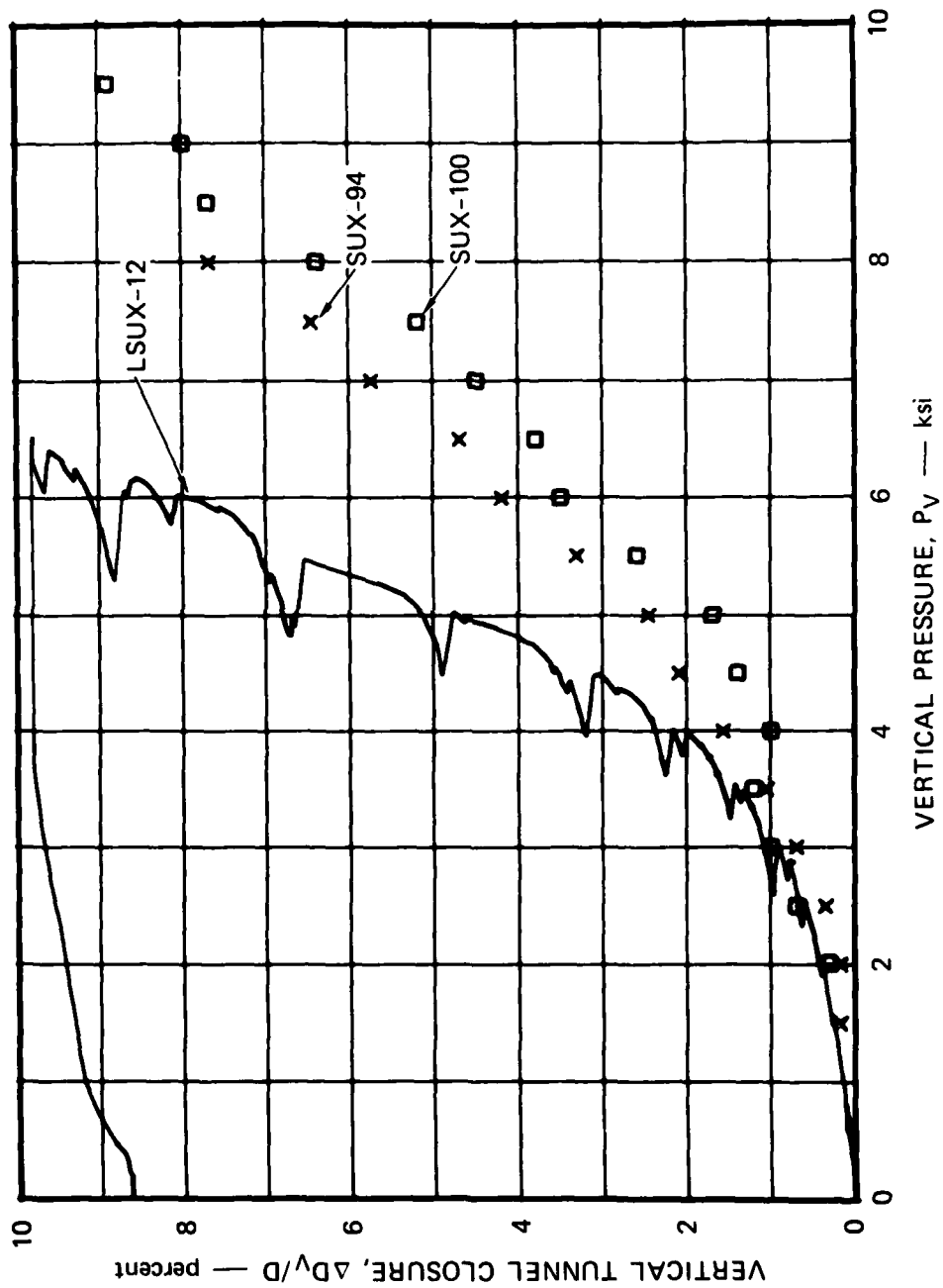
FIGURE 4.7 VERTICAL TUNNEL CLOSURE VERSUS VERTICAL PRESSURE FOR UNIAXIAL STRAIN LOADING OF SATURATED SRI RMG 2C2

6061-T0 aluminum liner, a/h = 11.5

MA-5762-24

97
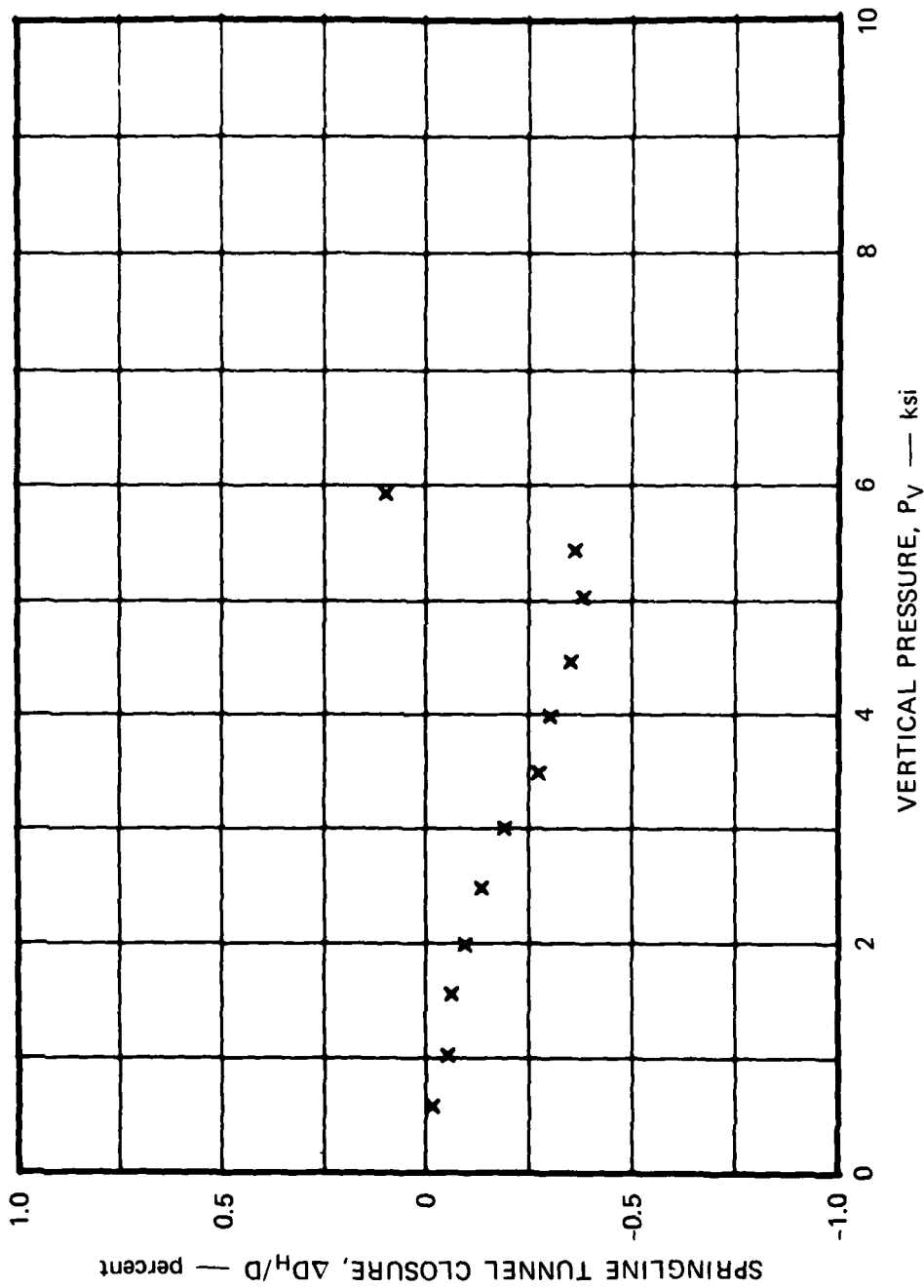
FIGURE 4.8 SPRINGLINE TUNNEL CLOSURE VERSUS VERTICAL PRESSURE FOR UNIAXIAL STRAIN LOADING
OF SATURATED SRI RMG 2C2 IN LSUX-12

6061-T0 aluminum liner, a/h = 11.5

MA-5762-25
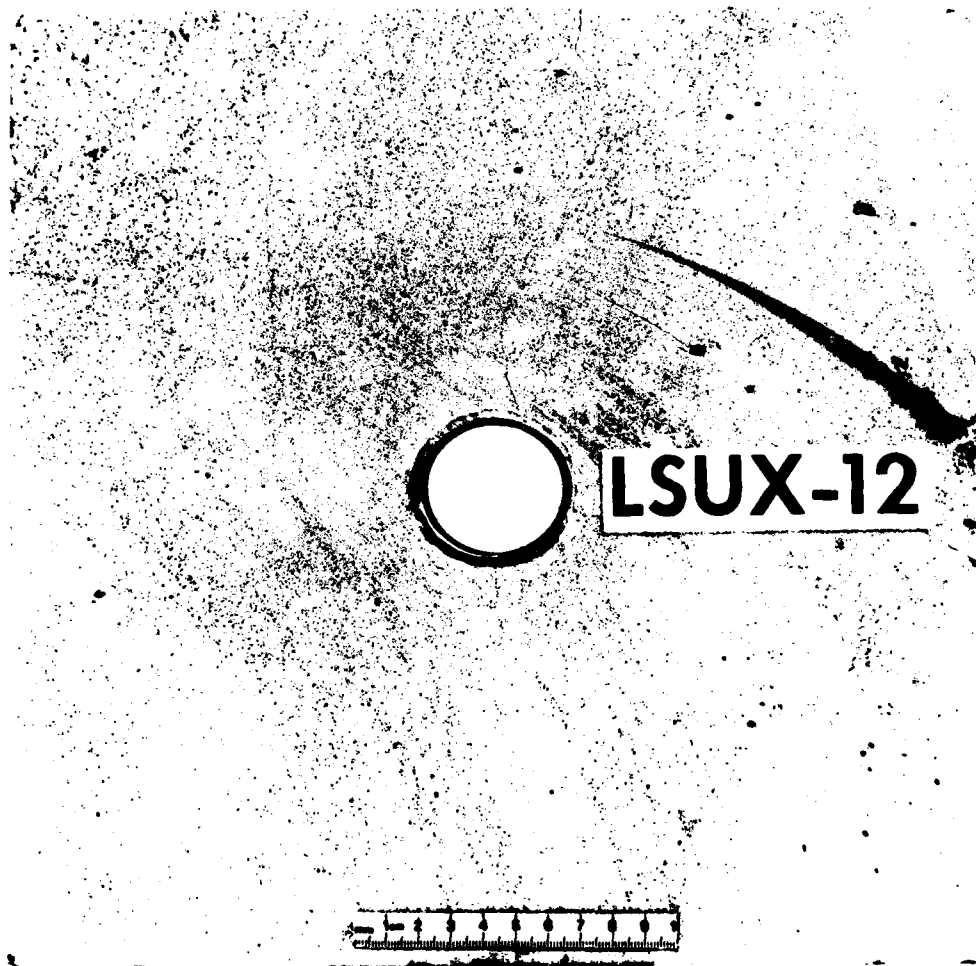
LSUX-12

MP-5762-26

FIGURE 4.9 SECTIONED SPECIMEN FROM STATIC UNIAXIAL STRAIN TEST LSUX-12
(P_V = 6.5 ksi, P_H = 3.5 ksi, $\Delta D_V/D_V$ = 10%, $\Delta D_H/D_H$ = 0.4%)

99
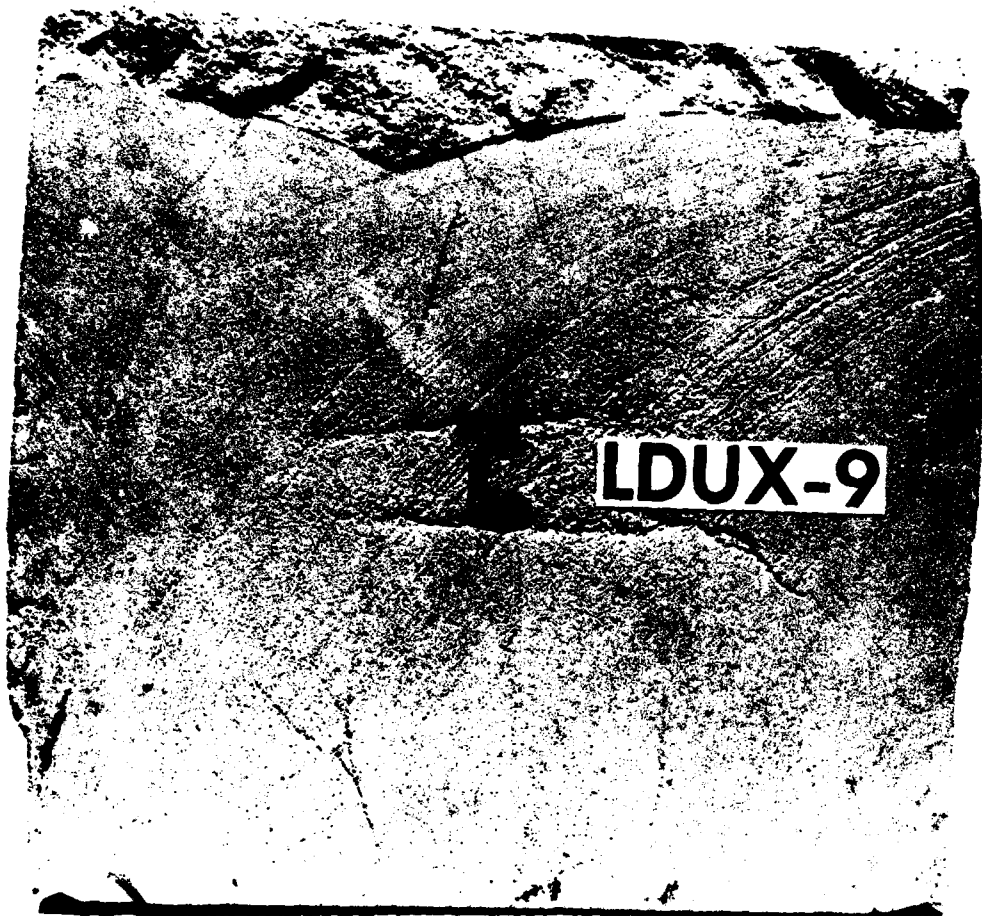
MP-4121-145

FIGURE 4.10   SECTIONED SPECIMEN FROM DYNAMIC UNIAXIAL STRAIN TEST
LDUX-9 (P_V = 10.5 ksi, P_H = 7 ksi, $\Delta D_V/D_V$ = 38.7%, $\Delta D_H/D_H$ = 100%)
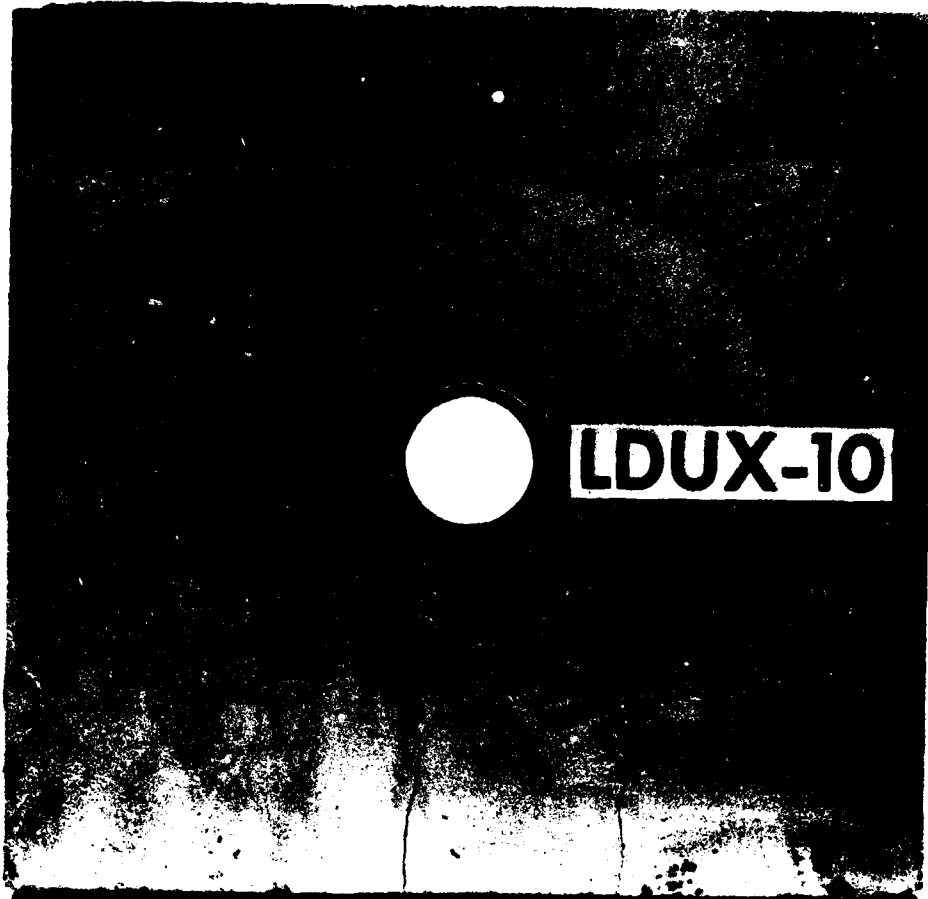
MP-4121-144

FIGURE 4.11   SECTIONED SPECIMEN FROM DYNAMIC UNIAXIAL STRAIN TEST
LDUX-10 (P_V = 7 ksi, P_H = 4 ksi, $\Delta D_V/D_V$ = 0.82%, $\Delta D_H/D_H$ = -0.77%)

101

significant. Pretest flaws are responsible for other anamolous results in dynamic tests on 12-inch-diameter (0.3-m) specimens [4]. We conclude, therefore, that drilling tunnels is superior to casting tunnels in the larger specimens.

4.3   TESTS ON JOINTED ROCK SPECIMENS

We performed two tests on jointed rock specimens whose tunnels were reinforced with 1015 steel liners having mean-radius-to-wall-thickness ratio, $a/h = 12.5$. Joint orientation, in terms of the three angles defined in Figure 4.1, is $\alpha = 90^{\circ}$ ($\pi/2$ rad), $\beta = 0^{\circ}$ (0 rad) and $\gamma = 90^{\circ}$ ($\pi/2$ rad) in the first test, LSUX-13, and $\alpha = 45^{\circ}$ ($\pi/4$ rad, $\beta = 45^{\circ}$ ($\pi/4$ rad) and $\gamma = 90^{\circ}$ ($\pi/2$ rad) in the second test, LSUX-14.

Figures 4.12 and 4.13 show posttest sections of the specimens, and Figures 4.14 and 4.15 show enlargements of the tunnel vicinity. The first two photographs show that no block motion occurred, indicating that tunnel closure is due to plastic deformation and fracture of the plates and probably localized slipping on the joints. Plastic deformation of the plates is evidenced by the bending they experience near the tunnel. Bending is especially evident in LSUX-13. Several plates near the tunnel cracked in each specimen as shown by the enlargements of the tunnel region. The cracks are normal to the joints, and do not intersect the tunnel at the orientations observed in intact rock [1]. Cracks observed in intact rock specimens are shear cracks that intersect the tunnel near the springlines and whose trajectories follow slip lines [2]. In the jointed rock specimen cracking occurs near the crown and invert rather than near the springlines. The bent shape of the plates suggest that the cracks are from bending rather than from shear flow as in intact rock.

Figures 4.12 and 4.13 show that the 0.33-inch-thick (8.47-mm) plates are squeezed tightly together during the test; individual planes are barely distinguishable except where the specimen was disturbed during posttest handling. Unfortunately, the plates intersecting the tunnel were disturbed in both specimens. Records of tunnel closure,

102
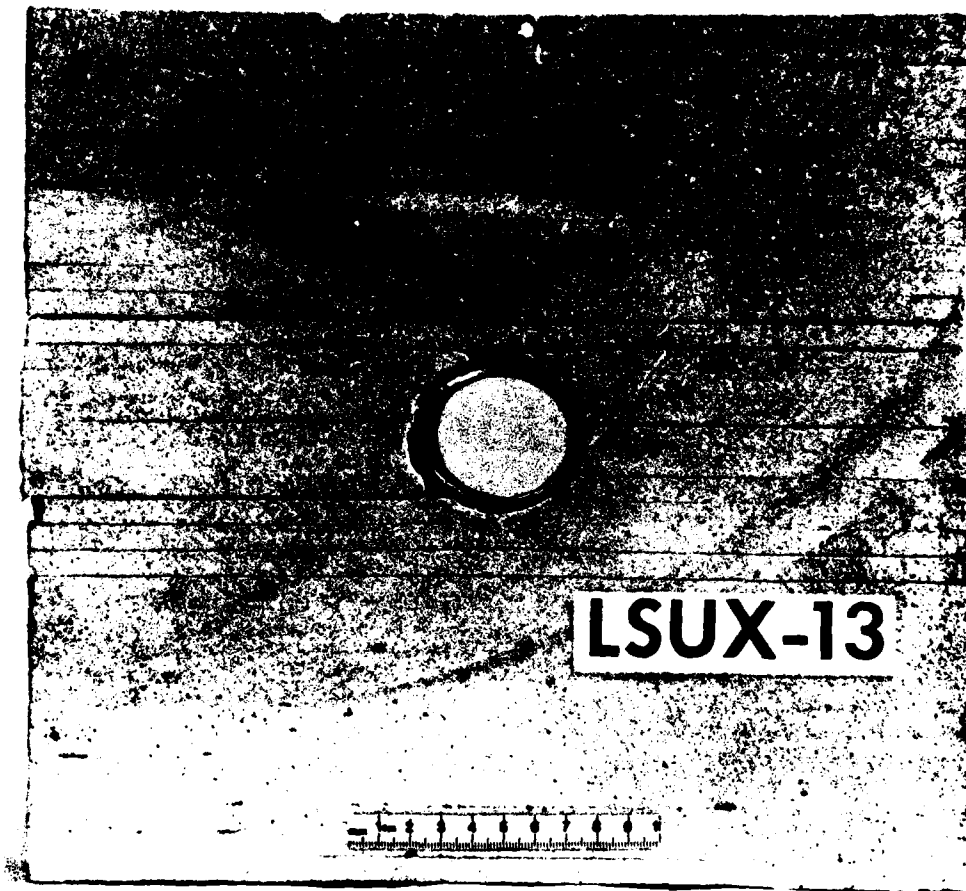
MP-5762-27

FIGURE 4.12   SECTIONED SPECIMEN FROM STATIC UNIAXIAL STRAIN TEST LSUX-13
(P_V = 17 ksi, P_H = 7.4 ksi, $\Delta D_V/D_V$ = 10.2%, $\Delta D_H/D_H$ = 0.25%)

MP-5762-28

FIGURE 4.13 SECTIONED SPECIMEN FROM STATIC UNIAXIAL STRAIN TEST LSUX-14
$(P_V = 12$ ksi, $P_H = 4.6$ ksi, $\Delta D_V/D_V = 8.90\%$, $\Delta D_H/D_H = -5.10\%)$
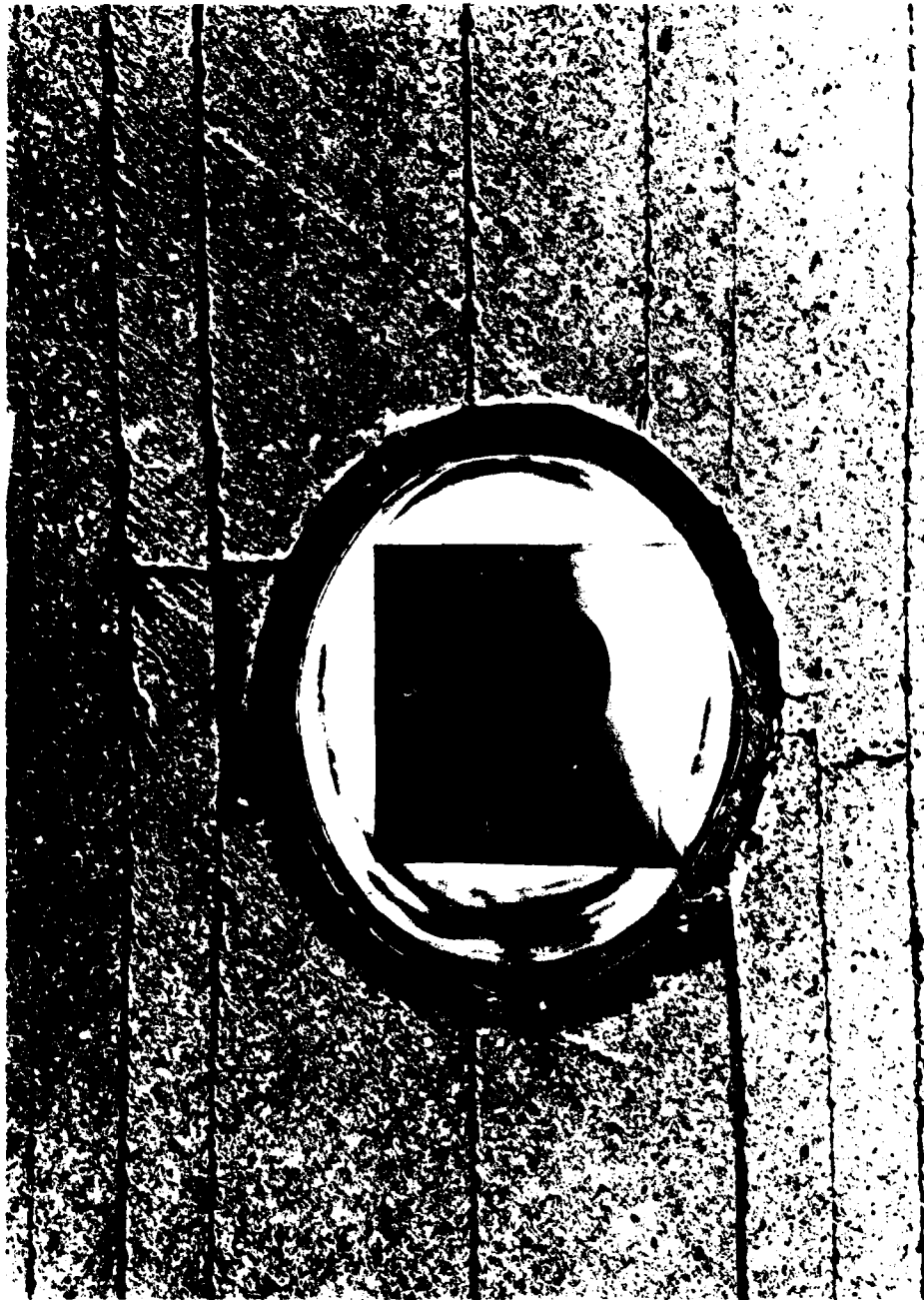
FIGURE 4.14   ENLARGEMENT OF TUNNEL REGION IN LSUX-13 SPECIMEN

MP-5762-29

105

FIGURE 4.15   ENLARGEMENT OF TUNNEL REGION IN LSUX-14 SPECIMEN

MP-5762-30

106

presented later, indicate that inital gaps* between the plates closed
when we applied the first increment of vertical pressure.

Figure 4.16 shows the uniaxial strain load paths for LSUX-13
and LSUX-14. The load paths are roughly the same except at low pressure
where the LSUX-13 load path increases sharply. We did not stop loading
in these tests as we did in LSUX-12, the test on intact SRI RMG 2C2.
The load paths are very smooth. In fact, in LSUX-14, cycling of the hydr-
aulic pumps (the very small steps in the LSUC-13 load path) is not even
evident. Unloading, however, is fairly coarse because of the dump valves'
slow action described previously.

The load path data plotted in Figure 4.16 is taken from an X-Y
plotter record. We did not construct the load paths from pressure data
recorded on analog tape because of noise introduced by our playback and
digitizing procedure. (Methods have since been developed to obtain
noise-free records from the tape recording). Although the tunnel closure
and tunnel liner strain data presented below were obtained from analog
tape and contain this noise, the plots are adequate. However, because
the load path is important in uniaxial strain loading tests, we present
data recorded directly from the instrument signals by an X-Y plotter.

Figure 4.17 plots vertical tunnel closure as a function of
vertical pressure for both tests. For comparison we also plotted
closure data from test SUX-104, a uniaxial strain loading test on a
4-inch-diameter (0.1-m) specimen of intact 16A rock. Tunnel closure
in both jointed rock tests increases sharply at very low vertical pressure.
This is due to closing the initial gaps between the plates. The magni-
tude of the closure, about 0.7 percent in LSUX-13 and nearly 1 percent
in LSUX-14, indicates that the inital gap between plates is approximately
2 mils (0.05 mm).[†] After this initial jump, vertical tunnel closure

---

[*] These gaps are due to the plates resting on a relatively few high points
so that the plates are easily deformed at low pressure.

[†] Because of the 45° ($\pi/4$ rad) angle between the joints and the vertical,
we expect the initial closure in LSUX-14 to be $\sqrt{2}$ larger than that in
LSUX-13.

107
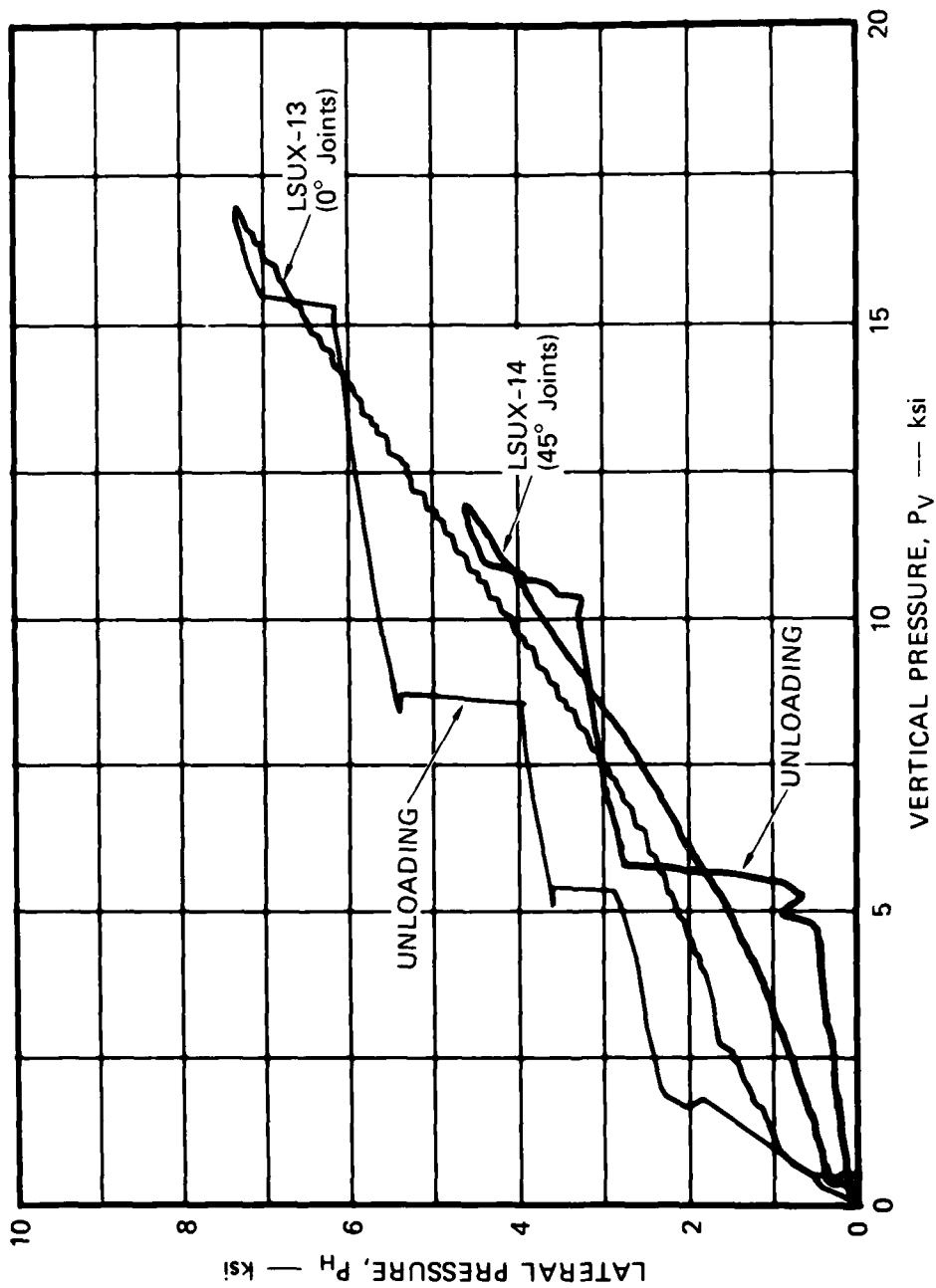
FIGURE 4.16 LATERAL CONFINING PRESSURE VERSUS VERTICAL PRESSURE FOR UNIAXIAL STRAIN LOADING OF 16A JOINTED ROCK SPECIMENS
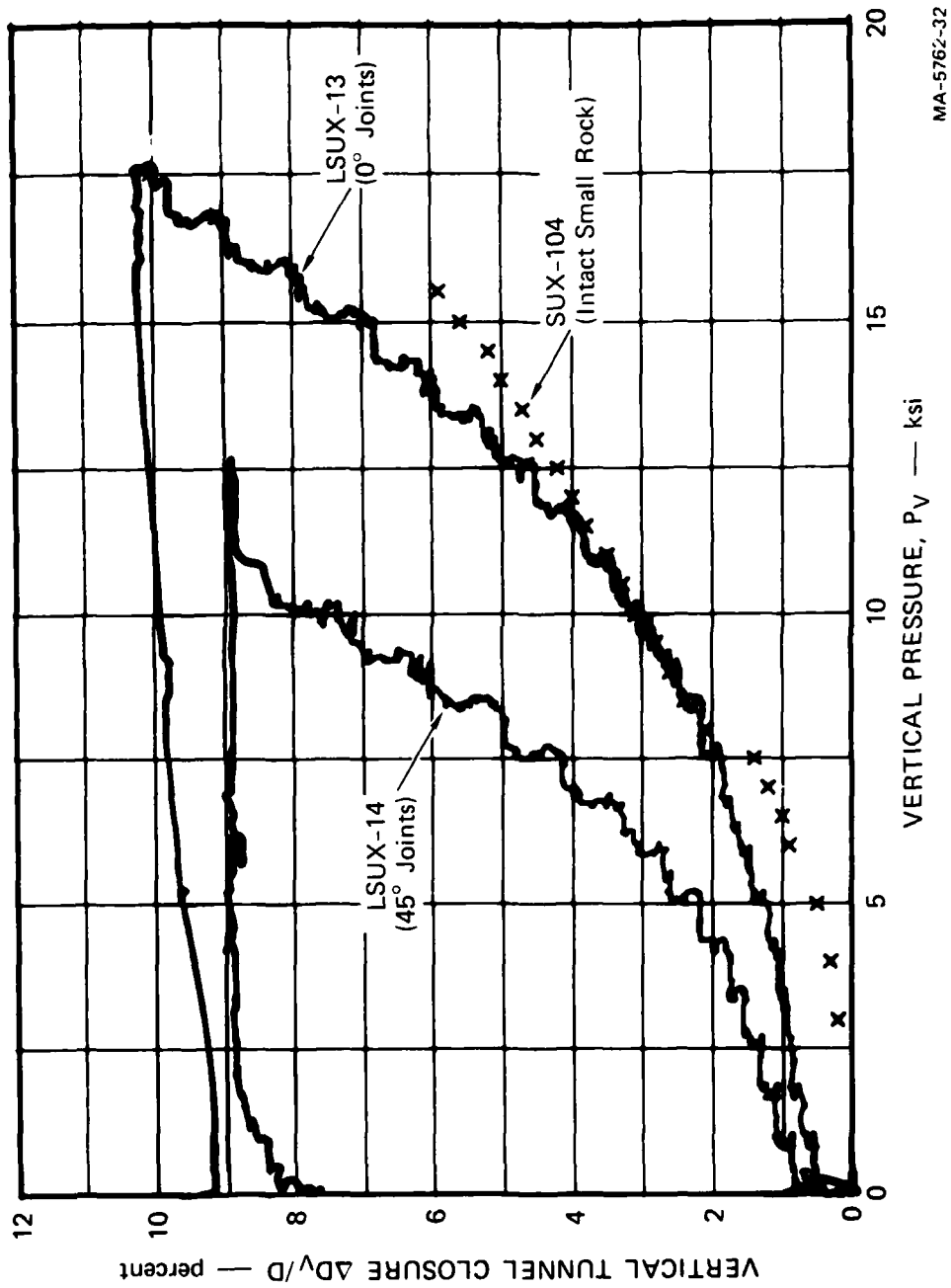
MA-5762-31

FIGURE 4.17   VERTICAL TUNNEL CLOSURE VERSUS VERTICAL PRESSURE FOR UNIAXIAL
STRAIN LOADING OF JOINTED 16A ROCK SPECIMENS

Data from a test on an intact 4-inch-diameter specimen, SUX-104, is plotted for
comparison.   1015 steel liner a/h = 12.5.

increases smoothly as the vertical pressure increases. Vertical tunnel closure is greater in LSUX-14 (45° joints) than in LSUX-13 (0° joints), indicating that for jointed rock with a joint normal further from the vertical (the angle β is larger) the rock-and-tunnel structure is weaker. Tunnel closure in LSUX-13, where the joint normal is vertical, is about the same as in SUX-104, an intact specimen. The similarity is expecially strong if we subtract from the LSUX-13 data the initial 0.7 percent closure.

Figure 4.18 plots springline tunnel closure as a function of vertical pressure. Springline closure differs markedly between LSUX-13 and LSUX-14. In both tests the springlines moved outward (negative closure) initially as the gaps between the plates closed. In LSUX-13 (0° joints), the springlines did not move further until late in the test when they moved slightly inward, resulting in a net inward closure of about 0.25 percent at maximum load. Qualitatively, this is the behavior we observe in tests on intact rock [2,3]. In LSUX-14 (45° joints), however, the springlines continue to move outward as the vertical pressure increases, and at peak load, tunnel closure at the springlines is -5.1 percent. This outward position changes only slightly on unloading.

Figure 4.19 plots tunnel liner strain at the crown as a function of vertical pressure. The strain gages are mounted on the outside of the liner and their output is due to both circumferential compression and bending. Gages in both tests indicate tensile strain, suggesting that bending (increasing curvature) dominates over circumferential compression. However, the oval shape of the liner suggests that the curvature at the crown and invert decreased. We have no explanation for this apparent discrepancy at present. The maximum strain at the crown is about 2 percent in LSUX-13 and 1.7 percent in LSUX-14.

Figure 4.20 plots tunnel liner strain at a springline as a function of vertical pressure. The strain gages here are also mounted on the outside of the liner. As at the crown, gages in both tests indicate tensile strain so bending dominates circumferential compression at the springlines as well. Strains at the springlines are larger than
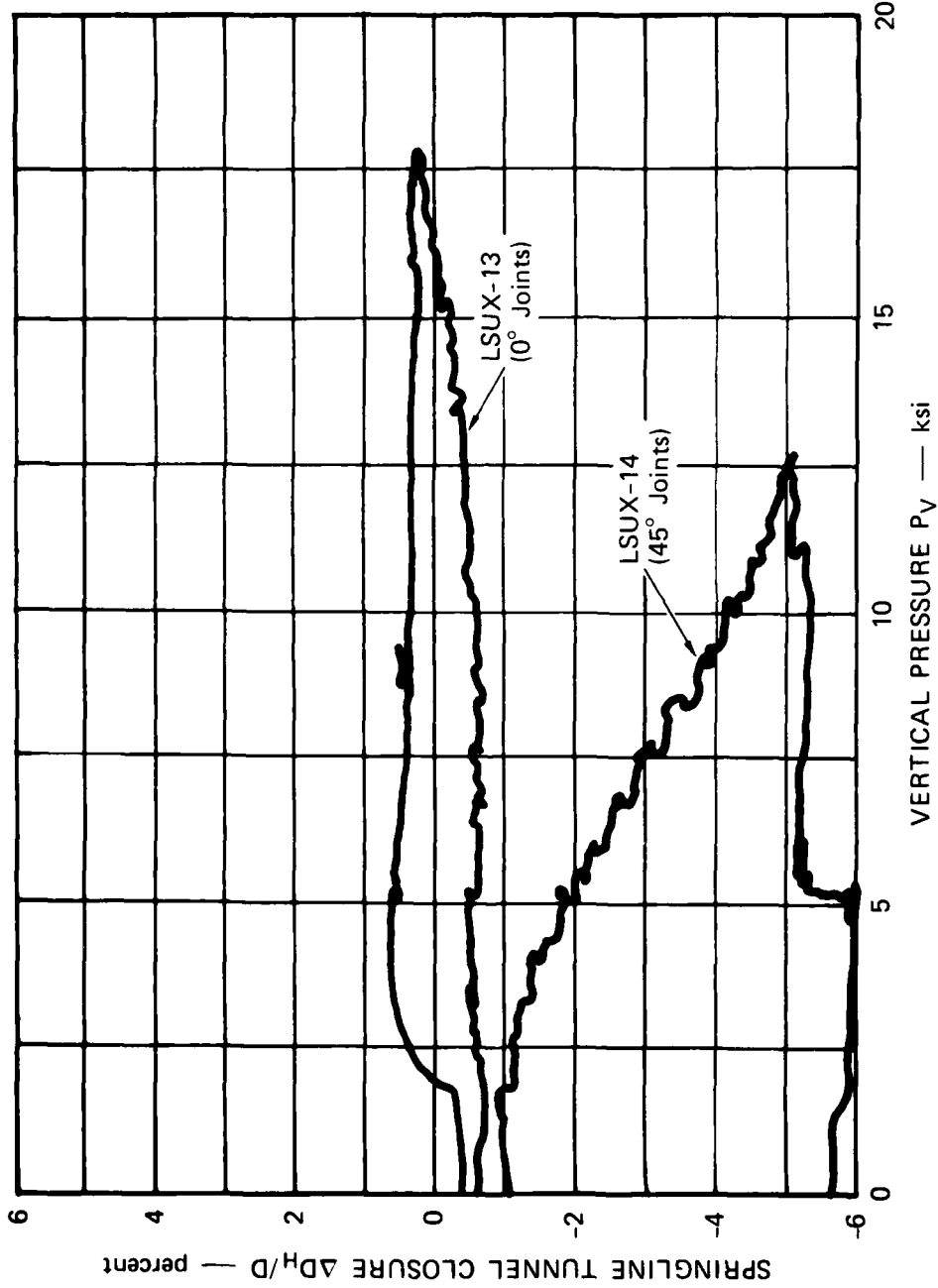
FIGURE 4.18   SPRINGLINE TUNNEL CLOSURE VERSUS VERTICAL PRESSURE FOR UNIAXIAL
STRAIN LOADING OF JOINTED 16A ROCK SPECIMENS

1015 steel liner, a/h = 12.5

111
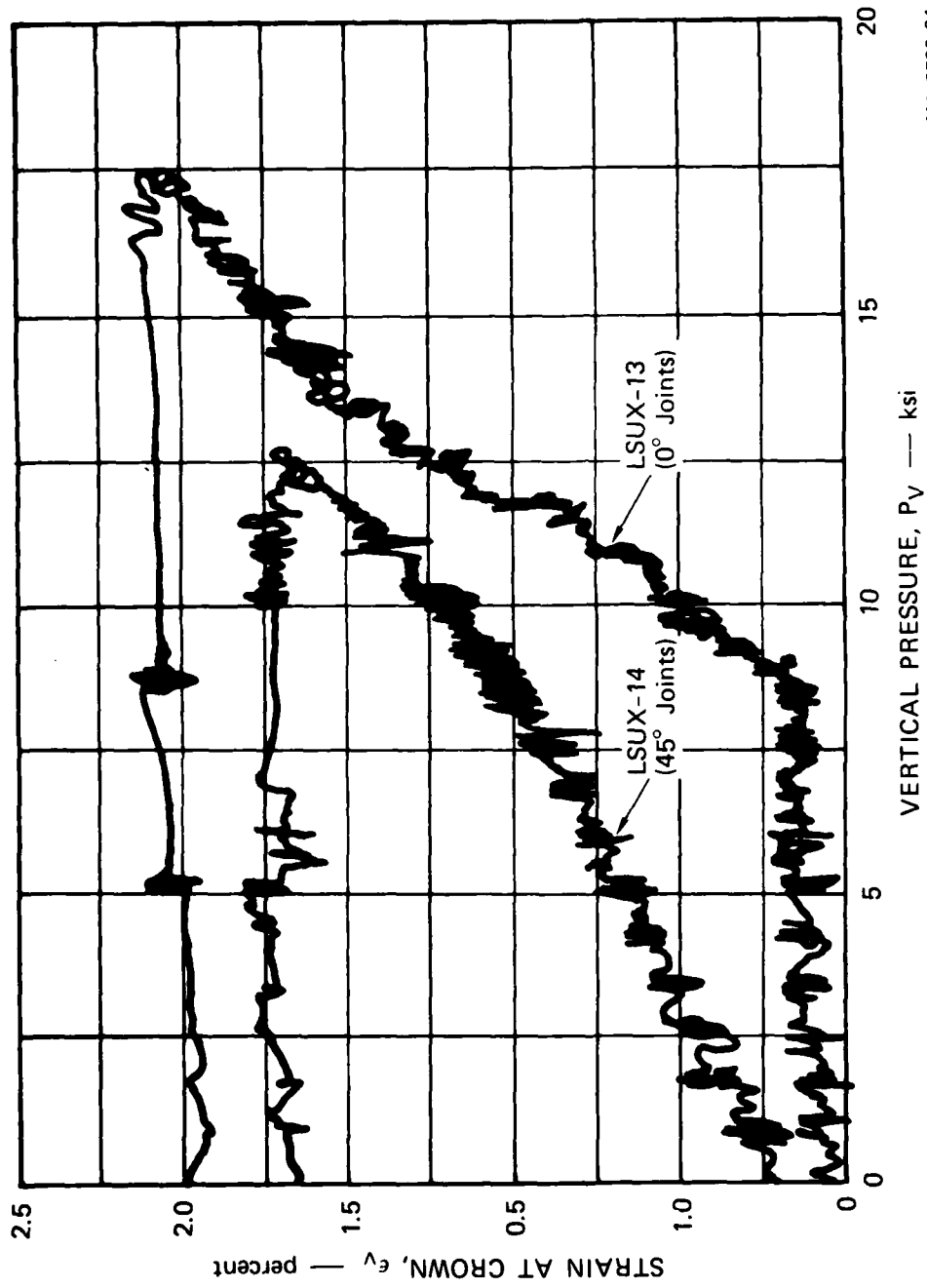
FIGURE 4.19 TUNNEL LINER STRAIN AT THE CROWN VERSUS VERTICAL PRESSURE FOR UNIAXIAL STRAIN LOADING OF JOINTED 16A ROCK SPECIMENS

1015 steel liner, a/h = 12.5. Gages mounted on outside of liner.
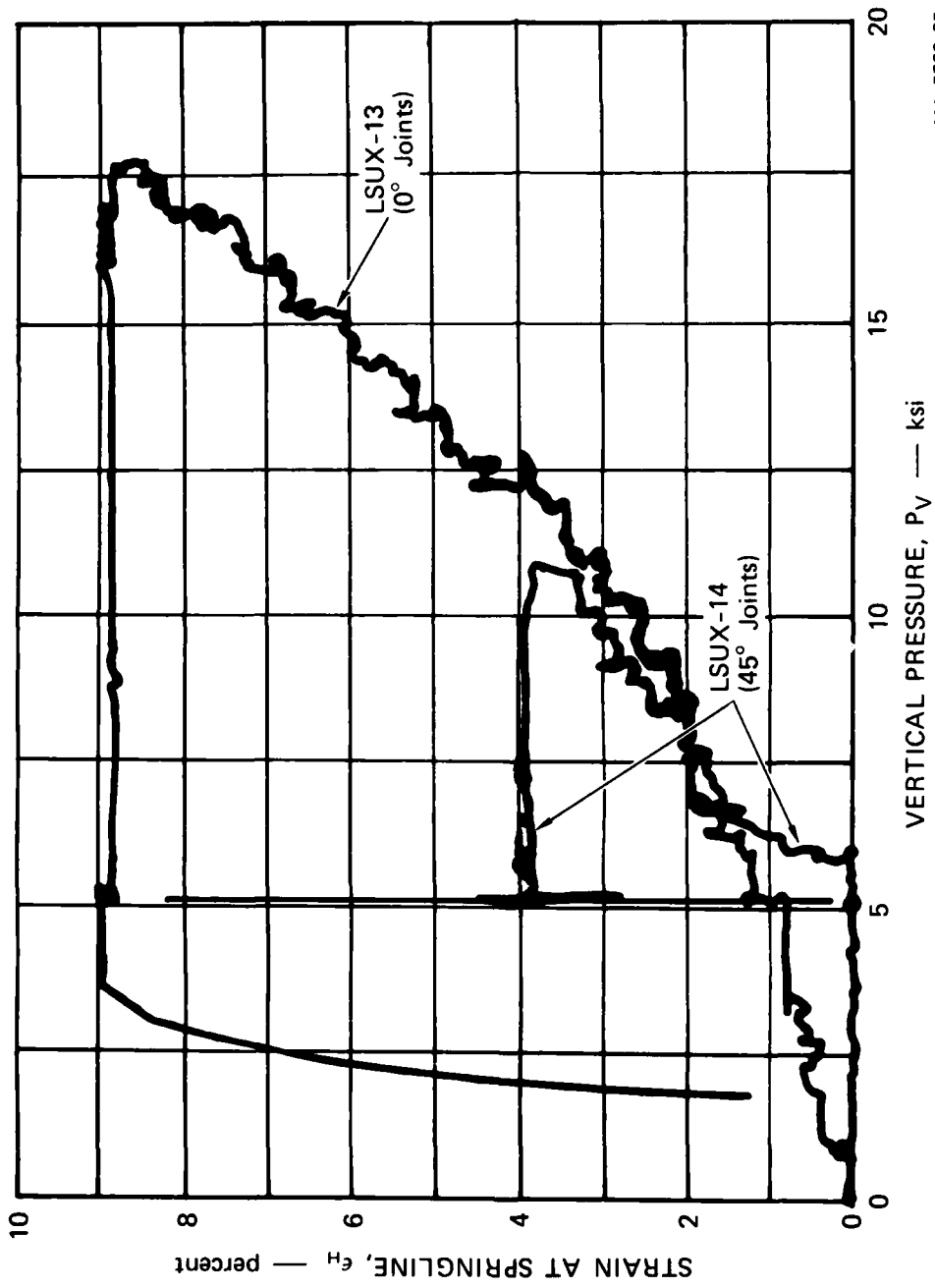
MA-5762-34

FIGURE 4.20 TUNNEL LINER STRAIN AT A SPRINGLINE VERSUS VERTICAL PRESSURE FOR
UNIAXIAL STRAIN LOADING OF JOINTED 16A ROCK SPECIMENS

1015 steel liner, a/h = 12.5. Gages mounted on outside of liner

MA-5762-35

113

those at the crown; the strain at peak load is about 8.8 percent in LSUX-13 and about 4 percent in LSUX-14.

In future tests we will mount strain gages inside the liner as well as outside. The additional tunnel liner strain data will permit us to study quantitatively tunnel liner bending and circumferential compression.

4.4   SUMMARY AND CONCLUSIONS

We performed three static uniaxial strain loading tests on 12-inch-diameter (0.3-m) specimens that contained reinforced 2-inch-diameter (50-mm) tunnels. The first specimen tested was an intact SRI RMG 2C2 model while the second and third specimens were jointed 16A rock simulant models having different joint orientations.

A microprocessor controlled the load path in these tests. Comparison of the load path for the intact SRI RMG 2C2 specimen with that obtained manually for similar 4-inch-diameter specimens showed that the microprocessor functions properly.

Results from tests on the jointed specimens showed that joint orientation influenced greatly the tunnel deformation: vertical tunnel closure in LSUS-14 (45° joints) was much greater than in LSUX-13 (0° joints) and the springlines moved outward considerably in LSUX-14 and inward slightly in LSUX-13. This quantitative as well as qualitative difference in tunnel closure indicates the need for further study of the influence of joints on tunnel deformation. More data regarding the effect of the orientation of a single set of joints are necessary for a fundamental understanding of joint/tunnel interaction. Specimens with two or more sets of joints also need to be tested to model realistically highly jointed, hardrock sites.

5.   THEORETICAL ANALYSIS OF ELLIPTICAL STRUCTURES

5.1   INTRODUCTION

This study investigated possible advantages of elliptical structures over circular structures in an elastic-plastic rock medium. A plane strain elastic analysis [11] shows that under side-on loading, a deep-based structure of elliptical cross section is more efficient than one of circular cross section. That is, an analysis of biaxial compression along the major and minor axes of an unlined elliptical cavity shows that the tangential stress is constant along the cavity wall if the ratio of the loading stresses is equal to the ratio of the major and minor axes of the ellipse. As a result, for Poisson's ratio ν = 0.33, incipient yielding of the rock occurs at a loading pressure 68 percent greater for the elliptical structure than for the circular structure. Figure 5.1 shows a schematic of the problem. To determine if elliptical structures retain their advantage during plastic deformation, we performed plane strain elastic-plastic analyses for both circular and elliptical structures.

We studied three cases: unlined cavities with no internal pressure, cavities with a uniform internal pressure P_i = 2000 psi (13.8 MPa), and cavities lined with a thin monocoque cylinder. The value for P_i was chosen to correspond to the symmetric yield pressure of the circular liner. We chose a thin steel liner having R/h = 20, where R is the radius of the circular cavity and h is the liner wall thickness. The steel was represented by an elastic-perfectly plastic Mises model with Young's modulus E = 30 x 10^6 psi (207 GPa), Poisson's ratio ν = 0.3, and yield stress σ_y = 40,000 psi (275 MPa).
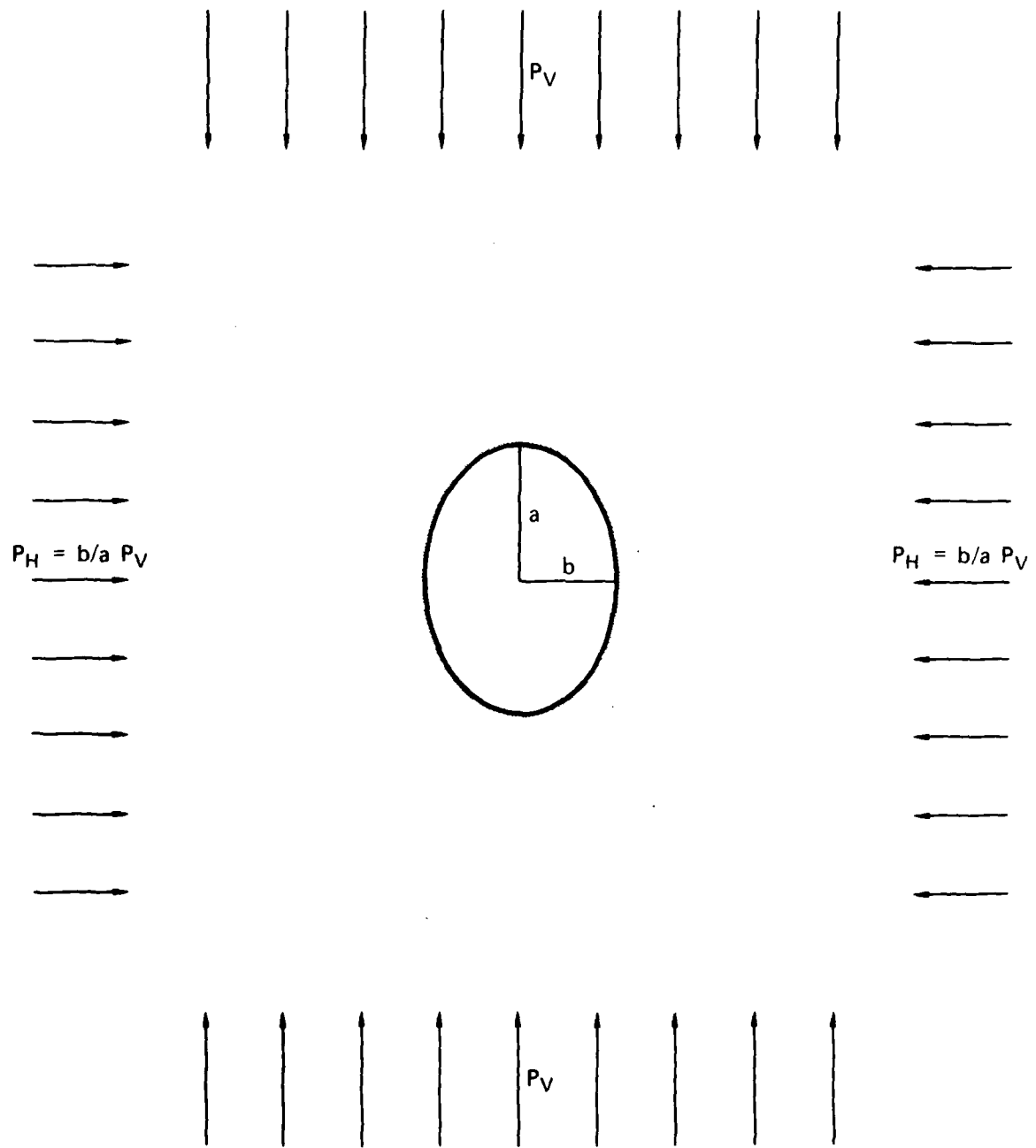
FIGURE 5.1   SCHEMATIC SHOWING BIAXIAL COMPRESSION OF INFINITE SOLID CONTAINING
AN ELLIPTICAL HOLE

5.2 PROBLEM FORMULATION AND SOLUTION

As a common basis, we studied elliptical and circular cavities of equal cross-sectional area. The ratio of the loading pressure, P_H/P_V, was taken to equal 1/2 (the stress ratio for uniaxial strain loading with Poisson's ratio $\nu = 0.33$). The elliptical cavity was therefore chosen with eccentricity $e = 0.866$ so that the ratio $b/a = 1/2$. To make the area of the ellipse ($A = \pi ab$) equal to the area of a circle of radius R ($A = \pi R^2$), we set $a = \sqrt{2} R$ and $b = R/\sqrt{2}$.

The rock medium surrounding the cavities has properties similar to tuff: Young's moduls $E = 1 \times 10^6$ psi (6.9 GPa), Poisson's ratio $\nu = 0.33$, unconfined compressive strength $\sigma_u = 2600$ psi (18 MPa), and friction angle $\phi = 10^O$ (0.175 rad). The rock was modeled as linear elastic-perfectly plastic with yield behavior governed by the Drucker-Prager criterion and associated flow rule. The rock material was therefore dilatant.

We used the finite element code NONSAP to obtain numerical solutions. Calculations of tunnel closure for unlined cavities with no internal pressure and for lined cavities had a mesh size equal to 10R. Calculations for cavities with an internal pressure P_i had a mesh size equal to 32R. Comparison of results from these two meshes showed that tunnel closure was not influenced greatly by mesh size.

As an initial check on the numerical technique, we used NONSAP to calculate the closure of the unlined elliptical cavity in a linearly elastic medium subjected to biaxial compression with $P_H/P_V = 1/2$. Results agreed with those obtained analytically.

5.3 RESULTS

Results of the elastic-plastic analyses show that elliptical structures do not retain their advantage over circular structures. After yielding begins, the plastic zones spread from the tunnel similarly for both the circular and elliptical structure, but the elliptical structure is weaker at the springlines. Figures 5.2 and 5.3 show the plastic zone around the tunnel at $P_V = 6000$ psi and 7500 psi (41.4 MPa and 51.7 MPa) for the lined circular and elliptical cavities with no internal pressure.

117
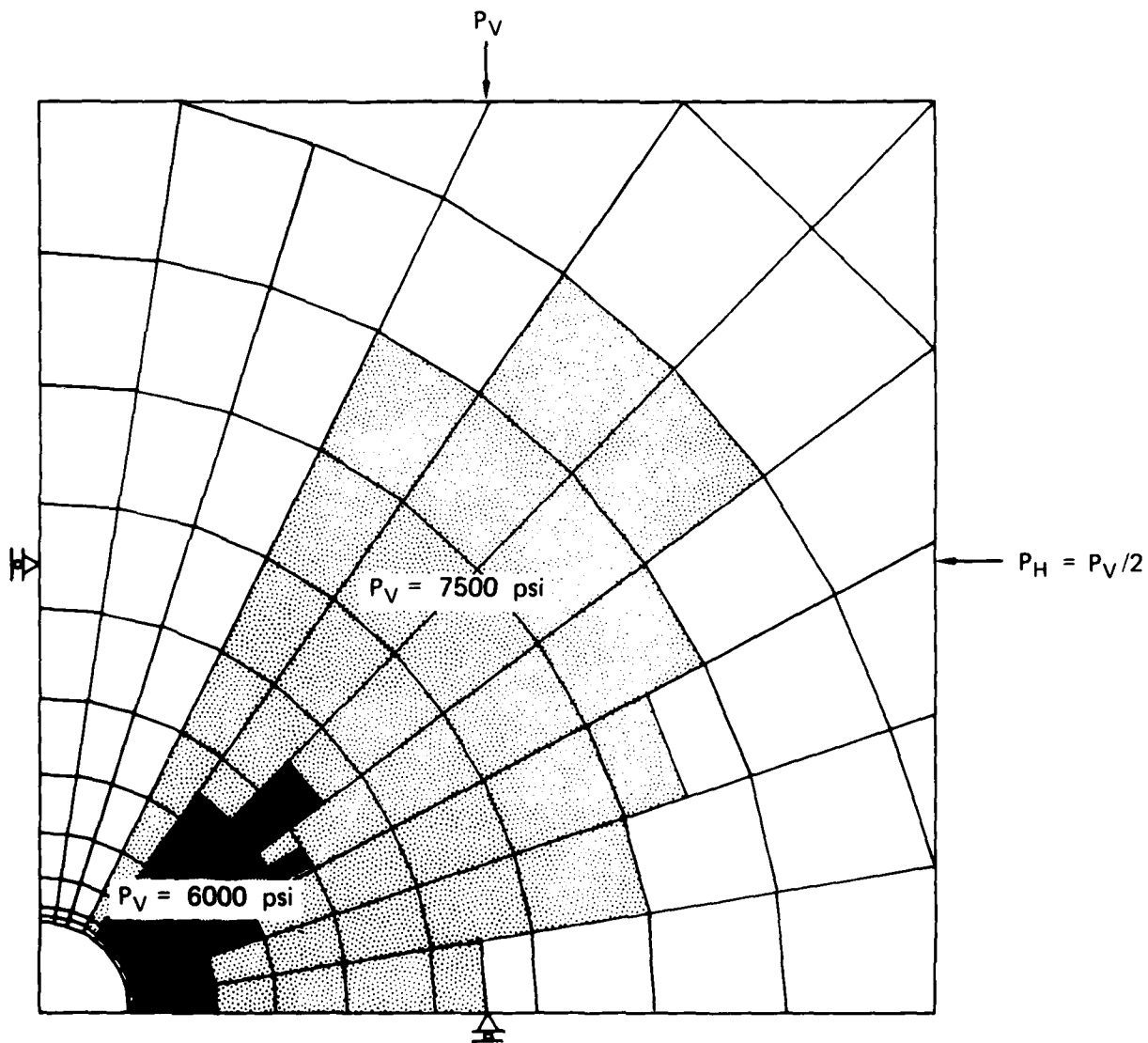
FIGURE 5.2   FINITE ELEMENT MESH FOR LINED CIRCULAR TUNNEL SHOWING PLASTIC ZONE
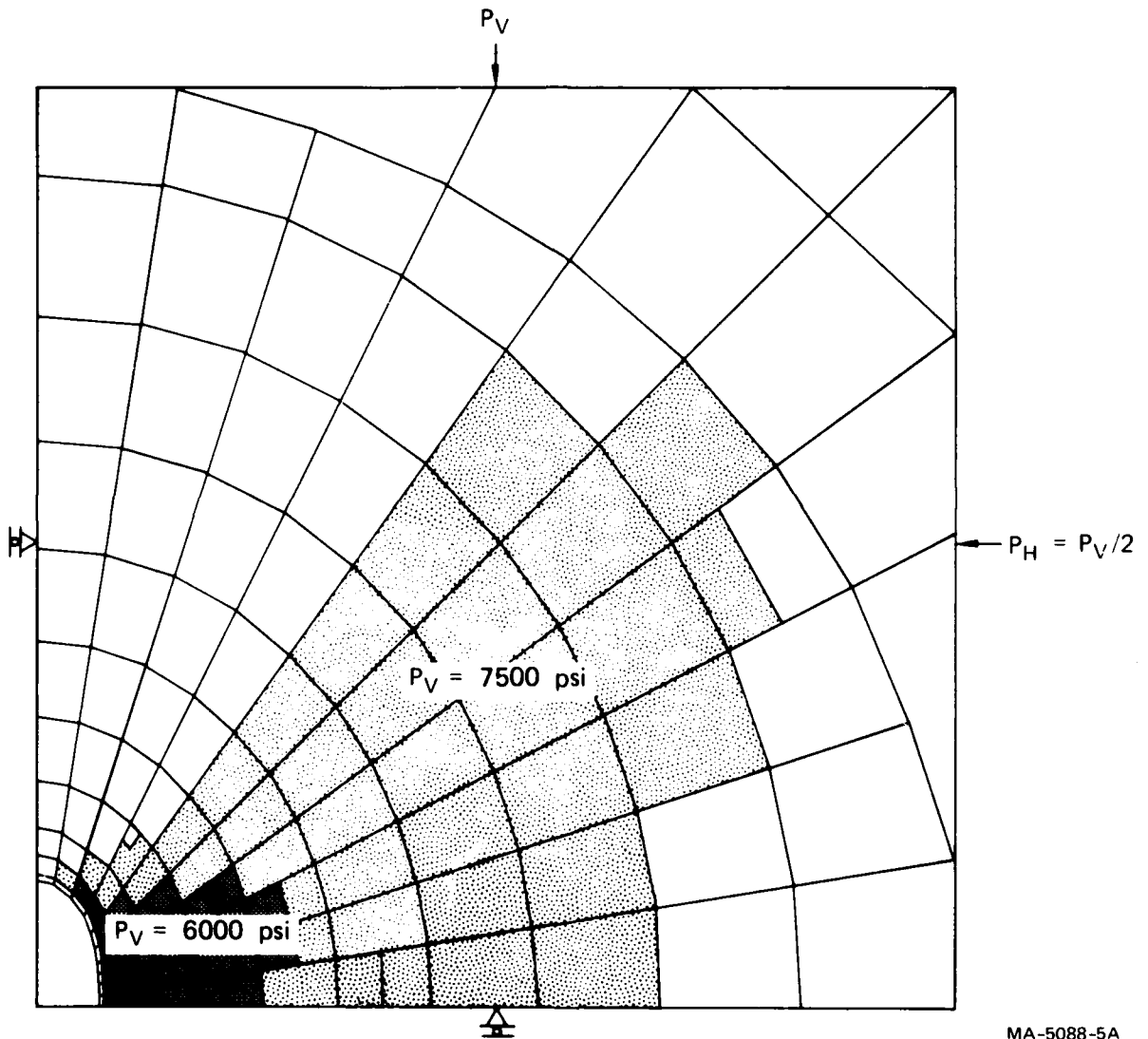
FIGURE 5.3   FINITE ELEMENT MESH FOR LINED ELLIPTICAL TUNNEL SHOWING PLASTIC ZONE

MA-5088-5A

119

At P_V = 6000 psi (41.4 MPa), the plastic zone extends slightly further from the tunnel for the circular cross section than for the elliptical cross section. However, at P_V = 7500 psi (51.7 MPa), the extent of the plastic zones is about the same for both structures and there is more yielding along the springlines for the elliptical structure.

Figure 5.4 plots vertical and lateral closures as functions of the vertical pressure for both structures. Closures are plotted as circles for circular tunnels and as squares for elliptical tunnels. Tunnel closure is nondimensionalized by dividing the change in lateral (spring-line) and vertical (crown-invert) diameters by 2R, the original diameter of the circular cavity.

Figure 5.4(a) shows closure data for unlined cavities with no internal pressure. Closure is about the same for both structures. At the greatest vertical pressure applied, 6000 psi (41.4 MPa), lateral closure exceeds vertical closure by a few percent for both structures, indicating that lack of strength at the springlines may lead to failure at higher loads.[*]

Figure 5.4(b) shows closure data for cavities with a uniform internal pressure P_i = 2000 psi (13.8 MPa). We used the larger mesh for these calculations and therefore could apply larger loads before the entire mesh yielded. Again, we find very little difference between closures for the two structures. The lateral closure is always smaller than the vertical closure, so we conclude that internal pressure of this magnitude is effective in preventing large springline closure.

Figure 5.4(c) shows closure data for lined cavities. Here we find the greatest differences between the two structures, especially in the lateral closures. Initially, the springlines of the circular structure move outward (negative lateral closure). Lateral closure is always inward for the ellipitcal structure. Vertical closure is about the same

---

[*]Large inward motion of the springlines has been identified as a failure mechanism at very large loads in experiments as well as calculations for other rock materials.
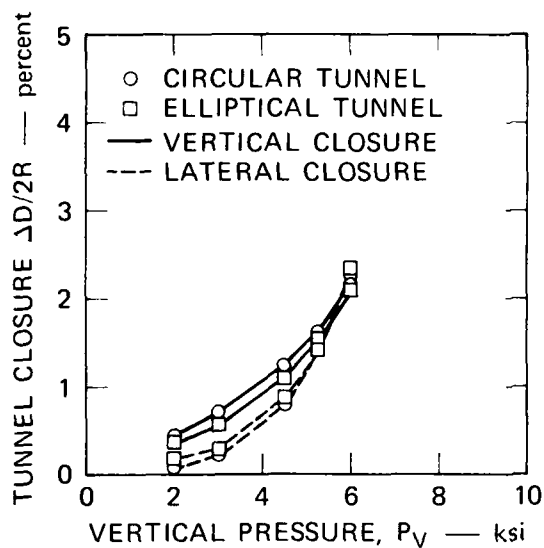
(a) UNLINED CAVITY, $P_i = 0$
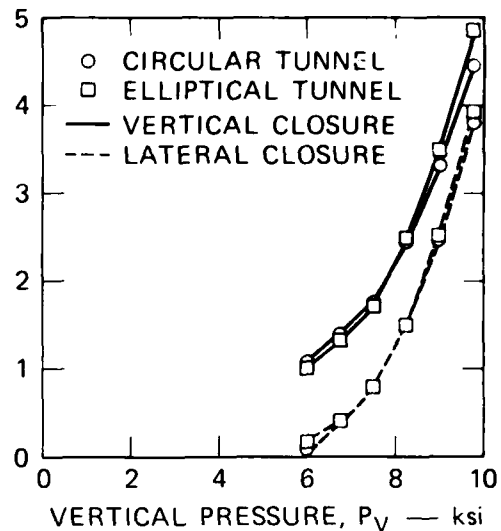
(b) CAVITY WITH UNIFORM INTERNAL PRESSURE $P_i = 2000$ psi
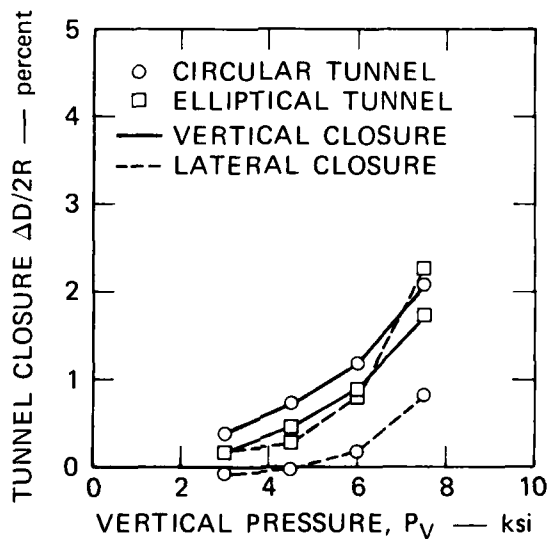
(c) LINED CAVITY, MILD STEEL LINER, R/h = 20

MA-5762-56

FIGURE 5.4   TUNNEL CLOSURE VERSUS VERTICAL PRESSURE FOR CIRCULAR AND ELLIPTICAL CAVITIES

121

for both structures. However, the lateral closure for the elliptical structure is about 2.8 times greater than that for the circular structure at the maximum load, $P_V = 7500$ psi (51.7 MPa). Hence, the elliptical structure is too weak at the springlines to prevent the increasing lateral closures observed for the unlined cavity. The difference in springline strength between the two structures is due to the difference in their curvatures at the springlines. The pressure exerted by the liner on the wall of the rock cavity is directly proportional to its curvature. The circular liner's greater curvature at the springlines results in greater pressure applied to the cavity wall and less closure.

A further comparison of the relative efficiencies of the two structures is given by the percentage decrease in cross-sectional area during deformation. For the circle, $\Delta A/A \approx (\Delta D_V + \Delta D_H)/2R$, and for the ellipse, $\Delta A/A \approx (\Delta D_V/\sqrt{2} + \sqrt{2}\Delta D_H)/2R$ where ΔD_V and ΔD_H are the changes in the vertical and lateral cavity diameters. Figure 5.5 plots reduction in cross-sectional area as a function of vertical pressure for both structure shapes. Again, data are plotted as circles for the circular cavity and as squares for the elliptical cavity. For the unlined cavity and the cavity with a uniform internal pressure, the elliptical structure shows a small advantage at low pressures and a small disadvantage at larger pressures. For lined cavities, however, neither structure has the advantage at low pressures, but the elliptical structure shows a large disadvantage at larger pressures. For example, at $P_V = 7500$ psi (51.7 MPa), the reduction in cross-sectional area for the ellipse is 55 percent greater than for the circle.

From these results we conclude that the advantage of elliptical structures in elastic material does not extend to elastic-plastic response. Elliptical structures are especially weak at the springlines and this is a serious drawback because springline collapse is known to be a failure mechanism. Furthermore, any small advantage in reduction of cross-sectional area at low pressures for the elliptical structures could be offset by increased fabrication costs.
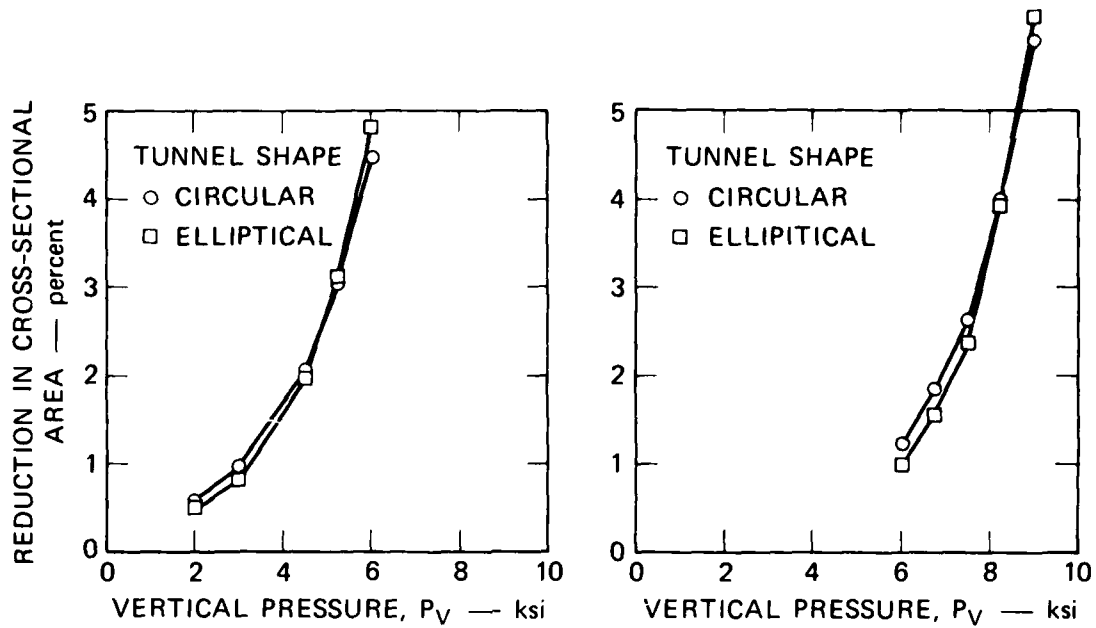
(a) UNLINED CAVITY, $P_i = 0$

(b) CAVITY WITH UNIFORM INTERNAL PRESSURE $P_i = 2000$ psi
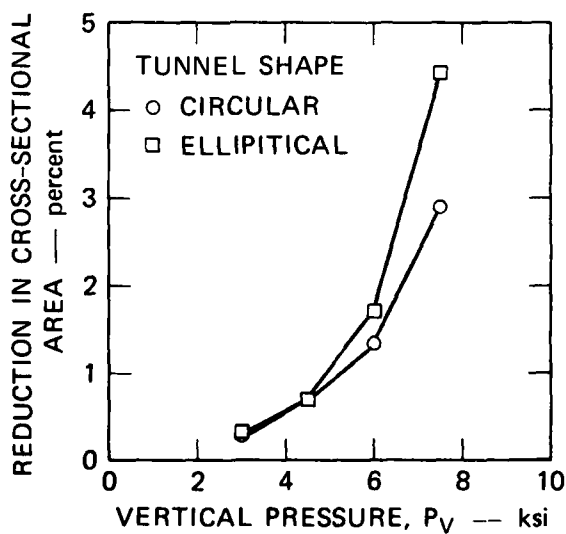
(c) LINED CAVITY, MILD STEEL LINER, R/h = 20

MA-5762-57

FIGURE 5.5   REDUCTION IN CROSS-SECTIONAL AREA VERSUS VERTICAL PRESSURE FOR CIRCULAR AND ELLIPTICAL CAVITIES

APPENDIX A

INSTRUMENTATION FOR ACTIVE TUNNEL CLOSURE AND
TUNNEL LINER STRAIN MEASUREMENTS

A.1 INTRODUCTION

In this appendix we describe instrumentation used to obtain active
tunnel closure and tunnel liner strain measurements in tests on our
12-inch-diameter (0.3-m) specimens. For the tests described in Chapter
4, we used two tunnel closure transducers and four liner strain gages.

A.2 TUNNEL CLOSURE TRANSDUCERS

The tunnel closure transducers were built from commercial LVDTs
(Linear Variable Differential Transformer) and mounting hardware. The
two transducers are located 7/16-inch (11 mm) on either side of the
tunnel midlength and are oriented to measure changes in the crown-invert
diameter and the springline diameter.

The LVDTs (Schaevitz Engineering, Model 100 MHR) have a linear
range of +0.10 inch (25 mm) and an extended range of +0.15 inch (3.9 mm)
with a modest reduction in linearity. For our 2-inch-diameter (50-mm)
tunnels the linear range corresponds to +5 percent closure. By posi-
tioning the core at one end of the linear range, we can measure closures
between 0 to 10 percent, but of one sign only. From experience we know
that vertical tunnel closure is always positive, so we can measure
closures between 0 to 10 percent. However, previous test results as
well as calculations indicate that springline closure changes sign
(gradually) in many tests. Therefore, we positioned the core in the
center of the linear range for the springline closure transducer. The
signal conditioning unit (Schaevitz Engineering, Model CAS-100) excites
the LVDT with 10 kHz and has a frequency response (-3db) of 1 kHz. This
is adequate for dynamic tests with the current pressure pulse risetimes
[4].

125

The assembled tunnel closure transducer is shown in Figure A.1. Figure A.2 shows an exploded iew of the transducer. The function of most parts is obvious. Two that require some discussion are the spindle mounts and the positioner rod. The spindle mounts attach the closure transducer to the tunnel liner wall. The mounts are inserted from the outside through small holes in the liner wall. The thin portion of the mount extends into the interior of liner and the tapered section wedges in the hole in the liner wall. Part of the tapered section extends beyond the outer diameter of the liner and is cut off flush with the liner. To prevent the mounts from moving outward before the liner is grouted into the tunnel or from being forced inward by porewater during the test, we epoxied a small square of 2-mil (.05-mm) shim steel over the liner mount hole. When the spindle mounts are in place, we position the transducer in the liner and lock it to the spindle mounts with set screws in the core support block and in the body support cap.

The positioner rod threads into the core support block and is locked in place with the lock nut. We adjust the initial position of the core in the LVDT body by threading the positioner rod in or out of the core support block. Positioning the core with the positioner rod is performed before the transducer is mounted in the tunnel, and therefore is only approximate. Initial core position can be fine-tuned by locking the set screws at the desired position on the spindle mounts.

A.3 TUNNEL LINER STRAIN GAGES

Tunnel liner strain gages were commercial, high elongation strain gages and were mounted on the outside of the liner at its midlength. The four gages were oriented to measure circumferential strain and were stationed at the crown, the invert, and at both springlines.

The gages (Micro-Measurements EP-08-062AA-120) have a gage length of 62 mils (1.6 mm) and are of the annealed constantan foil type, capable of measuring strains up to 10 percent. They are mounted with high elongation epoxy (M-Bond AE-15) and sealed with a protective coating (M-Coat G), both products of Micro-Measurements, Inc.

126
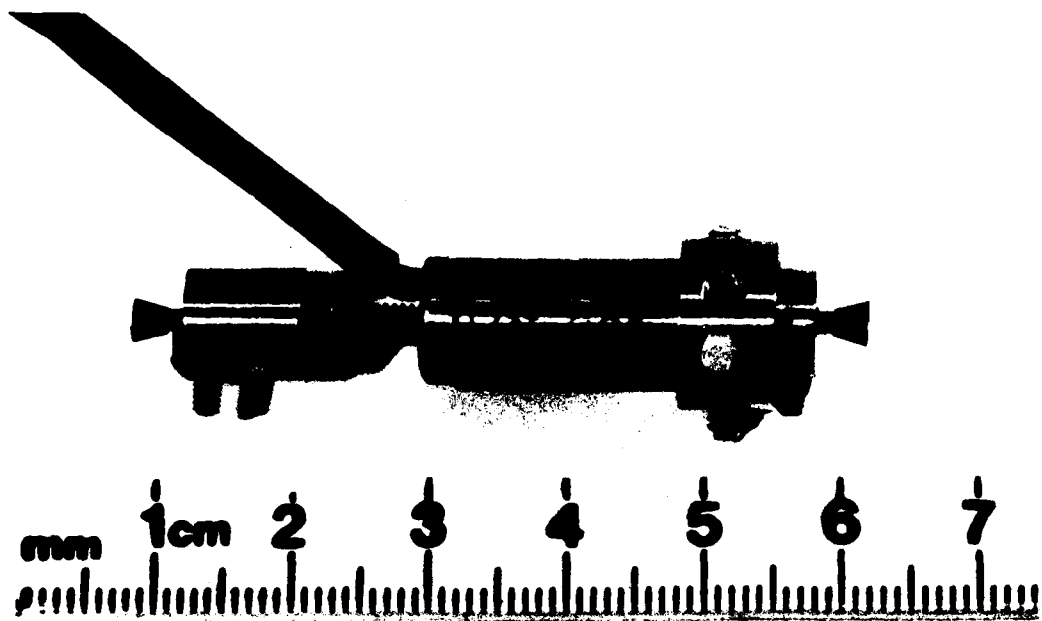
MP-5762-36

FIGURE A.1   ASSEMBLED TUNNEL CLOSURE TRANSDUCER
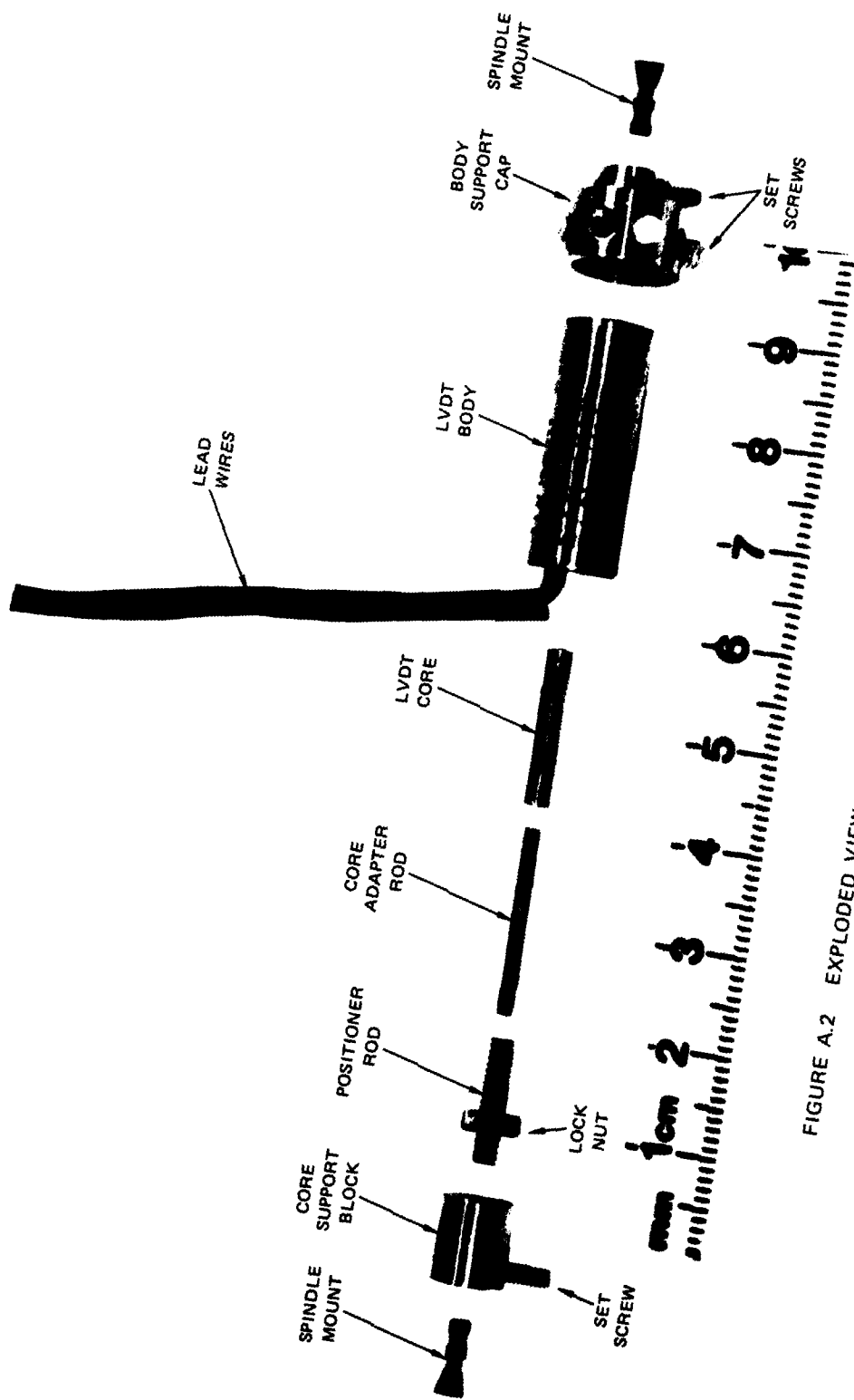
FIGURE A.2 EXPLODED VIEW OF TUNNEL CLOSURE TRANSDUCER

MP-5762-37

128

The signal conditioning unit (Honeywell Accudata 218 bridge amplifier) contains three precision resistors to complete the bridge. Gage excitation is 10 volts with remote sensing (measured at the gage). The unfiltered amplifier frequency response (-3 db) is 50 kHz, more than adequate for dynamic testing. Gage leads were strung inside the tunnel liner to the tunnel midlength. There, they exit to the liner exterior through small holes midway between the gage stations.

Since the gages are mounted on the outside of the liner, they will be under pressure during the test. The pressure acting on the gages is the resisting pressure exerted by the liner, typically a few ksi (a few tens of MPa). Pressures of this magnitude do not affect gage properties or output [12-15].

Blank

REFERENCES

1. T. C. Kennedy, J. V. Zaccor, and H. E. Lindberg, "Laboratory
    Investigation of Response of Deep-Based Structures," DNA3610F,
    SRI International Final Report, Project 3044, Menlo Park,
    California (October 1975).

2. T. C. Kennedy and H. E. Lindberg, "Laboratory Investigation of
    Rock Cavity Reinforcement," DNA 4023F, SRI International Final
    Report, Project 3743, Menlo Park, California (April 1976).

3. P. E. Senseny and H. E. Lindberg, "Theoretical and Laboratory
    Study of Deep-Based Structures, Volume II: Model Tests and
    Analysis of Mighty Epic Structures," DNA4425F, SRI International
    Final Report, Project 4121, Menlo Park, California (December 1977).

4. P. E. Senseny and H. E. Lindberg, "Theoretical and Laboratory
    Study of Deep-Based Structures, Volume I: Triaxial Machine for
    Static and Dynamic Testing of 12-inch-Diameter Rocks," DNA4425F,
    SRI International Final Report, Project 4121, Menlo Park, California
    (July 1977).

5. T. Hatano and H. Tsutsami, "Dynamical Compressive Deformation and
    Failure of Concrete Under Earthquake Load," Technical Report C-5904,
    Central Research Institute of Electric Power Industry, Tokyo, Japan,
    (1959).

6. D. W. Taylor and R. V. Whitman, "The Behavior of Soils Under
    Dynamic Loadings - 3, Final Report on Laboratory Studies," MIT
    Dept. of Civil and Sanitary Engineering Soils Lab, Cambridge,
    Mass (August 1954).

7. H. B. Seed and R. Lundgren, "Investigation of the Effect of
    Transient Loading on the Strength and Deformation Characteristics
    of Saturated Sands," Proc. ASTM, Vol. 54, pp. 1288-1306 (1954).

8. A. Casagrande and W. L. Shannon, "Stress, Deformation and Strength
    Characteristics of Soils under Dynamic Loads," Proc. 2nd ICSMFE,
    Vol. V. pp. 29-34 (1948).

9. J. N. Johnson and S. J. Green, "The Mechanical Response of Porous
    Media Subject to Static Loads," The Effects of Voids on Material
    Deformation, AMD - Vol. 16, ed. S. C. Cowin and M. M. Carroll
    (June 1976).

10. S. Timoshenko and J. N. Goodier, _Theory of Elasticity_, McGraw-Hill Book Co., Inc., New York (1951).

11. I. S. Sokolnikoff, _Mathematical Theory of Elasticity_, McGraw-Hill Book Co., Inc., New York (1956).

12. W. G. Brace, "Effect of Pressure on Electric-Resistance Strain Gages," _Experimental Mechanics_, Vol. 4, pp. 212-216 (1964)

13. G. A. Kular, "Use of Foil Strain Gage at High Hydrostatic Pressure," _Experimental Mechanics_, Vol. 12, pp. 311-316 (1972).

14. R. N. Schock and A. G. Duba, "Pressure Effects on the Response of Foil Strain Gages," _Experimental Mechanics_, Vol. 13, pp. 43-44 (1973).

15. C. G. Foster, "Response of Foil Strain Gages to Hydraulic Pressure," _Experimental Mechanics_, Vol. 17, pp. 26-32 (1977).

DISTRIBUTION LIST

DEPARTMENT OF DEFENSE

Assistant to the Secretary of Defense
Atomic Energy
    ATTN: Executive Assistant

Defense Advanced Rsch. Proj. Agency
    ATTN: TIO

Defense Intelligence Agency
    ATTN: DB-4C2
    ATTN: RDS-3A

Defense Nuclear Agency
    ATTN: STVL
    ATTN: RAEV
3 cy ATTN: SPSS, T. Deevy
4 cy ATTN: TITL

Defense Technical Information Center
12 cy ATTN: DD

Defense Nuclear Agency
    ATTN: FCTMOF
    ATTN: FCPR

Defense Nuclear Agency
Livermore Division
    ATTN: FCPRL

Field Command Test Directorate
Defense Nuclear Agency
2 cy ATTN: FCTC, J. Lacomb

Joint Strat. Tgt. Planning Staff
    ATTN: JLA
    ATTN: NRI-STINFO Library

Undersecretary of Def. for Rsch. & Engr.
    ATTN: Strategic & Space Systems (OS)

DEPARTMENT OF THE ARMY

Chief of Engineers
Department of the Army
    ATTN: DAEN-MCE-D
    ATTN: DAEN-RDM

Construction Engineering Rsch. Laboratory
Department of the Army
    ATTN: CERL-SOI-L

Harry Diamond Laboratories
Department of the Army
    ATTN: DELHD-N-P

U.S. Army Ballistic Research Labs
    ATTN: DRDAR-TSB-S
    ATTN: DRDAR-BLT, W. Taylor
    ATTN: DRDAR-BLE, J. Keefer
    ATTN: DRDAR-BLV

U.S. Army Communications Command
    ATTN: Technical Ref. Division

U. S. Army Concept Analysis Agency
    ATTN: CSSA-ADL

DEPARTMENT OF THE ARMY (Continued)

U.S. Army Engineer Center
    ATTN: DT-LRC

U.S. Army Engineer Dist. Omaha
    ATTN: MROED-D, D. Distefano

U.S. Army Engineer Div. Huntsville
    ATTN: HNDED-SR
3 cy ATTN: C. Huang

U.S. Army Engineer Div. Ohio River
    ATTN: ORDAS-L

U.S. Army Engr. Waterways Exper. Station
    ATTN: P. Mlakar
    ATTN: Library
    ATTN: WESSD, G. Jackson
    ATTN: WESSE, L. Ingram
    ATTN: J. Drake
    ATTN: WESSA, W. Flathau
    ATTN: WESSS, J. Ballard
    ATTN: J. Day

U.S. Army Nuclear & Chemical Agency
    ATTN: Library

DEPARTMENT OF THE NAVY

Dir. Cmd. Con. Plan. & Prgmng. Div.
Department of the Navy
    ATTN: OP-943

Naval Construction Battalion Center
    ATTN: Code L51, W. Shaw
    ATTN: Code L44, H. Haynes
    ATTN: Code L08A
    ATTN: Code L51, R. Odello
    ATTN: Code L51, S. Takahashi

Naval Electronic Systems Command
    ATTN: PME 117-211, B. Kruger

Naval Facilities Engineering Command
    ATTN: Code 09M22C

Naval Postgraduate School
    ATTN: Code 0142, Library

Naval Research Laboratory
    ATTN: Code 2627

Naval Surface Weapons Center
    ATTN: Tech. Library & Info. Svc. Br.

Naval War College
    ATTN: Code E-11

Strategic Systems Project Office
Department of the Navy
    ATTN: NSP-43

DEPARTMENT OF THE AIR FORCE

Air Force Institute of Technology
    ATTN: Library

Air Force Weapons Laboratory
Air Force Systems Command
    ATTN: NT, D. Payton
    ATTN: NTE, M. Plamondon
    ATTN: SUL

Assistant Chief of Staff
Studies & Analyses
Department of the Air Force
    ATTN: AF/SASM

Ballistic Missile Office/MN
Air Force Systems Command
    ATTN: MNN
    ATTN: MNNH

Deputy Chief of Staff
Operations Plans and Readiness
Department of the Air Force
    ATTN: AFXODC

Deputy Chief of Staff
Research, Development & Acq.
Department of the Air Force
    ATTN: AFRDQSM

Foreign Technology Division
Air Force Systems Command
    ATTN: NIIS Library

Strategic Air Command
Department of the Air Force
    ATTN: XPFS
    ATTN: NRI-STINFO Library

DEPARTMENT OF ENERGY CONTRACTORS

Lawrence Livermore National Laboratory
    ATTN: H. Heard
    ATTN: L-96, L. Woodruff
    ATTN: Technical Information Dept. Library
    ATTN: L-21, D. Oakley

Los Alamos National Scientific Laboratory
    ATTN: L. Germaine
    ATTN: MS 364
    ATTN: B. Killian
    ATTN: J. Johnson

Oak Ridge National Laboratory
Nuclear Div., X-10 Lab. Records Division
    ATTN: Central Research Library

Sandia National Laboratories
Livermore Laboratory
    ATTN: Library & Security Class. Div.

Sandia National Laboratories
    ATTN: L. Hill
    ATTN: 3141

OTHER GOVERNMENT AGENCIES

Department of the Interior
Bureau of Mines
    ATTN: Technical Library

Department of the Interior
U.S. Geological Survey
Special Projects Center
    ATTN: W. Twenhofel
    ATTN: R. Carroll
    ATTN: D. Snyder

Department of the Interior
U.S. Geological Survey
    ATTN: D. Roddy

DEPARTMENT OF DEFENSE CONTRACTORS

Aerospace Corp.
    ATTN: Technical Info. Services
    ATTN: P. Mathur

Agbabian Associates
    ATTN: C. Bagge
    ATTN: M. Balachanda
2 cy ATTN: M. Agbabian

Applied Theory, Inc.
2 cy ATTN: J. Trulio

AVCO Research & Systems Group
    ATTN: Library A830

BDM Corp.
    ATTN: Corporate Library
    ATTN: T. Neighbors

Boeing Company
    ATTN: T. Berg
    ATTN: M/S 42/37, K. Friddell
    ATTN: J. Wooster
    ATTN: R. Dyrdahl
    ATTN: H. Leistner
    ATTN: Aerospace Library

California Instute of Technology
    ATTN: D. Anderson

California Research & Technology, Inc.
    ATTN: Library
    ATTN: S. Schuster
    ATTN: K. Kreyenhagen

California Research & Technology, Inc.
    ATTN: D. Orphal

University of California
    ATTN: N. Cook
    ATTN: R. Goodman

Calspan Corp.
    ATTN: Library

Civil Systems Inc.
    ATTN: J. Bratton

134

DEPARTMENT OF DEFENSE CONTRACTORS (Continued)

University of Denver
Denver Research Institute
    ATTN: Sec. Officer for J. Wisotski

EG&G Wash. Analytical Srv. Center, Inc.
    ATTN: Library

Electromechanical Sys. of New Mexico, Inc.
    ATTN: R. Shunk

Eric H. Wang
Civil Engineering Rsch. Fac.
University of New Mexico
    ATTN: N. Baum

Foster-Miller Associates, Inc.
    ATTN: J. Hampson for E. Foster

Franklin Institute
    ATTN: Z. Zudans

General Electric Company—TEMPO
    ATTN: DASIAC

IIT Research Institute
    ATTN: R. Welch
    ATTN: M. Johnson
    ATTN: Documents Library

Institute for Defense Analyses
    ATTN: Classified Library

J. H. Wiggins Co., Inc.
    ATTN: J. Collins

Kaman AviDyne
    ATTN: Library

Kaman Sciences Corp.
    ATTN: Library

Lockheed Missiles & Space Co., Inc.
    ATTN: Technical Information Center
    ATTN: T. Geers

Massachusetts Inst. of Technology
    ATTN: W. Brace

Merritt CASES, Inc.
    ATTN: J. Merritt

Nathan M. Newmark Consult. Eng. Svcs.
    ATTN: A. Hendron
    ATTN: W. Hall
    ATTN: N. Newmark

City College of New York
Dept. of Civil Engineering
    ATTN: C. Miller

Northwestern University
Technology Institute
    ATTN: T. Belytschko

Pacifica Technology
    ATTN: G. Kent

DEPARTMENT OF DEFENSE CONTRACTORS (Continued)

Physics International Co.
    ATTN: Technical Library
    ATTN: F. Sauer
    ATTN: E. Moore

R & D Associates
    ATTN: J. Lewis
    ATTN: C. MacDonald
    ATTN: R. Port
    ATTN: Technical Information Center
    ATTN: D. Shrinivasa
    ATTN: D. Rawson
    ATTN: P. Haas

Rand Corp.
    ATTN: A. Laupa

Science Applications, Inc.
    ATTN: Technical Library

Science Applications, Inc.
    ATTN: Technical Library

Southwest Research Institute
    ATTN: A. Wenzel
    ATTN: W. Baker

SRI International
    ATTN: B. Holmes
    ATTN: G. Abrahamson
    ATTN: H. Lindberg

Systems, Science & Software, Inc.
    ATTN: C. Archembeam
    ATTN: W. Wray
    ATTN: T. Bache
    ATTN: R. Duff
    ATTN: D. Grine
    ATTN: Library

Terra Tek, Inc.
    ATTN: Library
    ATTN: H. Pratt

Tetra Tech., Inc.
    ATTN: Library

Texas A & M University System
    ATTN: Sec. Officer for A. Rychlik
    ATTN: J. Handin

TRW Defense & Space Sys. Group
    ATTN: Technical Information Center
    ATTN: N. Lipner
    ATTN: P. Huff

TRW Defense & Space Sys. Group
    ATTN: E. Wong
    ATTN: P. Dai

Universal Analytics, Inc.
    ATTN: E. Field

DEPARTMENT OF DEFENSE CONTRACTORS (Continued)

Weidlinger Assoc., Consulting Engineers
    ATTN: M. Baron
    ATTN: I. Sandler

Weidlinger Assoc., Consulting Engineers
    ATTN: J. Isenberg

DEPARTMENT OF DEFENSE CONTRACTORS (Continued)

Westinghouse Electric Corp.
    ATTN: W. Volz

William Perret
    ATTN: W. Perret